Delft University of Technology

MSc. Thesis

Precision Improvement in Optical Alignment Systems of Linear Colliders

Pre-aligning the Compact Linear Collider using Rasniks

Supervisors:
Dr. Ir. H. van der Graaf
Prof. Dr. Ir. T.M. Klapwijk

Author:
Joris van Heijningen

February 29, 2012

Delft University of Technology

MSc. Thesis

Precision Improvement in Optical Alignment Systems of Linear Colliders

Pre-aligning the Compact Linear Collider using Rasniks

Supervisors:
Dr. Ir. H. van der Graaf
Prof. Dr. Ir. T.M. Klapwijk

Author:
Joris van Heijningen

The research described in this thesis was performed in the Detector Research and Development group of the Dutch National Institute for Subatomic Physics (Nikhef), Science Park 105, 1098 XJ Amsterdam, The Netherlands, and in the Quantum Nanoscience department of the Delft University of Technology, Lorentzweg 1, 2628 CJ Delft, The Netherlands, in collaboration with the Accelerator & Beam Physics Survey and Alignment group (ABP-SU) of the Beams Department (BE) at the European Organisation for Nuclear Research (CERN), CH-1211 Genève 23, Switzerland

Abstract

This thesis reports on progress in various Nikhef solutions for the alignment of the proposed Compact Linear Collider. Optical three-point-alignment systems are proposed for the small (60 mm), intermediate (2 m) and large (200 m) alignment distances. A projective alignment system, called Rasnik and consisting of a back-illuminated chess field mask, a lens and an image sensor, is used for the small and intermediate distances. An alignment system that uses diffraction for image generation, called Rasdif and consisting of a diode laser, a diffraction plate and an image sensor, is used on the intermediate and large distances. A 4 m set-up at Nikhef and a 140 m set-up at CERN were used for validation of the performance of the optical alignment systems for the different alignment distances. A 0.5-1 μm resolution is reported for thermally shielded 4 m Rasniks and Rasdifs in open air and a 1.5-2 μm resolution is reported for a 140 m Rasdif in a 1.5×10^{-4} mbar vacuum.

A Rasdif anomaly was discovered during preliminary measurements on the 4 m set-up: the virtual departure of the spherical waves of light, the point where the waves *seem* to be coming from, did not coincide with the physical location of the laser. The translation of the image is governed by the translation of this virtual point, whereas governance by the physical point is desired. A Diode Pumped Solid State (DPSS) laser came out as best of measurements that searched for laser with a near virtual point. Translational linearity tests on the 4 m set-up pin the virtual point of departure about 4 cm behind the these lasers. Translational measurements of the 140 m Rasdif show great discrepancies in two separate measurements and this is subject to future investigation. Cramér-Rao Lower Bound (CRLB) analysis on simulated Rasdif images show the current diffraction plates, with an outer radius of 1.44 mm, have to be scaled to a design with an outer radius of 2.55 mm to obtain images with more gradient energy.

For the alignment of the final focusing magnets of the collider, position information about the location of these magnets is radially transferred to non-near-vertex locations by Zerodur spokes. The ends of these spokes are then aligned by Rasniks and/ or Rasdifs. Preliminary results of a 1 m Zerodur spoke set-up confirm the zero coefficient of expansion and Young's modulus of the material. Contact repeatability for one end of Zerodur, with a steel semi-sphere glued to it, and a reference block is measured to be within 150-200 nm by a 60 mm Rasnik attached to the other side of the spoke.

Acknowledgements

More than a year has passed since I started working on this project in the Detector Research and Development Group at Nikhef. First and foremost I would like to thank my direct supervisor Harry van der Graaf for the endless streams of discussion and good ideas. His undying enthusiasm for the project has been contagious to me. His sharp questions and remarks regarding this report made it a more clear and complete thesis.

The RasCLiC meetings every Tuesday have been very instructive and I would like to thank all its participants over the course of my time at Nikhef: Niels van Bakel, Harry van der Graaf, Henk Groenstege, Bram Bouwens, Gerrit Brouwer, Richard Rosing, Aran Alaei, Gerjan Bobbink, Jan Koopstra and Robert Hart.

I would like to thank Gerrit Brouwer from Nikhef's mechanical workshop for his brilliant skills in construction and modification of (parts of) set-ups used for this project. Richard Rosing and Aran Alaei from the Mechnical Engineering Department have contributed to the progress of this project by their excellent technical drawings. Henk Groenstege and Jan Koopstra from the Electronic Engineering Department have been of great aid to me in the field of their expertise. For all my software trouble and questions, Bram Bouwens has been of great help and I owe him my gratitude as well.

For those who helped me during my various measurement trips to CERN a word of gratitude is also due: Gerjan Bobbink, Vivien Rude, Helene Mainaud Durand, Nick Gazis and Michail Anastasopoulos.

I have learned a lot during my time at the Detector R& D department at Nikhef, but there was also time for *fun and games*. Various diners, outings, board game afternoons and gigs were extremely entertaining. Thank you Niels, Harry, Jan, Martin, Jan, Fred, Jan, Matteo, Gijs, Marten, Martin, Rolf, Wilco, Francesco, Enrico, Erisch, Panagiotis, Brent and Hong Wah.

Finally I would like to thank Teun Klapwijk for the various meetings at the Technical University of Delft on the progress of my project. His sharp questions and insights have helped me when I was in need of some direction and advice.

Contents

Chapter 1

Introduction

The builders of the ancient Temples of the Sun and Stonehenge-like structures were the first humans that practised the fine art of alignment. They placed large stones or pieces of rock that had the preferred shape in such a way that the rays of light coming from the sun would draw the preferred shadow or shine at some important point. The ancient Egyptians would know the start of a new period when the sun would rise along the left side of the Cheops pyramid, viewed from a nearby temple. This, for example, would show them at specific points of every year when to sow their seeds and when to harvest. The alignment was done on the decimetre scale and if the 'contractor' said it was aligned, the construction was aligned.

Throughout history, alignment has made a tremendous progress. One can think of lengthy bridges or tunnels where — without alignment — the construction would have been little more than a trial and error process. Structures of our current time that need the most precise alignment are those that make tiny particles collide. Beams of these particles consist of so-called bunches, which are clusters of particles, that have sub-nanometre dimensions. Making these bunches collide at designed collision points means *very* precise alignment of these beams is thus of the utmost importance.

1.1 Context and motivation

The focus of this thesis is on linear accelerator alignment. Even though linear accelerators already exist and have been sufficiently aligned to the criteria needed in the past, research in this field has not come to a standstill. Better alignment enhances the performance of the linear accelerator and new proposed linear accelerators have the need for better alignment in order to achieve their design goals.

Despite the fact that the Large Hadron Collider (LHC) is coming up to its design centre of mass energy of 14 TeV in a couple of years, plans for new accelerators are in an advanced state of preparation. The two leading ideas for a new linear accelerator technology are the International

Linear Collider (ILC) and the Compact Linear Collider (CLiC). Both are designed to hurl positrons and electrons up to tremendous speeds and to make them collide. This thesis focuses on the alignment of the CLiC particle accelerator.

In the sub micron world, where steel behaves as jelly and a minute change in temperature gives rise to expansions in the same order as the alignment criteria, fixing the structure of the accelerator completely is impossible. One must know the location of all structural elements with respect to each other and realign these continuously to guarantee alignment. This requires alignment systems with multiple read-outs per second in order to meet the preferred demands. Their data output can serve as input for actuators which realign the components.

1.2 Outline

Chapter 2 is about the history and operation of linear colliders and their alignment. Also, a description of the technical designs for the ILC and the CLiC is given here. The preferred alignments systems of this study are presented in Chapter 3 and whether they could align the proposed CLiC is covered in Chapter 3. In Chapter 4, the two experimental set-ups used to obtain this thesis' results are presented: one 4 m set-up at Nikhef and a 140 m set-up at CERN.

All alignment systems are subject to some types of error and these are analysed for the preferred systems. Together with methods of precision improvement this is the subject of Chapter 5. The results from the set-ups and further improvements regarding the thermal sources of error are explained in Chapter 6. These findings are the basis of the design for future implementations at linear collider test facilities at CERN. These implementations are shown in Chapter 7. In Chapter 8 the conclusions of this thesis and recommendations for future work are found.

Listed in the Bibliography are all sources of material, data and computer programs used. Appendices are added on the Matlab scripts used for data analysis and simulation as well as a stand-alone manual for the current set-up in the TT1 transfer tunnel at CERN.

Chapter 2

Linear Colliders

The first linear accelerator, accelerating positive ions to about 50 keV, was patented and built in 1928 by R. Widerøe. G. Ising had proposed this linear accelerator concept four years earlier, but the initial idea came from an Austro-Hongarian nuclear physicist, named Leó Szilárd [1]. A few decades later, the world saw the first medical implementation of a linear accelerator. In 1956, six months after a first model was used in England, Herny Kaplan came to Stanford with an unusual goal: using the local linear accelerator to fight cancer. A 2-year-old boy's eye tumour was treated with success and 50 years later 40 million patients have been treated in a similar way, making linear accelerators the backbone of radiation therapy worldwide [2], [3].

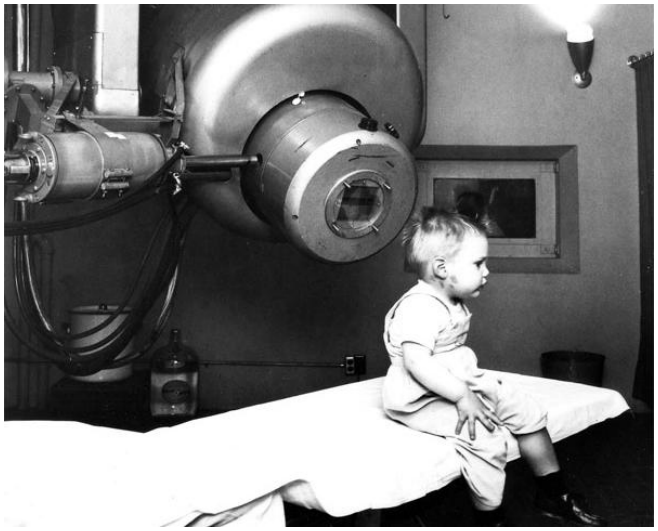

Figure 2.1: The first patient who was treated by a linear accelerator

The scope of this thesis lies in the implementation of linear accelerators in high energy physics. A clear distinction is made between linear accelerators and linear colliders. Linear accelerators are found in fixed

target experiments, where particles are fired upon a target, or as an accelerator section of a bigger circular collider. The term linear collider is used when two linear accelerators are positioned in such a way that the particle beams of both linacs meet at a designed collision point. An array of detectors if positioned around this collision point, detecting the products of the collisions.

When discussing linear colliders, a dive is first made into the history of the linear accelerator. When, where and how the first linear accelerators were constructed and which of them are still in operation is discussed. The most important alignment systems used in their construction and continuous alignment are then described and this chapter is concluded with an explanation and comparison of the two main linear collider projects of the future. In today's tight economical environment it is unlikely that *both* of these colliders will be built, which means that in the near future a *choice* will have to be made which one is most viable.

2.1 Operation of linear accelerators

Discussing the operation of any present collider is not possible without discussing the klystron first. The word klystron is an amalgamation from the stem from of a Greek verb $\kappa\lambda\upsilon\sigma$ (klys) and the word electron. This Greek verb describes the fraction of waves upon the shore. The klystron was invented by Russell and Sigurd Varian at Stanford University. In 1939 they published about a high frequency amplifier [5]. In Figure 2.2(a) a schematic picture of a typical klystron is displayed. Whilst klystrons are used in other fields, e.g. as a reference oscillator for heterodyne receivers in observational astrophysics, only the type of klystrons used for (linear) colliders is discussed here.

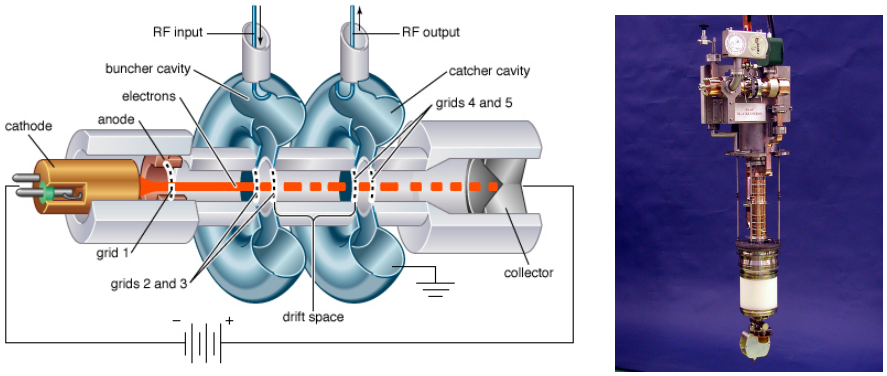

(a) (b)

Figure 2.2: (a) Schematic overview of a klystron and (b) a photograph of a SLAC XL4 klystron

Klystrons amplify radio frequency (RF) signals by converting the ki-

netic energy (per unit of time) of a DC electron beam into RF power. Electrons are produced at a thermionic cathode and accelerated through a hole in an anode. They are fed to the *buncher* cavity where an input RF signal is coupled in. This coupling occurs through an oscillating electric field at, or close to, the natural frequency of the cavity, which has effect on the beam of electrons. Electrons are accelerated or decelerated depending of their phase, in such a way that bunching occurs. As the electrons now have different speeds travelling through a drift tube, maximum bunching occurs at some location behind the buncher cavity and that's where the conversion of the kinetic energy of the electron beam occurs. The RF bunched electrons produce an RF magnetic field with maximum amplitude at the *catcher* cavity and this will excite a voltage across the gap of this cavity. The developed RF energy is coupled out and can be used for acceleration of bunches in accelerators or as input for even higher power klystrons. It is possible to have multiple buncher cavities and catcher cavities further increasing the bunching and total conversion efficiency respectively. However, this sets stricter precision requirements to the difference between input frequency and natural frequency of the cavities. Klystron amplifiers have the advantage over other types of amplifiers, because these coherently amplify a reference signal in such a way that its output may be precisely controlled in amplitude, frequency and phase.

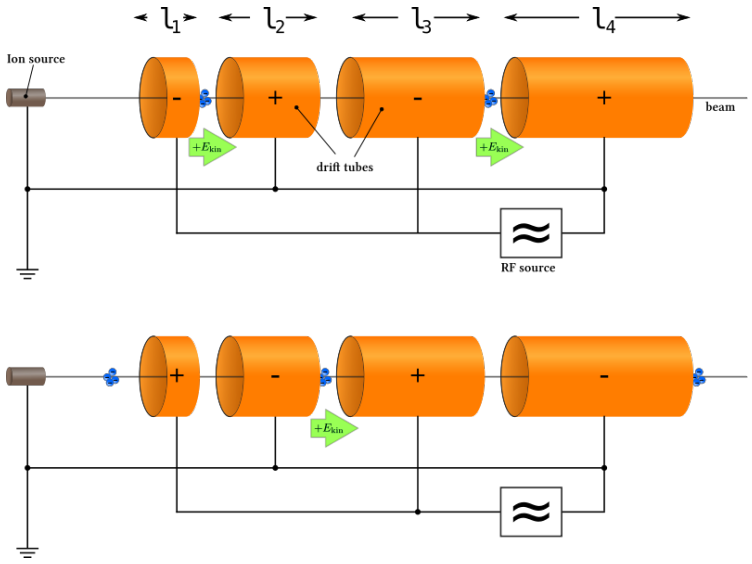

Figure 2.3: Schematic operation of a linear accelerator

The amplified RF signal can now be fed to a linear accelerator as is shown schematically in Figure 2.3. An ion (or any other charged particle) is *produced* at a source an given an initial speed, e.g. by a thermionic cathode-anode, similar to the production of the electron beam in the klystron. The ion *sees* the electric field generated by the voltage on the

first accelerator section with dimension l_1. When the input signal of the accelerator section would be DC, then the ion would, upon exiting the section, be attracted again. The RF oscillating voltage makes sure the voltage flips every time the to be accelerated particle is in the middle of a section, so that is repelled, i.e. accelerated to the next section. Because the velocity of the particle is increasing, but the RF signal has constant frequency the section dimensions (l_2, l_3 and l_4) increase. This and the fact that, for high voltages, non-superconducting materials dissipate a lot of heat make the choice for running pulsed bunches of particles through an accelerator a logical one.

For circular accelerators the precise increasing of the RF signal is necessary when particles are in a part of the accelerator where they have been accelerated before. This is one of the disadvantages of circular over linear colliders. A big advantage as that particles in beams that didn't collide are reusable as they travel along the circle again. Circular accelerators have often been chosen for particle collider experiments in the past, but now that particle physics needs very-high-energy lepton (low mass elementary particles) colliders the other disadvantages of circular acceleration need to be considered. Energy loss through synchrotron radiation is inversely proportional to the fourth power of the mass of the particles in question. That's why circular high energy colliders are built for heavy particles such as the LHC for protons. An electron-positron collider of the same size would never be able to achieve the same collision energies. In fact, energies at the Large Electron-Positron Collider (LEP), which used to occupy the tunnel now given over to the LHC, were limited to 209GeV by energy loss via synchrotron radiation. Building a 1 TeV centre-of-mass electron-positron circular accelerator would mean a 675 km circumference and, because of synchrotron radiation losses, an RF power input of 100 GW for a luminosity (a measure for the amount of collisions per unit of time) of $10^{34}\ cm^{-2}s^{-1}$ or $10^{-5}\ fb^{-1}s^{-1}$. This is about twice the power usage of the entire state of California in the summer. The size of the collider as well as its power usage seem excessive [6].

The explanation of the klystron and the linear accelerator given above is very basic, but is ample to appreciate the need for strict alignment requirements. If the positions of the different accelerator sections recede and are unknown, a lot of beam intensity can be lost and wake fields, generated by beams incident the linac structure itself, can arise. On the one hand, the klystrons generating the RF signal are attuned to the position of the accelerator section. On the other hand, particles not going exactly through the middle of such a section are deflected even more away from the intended path. Infinite precision on this is not possible and is countered, e.g. by focussing magnets, but the amount of misalignment that can be corrected for has its boundaries. These boundaries and the beam size one would like to acquire, int. al., invoke the alignment criteria.

2.2 Present linear accelerators

Throughout the second half of the twentieth century, several *high* energy linear colliders were used to study fundamental particle physics. So of them are still in operation and this section gives a short history of how these accelerators came to be and what they are used for.

The first linear accelerator at CERN ran its first beam in 1958 and was fully commissioned in 1959 when one turn of 50 MeV protons went round the Proton Synchrotron (PS). It was the only supplier of protons to CERN's circular accelerators until the Linac 2 took over in 1978. The Linac 2 has not only continued to supply protons for other experiments, it was also used to accelerate alpha particles, deuterons, oxygen and sulphur ions over the years. In 2007, a replacement of this accelerator was approved. The new Linac 4 accelerator will provide a 160 MeV H-ion beam, as an injector to the PS Booster [7].

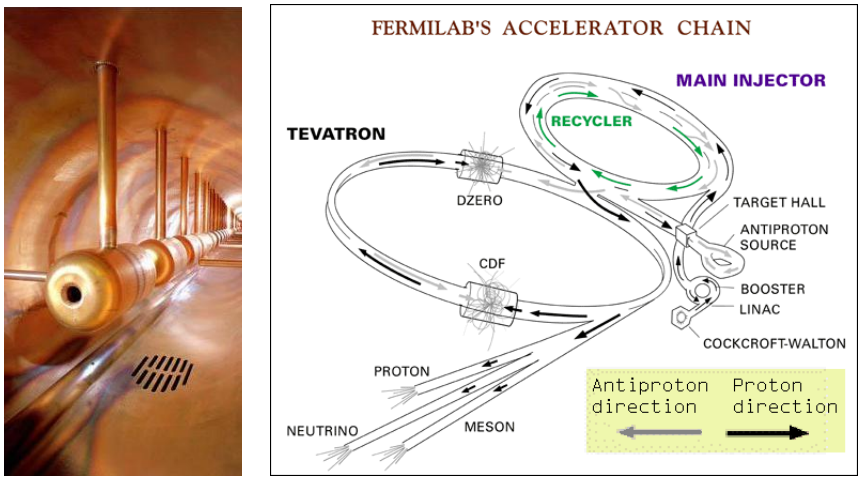

(a) (b)

Figure 2.4: (a) Photograph of the Fermilab linac and (b) an overview of the Fermilab accelerator chain

The Fermilab facilities west of Chicago house a circular particle collider called Tevatron. While the Tevatron, after years of service, was shut down on 30 September 2011, other experiments will continue at Fermilab, one of the intermediate accelerators being a linac. The Fermilab linac is 500 ft (or 152.4 m) long and accelerates protons coming from a Cockcroft Walton pre-accelerator to 400 MeV, which is about 70 percent of the speed of light. It provides (via an intermediate step) a neutron beam for cancer treatment, a proton beam for the MuCool test area (used to develop accelerator components for a future muon collider) and a proton beam for the Booster accelerator and the rest of the chain of accelerators [8]. A section of the linac and its position in the chain of accelerators at Fermilab is shown in Figure 2.4(a) and 2.4(b) respectively.

Figure 2.5: Aerial photo of the SLAC National Accelerator Laboratory, with detector complex at the right (East) side

The longest of linacs is the Stanford Linear Collider (SLC) with its 2 mi. (3.2 km) and it is the input for many experiments that have been or are conducted at the SLAC National Accelerator Laboratory. The facility is located on Stanford University-owned land on Sand Hill Road in Menlo Park, California, just west of the University's main campus. This laboratory was previously know as the Stanford Linear Accelerator Center (SLAC), but was renamed in 2008. Founded in 1962, the linac was finished and started operating in 1966 and has been operational ever since, accelerating electrons and positrons to 50 GeV for various experiments. The RF linear accelerator is buried 10 meters beneath the ground, passes underneath the Interstate Highway 280 and is claimed to be *the world's straightest object*. The klystron gallery atop the beam line is the longest building in the United States. Several Nobel prize winning discoveries have been done here, namely a study of the quark structure inside protons and neutrons and the discovery of the charm quark and the τ lepton. Eventually high energy physics was dominated by Tevatron and LEP and now the LHC, but the high polarization of the electron beam at SLC, close to 80 percent, made certain unique measurements possible [9].

2.3 Linear collider alignment

Alignment requirements are getting stricter for each new generation of linear colliders. Fortunately, research for more and more precise alignment over longer and longer distance has kept pace with the requirements. Several systems that have been used in the past or will prove to be the aligners of coming linear colliders are briefly explained below.

2.3.1 The Large Rectangular Fresnel Lens System

The operation of the Large Rectangular Fresnel Lens System (LRFLS) system is shown in Figure 2.6. Divergent, spherical waves, i.e. light, from

a laser impinges on Fresnel lenses which can be inserted in the optical path one by one, e.g. at T or M. Relative displacements of their image (Fresnel lenses give images because of the in-continuities in the lens surface) can be measured at the far end D. At SLAC, the whole system is in 12m vacuum tube sections and this vacuum set-up is also a support structure for the entire 3 mi. linac. The resolution of this system depends on: the size of the diffraction limited images $w \approx \lambda s/D$ (D is the effective width of the lens), the ability of a scanner/ image sensor to locate the centroid of an image, and the optical lever arm $(r + s)/r$. The resolution of the midspan, the most difficult region, of the 2 mi. long system is about 25 μm [4]. The largest systematic error creeps in at the transfer of the lens coordinate to those of the accelerating elements. Mechanically switching the lenses also introduces errors. The largest improvement done so far has been the replacement of the initial scanner with a CCD image sensor with digital output.

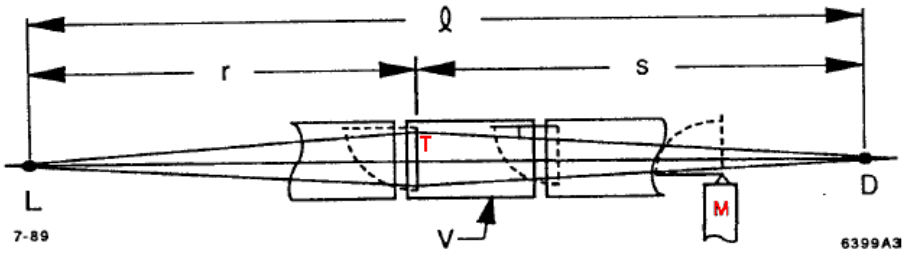

Figure 2.6: Schematic illustration of the Large Rectangular Fresnel Lens System used at SLAC. A 2mi. (3 km) version has kept it aligned for 20 years

2.3.2 Poisson Alignment Reference System

An explanatory illustration of the Poisson Alignment Reference System (PARS) is shown in Figure 2.7(b). The laser beam is optically blown up to a plane wave beam of larger diameter (see Figure 2.7(a)) and this light illuminates the spheres. In the wake of the sphere, diffraction causes a *Poisson spot* to emerge and this spot (and the pattern around it) can be used for position and shift estimation. One can mechanically switch between these spheres like Figure 2.7(b) shows, but spheres not positioned in each others optical path is also possible. Based on results from a 26.5 m long prototype exhibiting submicron resolution, simulations indicate that 2 μm is possible at 300 m [10]. Readout of many spheres is possible at kHz rates, but this amount of spheres is limited by the vacuum pipe diameter. As all alignment systems, the PARS is sensitive to (ground) vibrations since pointing accuracies of 20 nrad are required to obtain the claimed resolutions.

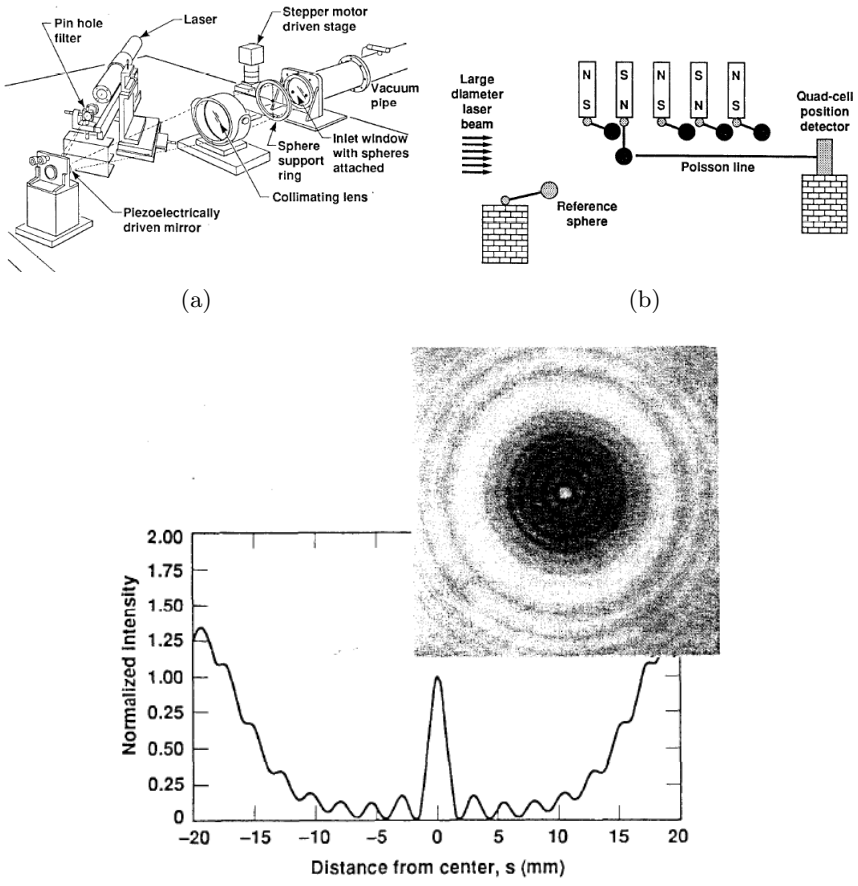

(a) (b)

(c)

Figure 2.7: (a) The Poisson Alignment Reference System light source, (b) an explanatory illustration of this alignment system and (c) an example image of a *Poisson spot* by a 25 mm sphere at 100m distance

2.3.3 Wire Positioning System

What is simpler and cheaper than a stretched wire, for the straight alignment of components? The Wire Positioning System (WPS) has played a role in aligning many of CERN's accelerators over the years [11]. One stretches a wire over the distance one would like to align and then there are two ways of reading the position of some sensor with regard to the wire. A change in the position of the wire changes the capacitance of the sensor-wire set-up in both directions perpendicular to the wire. This change in the capacitance can be measured by a capacitive sensor, which is basically an oscillatory RC or LC circuit. Providing a current to the capacitance charges it ($dV/dt = I/C$) and this rate of change of voltage across the capacitance results in the voltage reaching a threshold voltage. The frequency of the resulting oscillation is a measure for dV/dt and thus

for the capacitance. The capacitive sensor is empirically calibrated once so that the position of the wire can be deduced from the voltage readout for the remainder of the sensor operation.

This capacitive sensor and a wire running through it is shown in Figure 2.8(a). Innovations in various other fields, e.g. in fishing, have changed wire material over the years. The wire used at CERN nowadays is made a composite kevlar and carbon, called Carbon-Peek, and this material has good enough tensile and capacitive properties to perform position estimation over 140 m within resolutions of around 10 μm in the direction of gravity and even better in the other direction perpendicular to the wire. The largest systematic errors of the WPS are caused by air currents and gravitational sag of the wire, so research for putting the entire system in a vacuum or stronger wires should not go unexplored. The resolution is thus better for shorter system and submicron rms can be obtained for a 4 m stretched wire (V Rude 2012, pers. comm., 7 February). If wires are found with better tensile, but worse conductive properties, an optical method for the WPS readout is also possible [12]. An array of LEDs flashes at the stretched wire and two cameras make a photograph at the same time. The cameras are both inclined at a 90 ° angle with respect to each other and a 45 ° angle with respect to the x and y axis, as is shown in Figure 2.8(b). The position of the wire can be calculated by comparison of the two pictures with roughly the same precision as the capacitive WPS. This system uses another type of wire, called Vectran. It has, just as the LRFLS and the PARS, the advantage that multiple sensors can be placed along the same reference line.

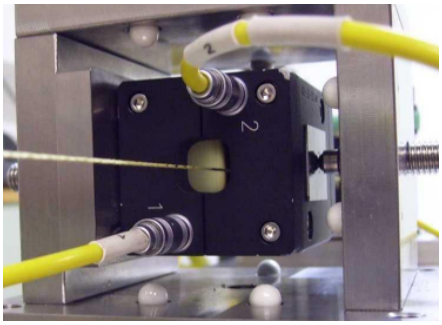

(a)

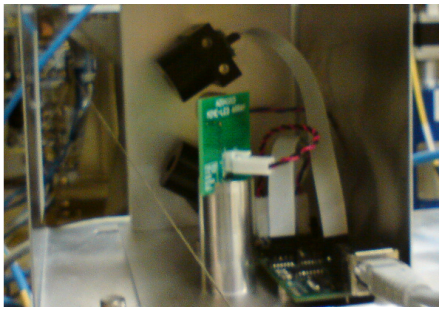

(b)

Figure 2.8: Photographs of a (a) capacitive sensor with a stretched wire running through it and (b) the optical WPS, where the array of LEDs is on the green circuitry board and the two cameras are directed at the wire at a 90 ° angle

2.3.4 Hydrostatic Level System

Measuring height differences between two points by reading of two interconnected cylinders filled with water has been conducted in the past and is still an alignment method used nowadays. The Hydrostatic Level System (HLS) has been used to align the Positron Electron Project (PEP) storage ring at SLAC (100 μm rms) in 1981 [13]. For CLIC pre-alignment the vertical uncertainty of the WPS introduced by the sag is measured by the HLS as well and this is investigated in TT1, an old transfer tunnel at CERN. Different fluids, in this case mercury, are subject to investigation at SLAC. There, the Final Focus Test Beam (FFTB) is hoped to be aligned up to micron accuracy over limited distances. Reading out the water level can be done in several ways, but mostly used is a laser shining from below on the water level. The reflected light falls on the side of water container and its height in the container wall is a measure for the water level and thus the relative position of the HLS unit. The earth's geoid not being smooth and time dependent is the largest source of systematic error in this alignment system.

2.4 The ILC and the CLiC

The two main proposed future linear colliders are the ILC and the CLIC. Both are electron—positron (e^+—e^-) colliders, but their designers have chosen for different techniques to accelerate these leptons. After the International Technology Recommendation Panel (ITRP) recommended a superconducting RF technology for a future linear collider, three existing linear collider projects – the Next Linear Collider (NLC), the Global Linear Collider (GLC) and Teraelectronvolt Energy Superconducting Linear Accelerator (TESLA) – joined their efforts into the ILC project. The CLiC is linear collider proposed and researched primarily by CERN. The proposed accelerating structures of the CLiC use a two beam — one main beam and a drive beam — solution. This drive beam technology is at room temperature (i.e. non-superconducting). Below, a description of the ILC and the CLiC and an overview of their differences are found.

A schematic overview of the ILC design is given in Figure 2.9. The ILC accelerator chain starts with an electron source, where 2 ns laser light pulses eject electrons from a photocathode. The electrons will then be accelerated to 5 GeV in a 250 m primary linac. The negatively charged leptons go into so-called damping rings, 7 km in circumference, in which the size of the bunches of particles is reduced to a few mm in length and less than 100 m diameter. The pulses are then fed to the final linac where they will be accelerated by superconducting Niobium structures to the final design energy of 250 GeV. A portion of the beam is diverted to collide on a titanium-alloy target, where synchrotron radiation from the incoming high energy electrons will produce electron-positron pairs.

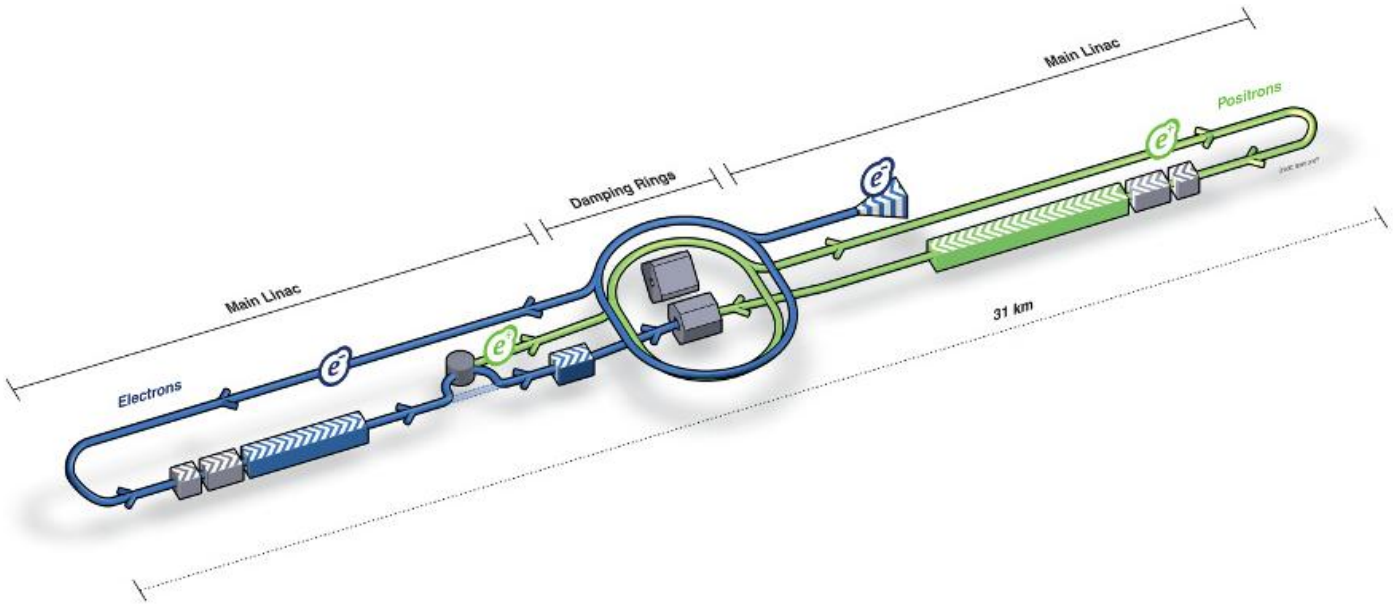

Figure 2.9: Schematic overview of the ILC design (not to scale)

The positrons of these produced pairs will be collected and accelerated to 5 GeV in a separate linac. These 5 GeV positrons are then fed to their own damping ring and subsequently fed to the other main linac, also accelerating the positrons to 250 GeV. The two 250 GeV beams meet each other at the interaction point to have a 500 GeV centre-of-mass linear collider. At the interaction point a *push and pull* design is implemented to accommodate for two different detectors.

The design of the CLiC is very different than that of the ILC, illustrated by Figure 2.9 with Figure 2.10.The CLiC uses an electron source as well as a positron source that are fed to (pre-)damping rings for bunching. Both beams are then accelerated to 6.14 GeV in a booster linac and then respectively fed to the e^- main linac and the e^+ main linac. This main beam could be fitted with a long klystron gallery, just as the SLC, but this would use a lot of power to achieve the needed acceleration and would come at a high price tag. A different solution is currently being investigated at the CLiC Test Facilities (CTFs) at CERN. Another beam line, called the drive beam, is parallel to the main beam at both main linac structures. This drive beam delivers a high intensity (about 100 A), low energy (2.38 GeV) pulsed electron beam to build high accelerating gradients (the amount of acceleration per meter). Such high gradients are easier to achieve with electric fields oscillating at high frequency. The drive beam accelerator makes use of klystrons at the start of the beam to obtain a high power GHz electron bunches for the drive beam. However, this concept uses less klystrons when a gallery is built along the entire linac. A frequency of 30 GHz, aiming to achieve a gradient of 150 MV/m

was selected for the 3 TeV design [15]. The drive beam is designed to be positioned 60 cm along side the main beam so that transferring power from a *high intensity-low energy* beam to the *low intensity-high energy* beam (the main beam) is efficient enough. Power Extraction and Transfer Structures (PETSs), passive microwave devices in which the bunches of the drive beam transfer their power to waveguides, are designed to convert the kinetic energy of the drive beam electrons to electric energy at the mode frequency. This oscillating electric energy is picked up by the bunched electrons (or positrons) in the main beam and those bunches are accelerated to a higher energy. This sequence is repeated along the entire main beam linac, accelerating the negatively (or positively) charged leptons to 1.5 TeV. The two beams meet at the interaction point at 3 TeV centre-of-mass energy.

There are a lot of differences in the design and technology used for the ILC and the CLiC. The technology involved in accelerating the charged leptons to high energies is very different for both colliders. A difference lies in the final focus of the beams that need to be achieved in order to get the desired luminosity at the interaction point, which is in the order of $10^{35}\ cm^{-2}s^{-1}$ or $10^{-4}\ fb^{-1}s^{-1}$. At the ILC, the final beam dimensions are in the submicron region, whereas the CLiC design demands final beam dimensions of several nanometers. Aligning beams of these sizes has never been done before and calls for more precise alignment systems than the ones described in §2.3. Another difference is that ILC uses superconducting technology, operating at a temperature of 4K, and the CLiC uses room temperature non-superconducting drive-to-main beam technology in order to achieve the final energies. While the ILC and the CLiC are comparable in size, the CLiC accelerates its particles to a centre-of-mass energy six times higher than the ILC. The gradient used in the CLiC (150 MV/m) used for accelerating the particles is more than 4 times as high as the designed gradient for the ILC (35 MV/m). In fact, if CLIC would use the same acceleration technology as the ILC, it would need to be 118 km long to reach its energy goal [14]. The larger gradient comes with a price: more research is needed for the cutting edge technology of the CLiC, whereas the technology of the ICL is already proven to a large extent. Essentially, both designs aim for the same goal: colliding electrons an positrons at unprecedented energies and this goal comes with a price tag over several billion dollars in both case. Thus, in the tight economic climate of today, it is unlikely that both colliders will be built.

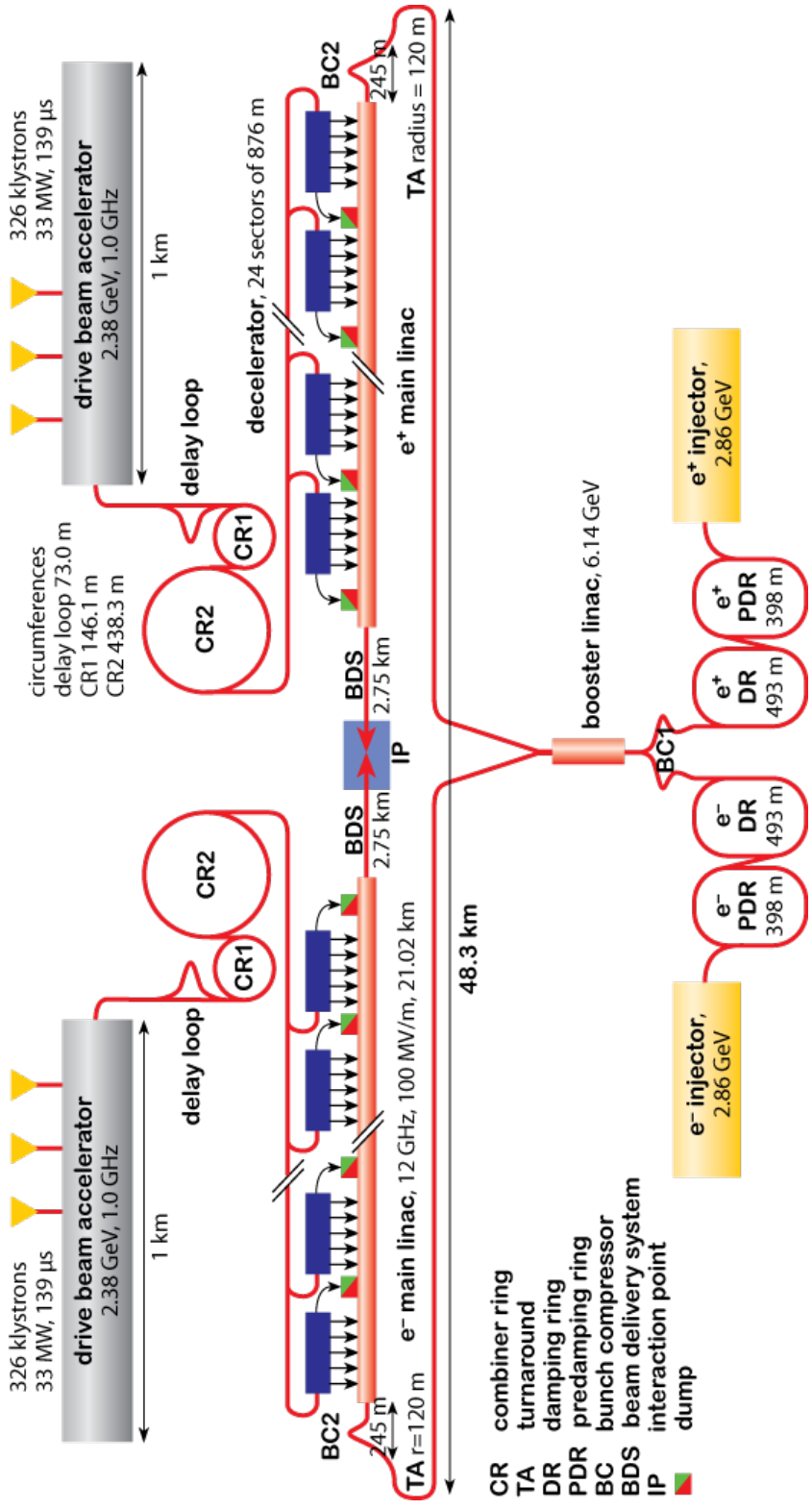

Figure 2.10: Layout of the the 3 TeV CLiC design (not to scale), from[15]

Chapter 3

Preferred alignment system

The alignment systems for linear colliders as presented in the §2.3 have proven their worth in the past. New criteria for the alignment of the CLiC have, however, created the need for even more precise alignment systems than have been built so far. The alignment of all the structural elements of the two linear accelerators has to be strict enough to prevent beam loss, e.g. beam from colliding with the pipe walls, which creates secondary emissions and radiation. When this *pre-alignment* is in order and two beams are delivered to the interaction point, beam based alignment can commence. The secondary emissions and radiation are monitored and, together with beam position monitors (BPMs), this provides data for beam based alignment. The beam is the *straightest* line in the entire collider, the beam being particles travelling at near light speed in a vacuum. The most used BPM looks like a tuning fork. The arms of the fork are actually coils in an LC circuit and any current flowing in the vicinity of these coils can be picked up by this resonant circuit. The charged particles in the beam are, in this case, the current. The readout of the two LC circuits is a measure for the beam position with respect to the two arms of the BPM. Two of these tuning fork like devices can determine the position of the beam in the directions perpendicular to the beam.

Section	Horizontal tolerance	Vertical tolerance
Final focus (bb)	4 nm	0.5 nm
Main beam (bb)	14 nm	1.5 nm
Drive beam (pa)	>100 μm	$\approx$ 1 μm

Table 3.1: Beam based alignment (bb) and pre-alignment(pa) criteria for the CLiC in the different sections, from a CERN report [15] and a 2008 CERN presentation [16]

Table 3.1 shows the alignment criteria for beam-based alignment for the linac and the final focus and pre-alignment criteria for the drive beam. This beam-based alignment can only take place if the linacs and final focus

are pre-aligned, because of beam losses encountered when the structure is not pre-aligned. The minimal pre-alignment criteria for the final focus and the main beam are three orders of magnitude larger (μm) than the criteria for the beam based alignment [15]. The (perpendicular)horizontal tolerances are looser than the vertical ones for the final focus and along the linac. This is because the designed beam size at the interaction point is 60nm x 0.7nm, where the horizontal size is a factor 85 larger than the vertical one. This kind of final focus at a particle beam has not been displayed in any particle accelerator or collider, e.g. in the SLC a beam diameter of 1.7μm x 0.9μm was achieved, which is three orders of magnitude larger than the designed *height* of the CLiC beam at interaction.

A combination of optical three point alignment systems is proposed by Nikhef to meet these demands. Already in 1988 in the L3 experiment at CERN a predecessor of today's system aligned the muon drift chambers of the detector [17]. More than 6000 of these systems are in use for the alignment and monitoring of ATLAS' (A Toroidal LHC ApparatuS) muon chambers. This line of systems is called Rasnik, which is an acronym for Red Alignment System Nikhef. This older version of Rasnik worked with a LED, a lens and a four quadrant diode (4QD). It made sure that the position readouts of passing muons where corrected for the relative positions of the drift chambers in the L3 experiment, shown in Figure 3.1.

Explaining the operation, the pros and cons and how these play a role in the pre-alignment of the CLiC is the purpose of this chapter. First the Rasnik, consisting of a LED-diffusor-coded mask light source, a lens and an ordinary pixel image sensor, is presented. Then another three point alignment system called Rasdif is explained, where the light source and lens have been replaced by a laser and a diffraction plate respectively. The chapter is concluded by an overview of several general implementations of both systems in the pre-alignment of the CLiC.

3.1 Rasnik

The idea for Rasnik has been around for about 30 years and has been subject to improvements ever since. The 4QD Rasnik was introduced in 1983 and it made way for the CCD Rasnik in 1993. The image of the LED was projected by a lens onto the four surfaces of the 4QD and a comparison of the relative intensity measured by each of the surfaces was made. This comparison allowed the Rasnik to determine the position of the spot on the 4QD. The CCD Rasnik is the Rasnik that is used nowadays and is explained and discussed in this section.

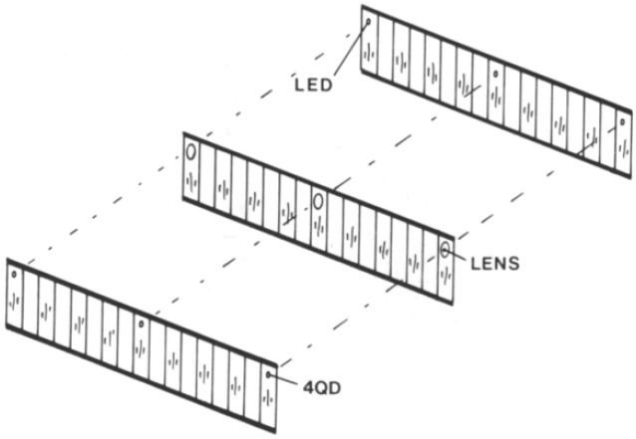

Figure 3.1: Rasnik three-point alignment systems in the L3 experiment, based on a four quadrant diode, from [17]

3.1.1 The Rasnik principle

The three points of the CCD Rasnik are occupied by a light source (consisting of a power LED, a diffusor and a coded mask), a standard plano-convex singlet lens and a pixel image sensor, as is shown in Figure 3.3. The chess-board-like mask, holding code, was invented by H. Groenstege (Nikhef). The image of this mask is projected onto a pixel image sensor. A coarse positioning code is embedded in the chess field pattern every 9^{th} row and column and is visible in the image sensor readout of Figure 3.3. This 9^{th} row or column hold a digital code used to determine which part of the surface of the mask is projected on the image sensor. The images collected by the image sensor are analysed by dedicated software. This software estimates the shifts in the different directions and rotations. In Rasniks, where the lens is in the middle between the light source and the image sensor, the lens has a focal length of one fourth of the total length of the system. These are the systems analysed in this thesis. Systems with the lens not in the middle are also possible. Here the image of the mask has a scale or magnification equal to $d_{lens-sensor}/d_{mask-lens}$.

Translations of all three points of the Rasnik have an effect on the position of the image on the pixel image sensor. Using the axis labels as defined in Figure 3.3, the x and y position shift the entire image and a shift in the z direction will be visible in the chess field size, because of a change in magnification or scale. Rotations of mask or image sensor around the z axis is visible as a rotation of the entire image. A rotation of the lens around this axis, however, will not appear in the image picked up by the image sensor. A reconstruction of the image by the image analysis software can be used to determine the rotation and shifts in the Cartesian coordinates. The typical Rasnik coding, embedded in the chess

field pattern, makes it possible for the software to recognise the relative location of the mask with respect to the lens and the image sensor every time the readout is started. If the image sensor and lens are fixed, i.e. a camera, with respect to each other, the absolute position of the mask with respect to this camera can be read out.

The diffusor between the LED and the mask is there to make the light incident on the mask homogeneous. Most LEDs used nowadays are so called *Lambert radiators*. In optics, Lambert's cosine law says that the radiant intensity observed from a Lambertian radiator is directly proportional to the cosine of the angle θ with respect to the LED surface normal. The diffusor itself is also a Lambertian surface. It produces a homogeneous background behind the mask, as the only image to be projected on the image sensor is the image of the coded mask and not that of the LED or something else. In fact, if one would use e.g. Fresnel lenses in stead of diffusors to homogenize a beam of light the LED—Fresnel lens combination has to be several centimetres behind the mask in order to lose the image of the Fresnel lens.

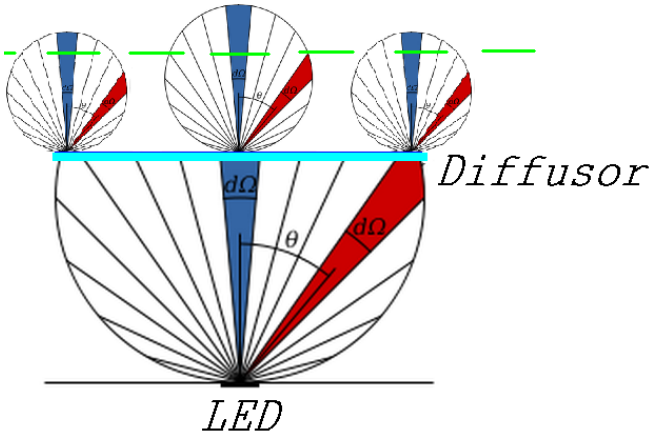

Figure 3.2: LED as a Lambertian radiator with diffusor as a Lambertian surface. The LED light is homogenized by the diffusor, but a small intensity bump at the surface to be presented to the mask (indicated in *green*) remains close to the normal of the LED surface

The choice of the lens diameter is a trade-off between enough light onto the image sensor and diffraction limited blurring effects on the one hand and limited image distortions and a larger depth of field on the other hand. Larger lens diameter result in more light on the image sensor and less diffraction blurring, which are first order effects. But, limiting this diameter by means of e.g. a diaphragm decreases the effect an important image distortion called the *pincushion* effect encountered when using singlet positive lenses. This is a second order refraction effect. Image magnification increases with the distance from the optical axis, because of rays of light travelling paths relatively far away from the centre of the

lens being refracted differently. This results in the image of the mask being magnified more at the edges of the image, like a pincushion. The increased depth of field by decreasing the diameter of the lens increases the range of the z measurement.

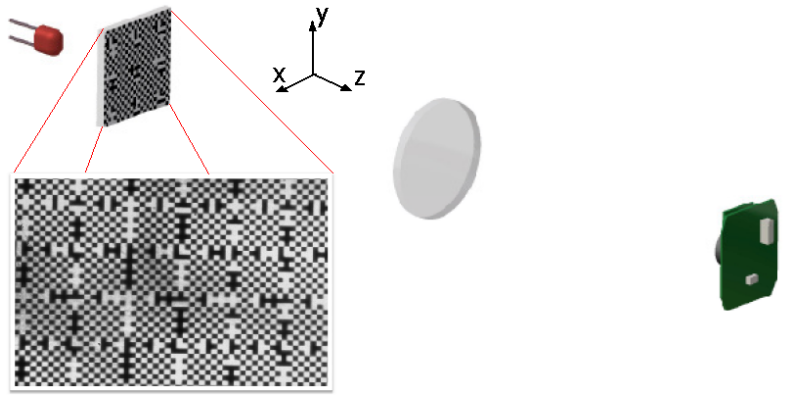

Figure 3.3: Overview of the Rasnik components

Rasnik systems can be scaled up without much difficulty, but the empirically it has been determined that the lens has to have a diameter of about 0.5 percent of the total length of the system. For example, a hundred meter Rasnik would require a lens with a diameter of half a meter and these are really expensive if not impossible to make. The pixel sizes of the used image sensors are in the order of tens of microns and the squares on the mask, called chess fields, have dimensions which are larger than this pixel size. The chess fields have to be more than about an order of magnitude larger in size as the pixels, because one must be able to distinguish the chess fields and the contours between the chess fields out the image produced by the image sensor. The pixels of the image sensor not being small enough is the first limit encountered when downscaling a Rasnik.

3.1.2 Rasnik image analysis

In the first Rasnik image analysis algorithms by F. Linde (Nikhef), the position estimation of a contour, defined as the black to white transitions around a chess field, is done in a way shown in Figure 3.1.2. A typical set readout of several pixels in one dimension is shown in Figure 3.4(a). A transition from a black to a white square is visible for a not infinitely sharp image. If it were infinitely sharp, the fittin procedure described below is also possible, but a practical example is given here. The position where the value of the fit is precisely in between the *black* and the *white* value is the used location of the contour. A shifted contour is shown in Figure 3.4(b) and the fit on the gradient gives a different position readout.

Typically, there is 200 mm contour length on a Rasnik mask. The

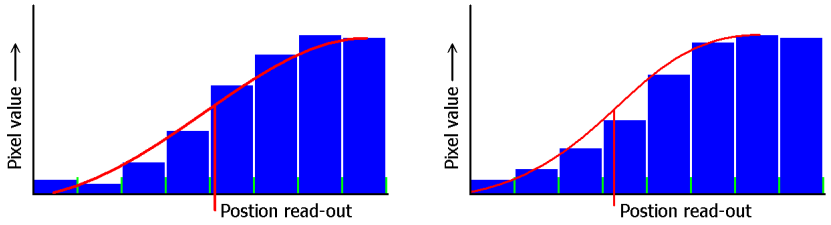

(a) (b)

Figure 3.4: (a) Pixel values at a non-sharp black to white contour and (b) a shifted contour and the subsequent different position estimation. The *green* intervals represent pixels, so one can imagine sub-pixel size determination of the position is possible

number of black-to-white transitions is given by following equation:

$$\#\text{ of transitions} = \frac{\text{contour length}}{\text{chess field size}} \tag{3.1}$$

The total number of transitions in the produced Rasnik image is typically 1000—4000. Averaging over the all contour fitting errors gives an output that has sub-pixel size resolution. More contours in an image improves this averaging, so a larger image sensor is an obvious solution for obtaining this. Large image sensors, however, may have a larger pixel pitch, defined as the amount of pixels per unit length in both dimensions. This pixel pitch is inversely proportional to the sharpness and at some point the image is smeared out to an extent that the fitting of a contour becomes less precise. Images degraded by noise can further compromise the quality of the contour fit. Reducing image noise and systematic distortion, without reduction of the depth of field, has been the subject of a large portion of the Rasnik research. Coping with noises and systematic errors has been a struggle for many years, but several people working on the Rasnik readout software have constructed various ways to handle this [18].

The shift and rotation estimation of an image can also be done by algorithms using Fourier analysis. This analysis does not calculate the position of every contour, but the chess field square wave nature in one dimension can be seen as a part of sine like functions of which the frequency and phase can be determined in Fourier space. The phase is dependent on the position of the image and is thus sensitive to shifts in x and y. The frequency is dependent on the chess field size, i.e. the magnification, and is thus sensitive to shifts in z. Rotations of mask and image sensor around the z axis rotate the entire Fourier image as well and can thus be determined. The sharpness of the harmonic peaks in Fourier space can show the amount of distortion in the image.

3.2 Rasdif

The original drive for development of the Rasdif was avoiding a large diameter lens for long alignment systems. The size of the diffraction plate is considerably smaller than the lens a Rasnik would need for a given system. The name Rasdif is chosen such to show that it belongs to the line of Rasnik systems, but that it uses diffraction to produce the images for alignment purposes. In 2003 this new member in the Rasnik family was proposed and a 91 m version of this system was introduced in the TT1 set-up at CERN in August 2006 [19].

3.2.1 The Rasdif principle

Replacing the LED and mask and the lens of a Rasnik with a divergent monochromatic light source and a diffraction plate respectively, one ends up with a so-called Rasdif, as shown in Figure 3.5(a). A laser is usually picked as a diverging monochromatic light source. A particular design of the diffraction plate produces an image on the image sensor that is a result of diffraction of spherical waves of light coming from the laser diode.

As is the case for Rasniks, translations in x or y of any of the three components of Rasdif appears as a shift of the image in that direction. A translation of the diffraction plate will appear as a twice as large translation in the shifted image. Translations of any of the three components in the z axis are more difficult to observe. Diffraction simulations done by R. van der Geer in 2008 show that the changes in the image are relatively small during translation in the z direction [20].

If the laser is a *perfect* point source that emits spherical waves, as in Figure 3.5(b), any rotation of the laser around the x,y or z axis has no effect on the image, as the waves are spherical and thus radially isotropic. The systematic effect that occurs when the laser is not a point source is described in §5.1.4. Different from the effect of rotating a lens of a Rasnik, rotations around the z axis of the diffraction plate rotate the entire image. Rotation of the image sensor around the z axis can be picked up in the same way as with Rasnik. Parallel operation of Rasniks and Rasdifs complement each other as both the point that holds the light sources and the point that holds the lens and the diffraction plate are sensitive to rotations around the z axis.

A different amount of chess fields in the image of a Rasnik system is obtained by changing the mask with one with a different chess field size. Altering the image of a Rasdif is done in a different way, which at first might seem contra-intuitive. All though diffraction of spherical waves is usually calculated in Fresnel or Fraunhofer diffraction theory [21], for this purpose it can be understood by a study of the one dimensional Bragg's law as well:

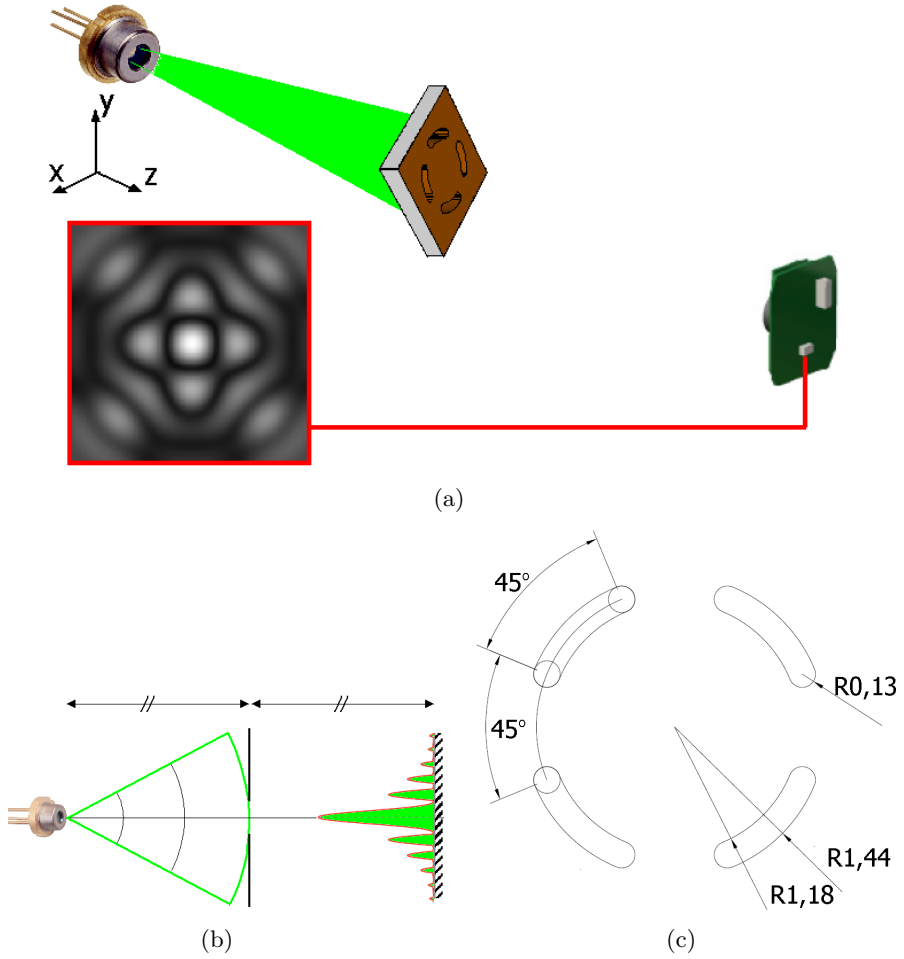

(a)

(b)

(c)

Figure 3.5: (a) Overview of Rasdif components, (b) the diffraction of spherical waves in one dimension and (c) a design of a diffraction plate in a 4 m Rasdif

$$\begin{aligned} 2d \sin\theta &= n\lambda \\ \sin\theta &= \frac{n\lambda}{2d} \end{aligned} \tag{3.2}$$

The $\sin\theta$ can be seen as a measure for the size of the diffraction pattern, because this determines where the maxima, i.e. the light blobs, are. From Bragg's law, it can be deduced that increasing the dimensions of the design of the diffraction plate will decrease the size of the diffraction pattern at the image sensor. The size of the diffraction pattern, however, is proportional to the laser light's wavelength, so red lasers (650 nm) give larger diffraction patterns than blue lasers (400 nm).

Considering the motivation for proposing Rasdif being the inability for feasible Rasniks to be scaled up to systems longer than couples of tens

of meters, Rasdif can be scaled up to larger distance. Modern lasers can nowadays provide coherent light up to kilometres meaning that, if systematic bending errors (§5.1.1) are (made) small enough and the diffraction plate size is chosen well, diffracted light can be delivered to an image sensor of a Rasdif of that size. In theory, there is no limit to the downscaling of a Rasdif, as long as the condition of a monochromatic divergent light source, emitting spherical waves of light, is met.

3.2.2 Rasdif image analysis

Rasdif analysis is done in Fourier space and is made by B. Bouwens (Nikhef). At the start of a position readout of Rasdif, the first image picked up by the pixel image sensor is saved and this image will be the reference image. Future images will be compared to this reference image and a shift in the x and y direction with regard the reference image is the output of the analysis software. This comparison is actually done by using the FFTs of the reference image (F_{ref}) and the to be analysed image (F_{im}) in an algorithm also used for automatic image registration purposes [22]:

$$\text{Ratio} = \frac{F_{ref}F_{im}^{*}}{|F_{ref}F_{im}|} \tag{3.3}$$

Applying the inverse FFT to this ratio results in an original images sized single array with values close to zero everywhere except for a small area around a single point. The peak in this small non-zero area is exactly at (v_x, v_y), the magnitude of the shift of the analysed image with respect to the position of the reference image. The precision of the fit on this two dimensional peak determines the quality of the software readout. Corrupted images, by random noises or systematic errors described in §5.1 and §5.2 respectively, compromise the operation of this algorithm. Off course, this algorithm also works on Rasnik images as FFTs are done on Rasnik images with the same ease. The absolute position information is not taken into account when using Rasdif software for Rasnik images, as the course position coding in the Rasnik chess field pattern is not *recognised* by the Rasdif software.

3.3 Rasnik and Rasdif for the CLiC

The two alignment systems described above can assist in the pre-alignment of the CLiC in different *areas*. Small systems (in the order of centimetres), intermediate sized systems (in the order of metres) and long systems (in the order of hundreds of metres) are needed for the CLiC pre-alignment and Rasnik and/ or Rasdif are able to comply with all these needs. Rasnik has proved its worth in other CERN alignment projects, such as the muon chambers for L3 and ATLAS, and improvement to the system has

been going on for 30 years. The projective optical alignment system is the preferred choice for small systems, except when the area available for the optical path is a critical point: the diffraction plate of a Rasdif is, for example twenty times smaller than a Rasnik lens for a 4 metre system. It can be used in CLiC for the small system alignment between the drive beam and the main beam, ensuring the correct distance between these beams. This is relevant as precise timing of the delivery of the electrons of RF beam to the accelerating cavities in the main beam is important, as described in §2.1. The CLiC design also demands alignment of 2m sections of the main beam as well as the drive beam and Rasnik as well as Rasdif can comply to these demands.

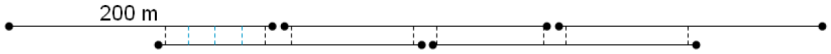

Figure 3.6: Schematic plan for overlapping long distance CLiC pre-alignment, from [23]

Rasnik starts becoming infeasible, in a practical as well as a financial sense, when system dimensions are above several tens of metres, mainly because this is more than four times the focal length of standard lenses. As Rasdif is scalable above these scales, it can provide a solution for the needed alignment over hundreds of metres. The configuration plan for this is shown in Figure 3.6 and is in need of long 200 m alignment systems, which overlap at half each others length. In order to make a Rasdif system for a specific problem, the size of the diffraction plate is not the only thing one can variate. The choice of the colour of the laser, i.e. the wavelength, also influences the size of the diffraction pattern, which is described above in equation 3.2.

The Rasnik and Rasdif systems to be implemented in CLiC can be put in a vacuum increasing their performance to tens of nanometre resolution. Vacuum complicates the mechanics and is usually expensive, so both optical alignment systems meeting demands without the use of vacuum is desirable. For short and intermediate sized systems, Rasnik (no vacuum) is less expensive than currently investigated alignment systems at CLiC mock-ups at CERN [15]. The ability to do multiple readouts per second of both Rasnik and Rasdif is key to the multi-Hz monitoring and subsequent active realignment intended for CLiC. The set-ups used to quantify the performance of the preferred optical alignment systems are described in the next chapter.

Chapter 4

Experimental set-ups

As CLiC alignment comprises of alignment over relatively short (60 mm), intermediate (2 m) and long (200 m) distances, performance of the optical alignment systems must be verified on set-ups with the same or comparable length. Research on the short Rasnik systems has been conducted in the past at Nikhef and sub-micron performance has already been obtained, so these systems are not investigated on a separate set-up.

At Nikhef (H038), a 4 m double Rasnik/ double Rasdif set-up was constructed in the beginning of 2011, where the systems are in parallel operation. In the course of the year, improvements were applied in several elements for both three point alignments systems. Taking learning from the results of the chromatic aberration and virtual point of departure studies (described in §5.1.3 and §5.1.4) different LEDs and lasers were installed respectively. Different diffraction plates and different pixel image sensors have been tried. The only thing that has not been altered in this set-up are the Rasnik lenses, with a fixed focal length of one-fourth of the total distance of the system.

At CERN, in an old transfer tunnel (TT1), a 140 m set-up is in operation for years. A set-up for comparing several alignment systems, namely the WPS and HLS (see §lincolal), were proposed to be built there in 2003 [24]. Between 2003 and 2005, the focus at CERN was more on the LHC, so only in 2006, the TT1 set-up was built. In that year a 91 m Rasdif system (called RasCliC) was installed and has been subject to improvements ever since. After a start with a single system, a second system was added. The two systems now monitored the full distance of 140 m. Different diffraction plates were made, the design following conclusions of a study by R. van der Geer [20]. As of November 2011, HeNe fibre coupled red lasers have been replaced by smaller green Diode Pumped Solid State (DPSS) lasers.

4.1 4 m Rasnik/ Rasdif set-up at Nikhef

The 4 m set-up is the first set-up where Rasnik and Rasdif are read out along side each other and the first time a Rasdif of this smaller scale is investigated. As the three points of alignment are on 2 m intervals, this set-up can evaluate the Rasnik and Rasdif performance on the intermediate CLiC alignment requirements. The set-up consists of 4 light sources, 2 Rasnik light sources and Rasdif 2 DPSS lasers, in the middle 2 lenses and 2 diffraction plates and at the end 4 pixel image sensors. Photographs explaining the configuration are found in Figure 4.1.

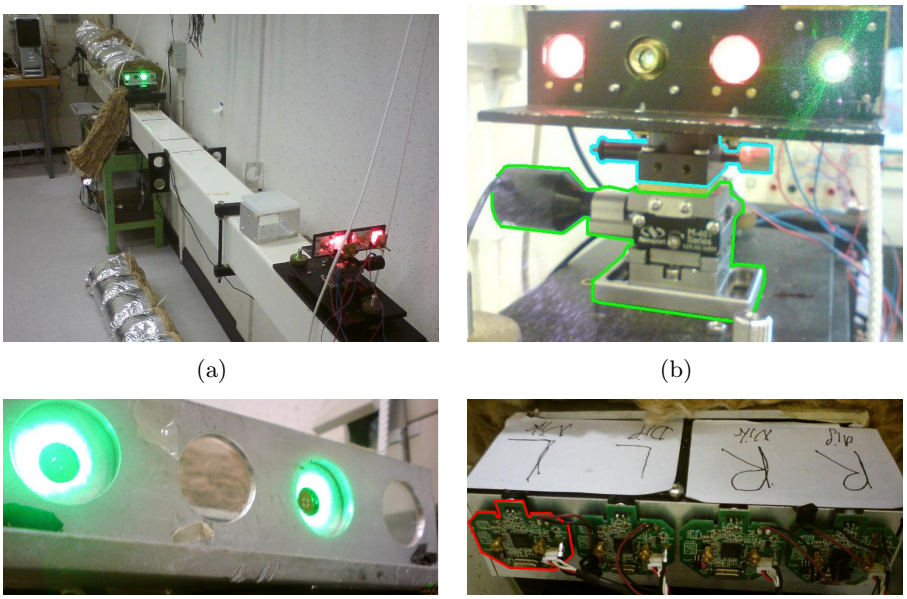

(a) (b)

(c) (d)

Figure 4.1: (a) Photograph giving a total overview of the 4 m parallel Rasnik/ Rasdif set-up with (b) 2 Rasnik light sources and 2 DPSS lasers, (c) 2 lenses and 2 diffraction plates and (d) 4 pixel sensors (viewed from the back). In (a), 2 m section of the thermal shielding is dismounted (lying on the floor) for understandability

In Figure 4.1(b) the light sources of both Rasnik and Rasdif are shown. All four of them are attached to an L-shape and this piece of metal can be fixed onto a set of actuators. One actuator is a small turntable (indicated with *cyan*) to apply rotations and the other actuator is an electric linear actuator (indicated with *green*) which can apply translations in the x and z direction. The turntable is used for investigating the location of the virtual point (see §5.1.4). The electrical sled of type Newport Newstep is controlled by a computer and is used to investigate the response of the alignment systems to applied transitions. With a computer interface, one can command translations precise up to the micrometre and set sequences

of translations via Labview interface built by F. Hartjes (Nikhef).

The Rasnik light source consists of a power LED, which is an array of small high power LEDs, a milk glass diffusor and the etched mask with the chessboard pattern. The Rasdif light source is a DPSS laser, which emits spherical waves of green light at 532 nm.

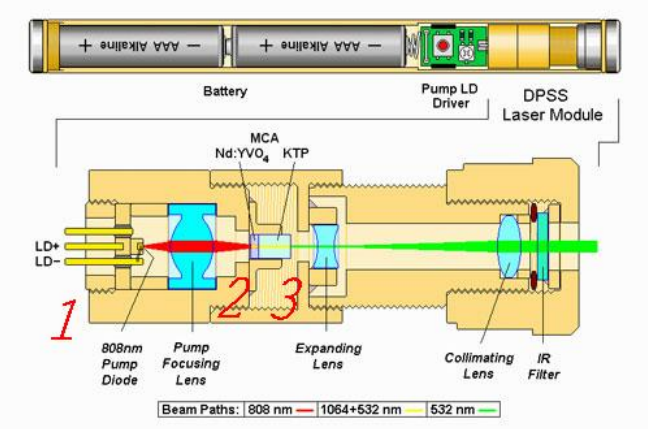

Figure 4.2: Schematic overview of a DPSS laser

.

The DPSS laser is obtained by opening an ordinary laser pointer of type Odicforce OFL147/001, with a similar composition as the overview showed in Figure 4.2. A diode which emits 808 nm near infra-red light shines its light on a so called pump medium. The pump medium, a small crystal (ND:YVO_4), converts this light to 1064 nm and this light is fed to a frequency doubler crystal (KTP). The doubling of the frequency results in the emitted light of half the wavelength: 532 nm. All of the optics to collimate the beam to a non-diverging beam is stripped off to the point where one is left with 1) the diode laser with the pump driver circuitry, 2) the pump medium and 3) the frequency doubling crystal. The lasers operate at a voltage of around 2.75 V with a current of about 350 mA.

Shown in Figure 4.1(c), the lens and diffraction plate holder are in the middle of the set-up. The lenses are Melles Griot simplex lenses of the type LPX-25.0-518.7-C, where the value 25.0 indicates the diameter of the lens in millimetre. The value 518.7 indicates the radius of the convex of the plano-convex lenses in millimetre, which are made of BK7 glass. The diffraction plates are made by Delta Mask and have the same design as the one shown in Figure 3.5(a). The design is etched out of a chromium mask with an outer radius of 1.44, and inner diameter of 1.18 mm and struts 0.26 mm wide. The pixel image sensor, shown in Figure 4.1(d) and indicated in *red*, consists of the inner circuitry and the pixel image sensor of a Logitech C300 webcam. Four of these sensors are fixed a holder, which has a *dark chamber* in front of the sensor to decrease background light.

4.2 140 m TT1 RasCLiC set-up at CERN

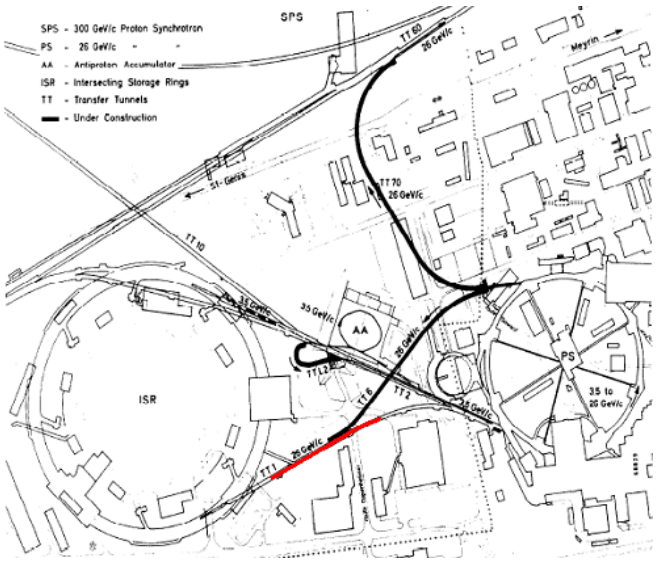

Figure 4.3: The used part of TT1 (in red) relative to underground structures at CERN. At the South side of the LHC, the Super Proton Synchrotron (SPS) is just visible on this map

.

The Transfer Tunnel One (TT1) at CERN, a tunnel where particle beams were transferred from the Proton Synchrotron (PS) to the Intersecting Storage Rings (ISR) until 1984 when the ISR was decommissioned, is home to a 140m test set-up (see Figure 4.3). This set-up was constructed to test and compare several alignment systems on same scale as the overlapping long distance alignment of the CLiC is designed. Today, the WPS and HLS and the so-called RasCLiC are read out along side each other, as shown in Figure 4.4. The RasCLiC is the Nikhef-built system for CLiC to complement these systems or to be compared to them.

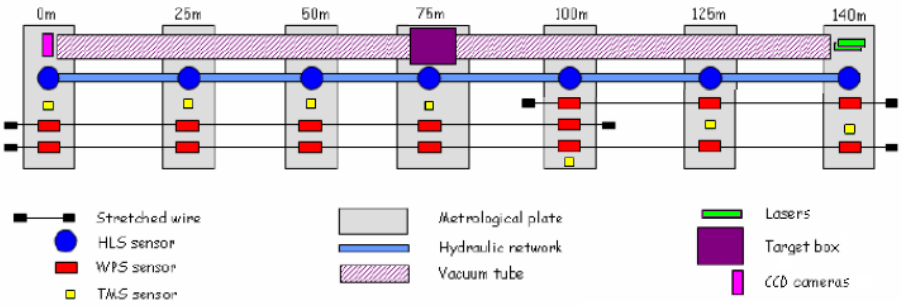

Figure 4.4: Schematic lay-out of the alignment systems in the TT1 set-up

The RasCLiC system is a double Rasdif over 140m, where the lasers

are at the North-East section of the tunnel at the start of the bending to the East. The two lasers are linked to the vacuum tube by means of bellows. A photograph of the laser side with only one bellow installed is shown in Figure 4.6. In previous operation, HeNe lasers, coupled in by fibers, were used as the light source for this system. Moving towards implementation of a larger number of systems in the future for CLiC alignment, smaller laser solutions to provide the monochromatic spherical light source have been installed. The *new* laser type is DPSS, emitting coherent green light at 532 nm, and has proven to have the desired characteristics for this set-up. It has a large intensity for its size, can thus easily be made to fit in a vacuum envelope, emits coherent (enough) light up to and beyond 140 m and the virtual point of departure of the coherent light almost coincides with the physical location of the crystal. The characteristic involving the virtual point is described in §5.1.4. In Figure 4.5 one see the North-East section of the vacuum tube: the laser side where the tunnel starts to bend to the East.

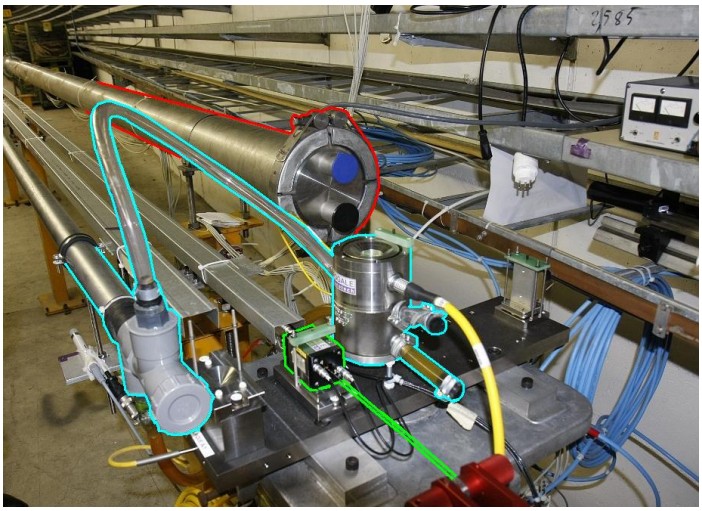

Figure 4.5: Photograph of the laser side of the TT1 set-up, *old* photo. The lasers are not yet installed here and the vacuum tube is sealed of with blue caps. One can distinguish a vacuum tube (red), the WPS (green) and the HLS (cyan)

The vacuum tube is a stainless steel tube with an inner diameter of 155 mm. At the laser side of the tube, two smaller tubes of about 10 cm are welded on. This makes installation of bellows to the individual lasers possible and makes it possible for the lasers to be in vacuum as well. Half-way down the tube flexible bellows are attached to ensure easy installation of the diffraction plate section. At the South-West side of the set-up, which is the pixel image sensor side, the tube is sealed off with an *optical window*. This optical window is a piece of transparent optical material that allows light into an optical instrument. Inside the vacuum

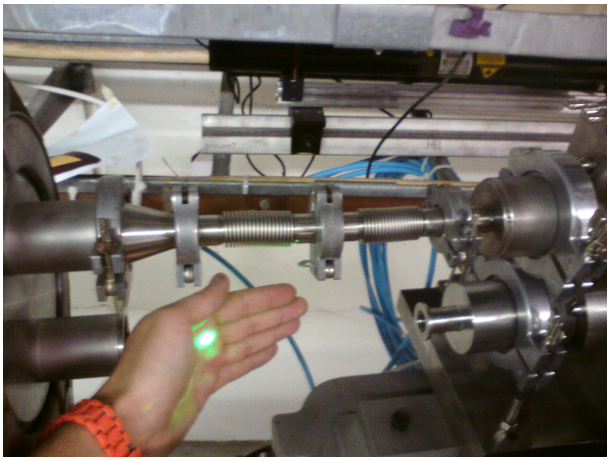

Figure 4.6: The two lasers of the RasCLiC, one linked to the vacuum tube

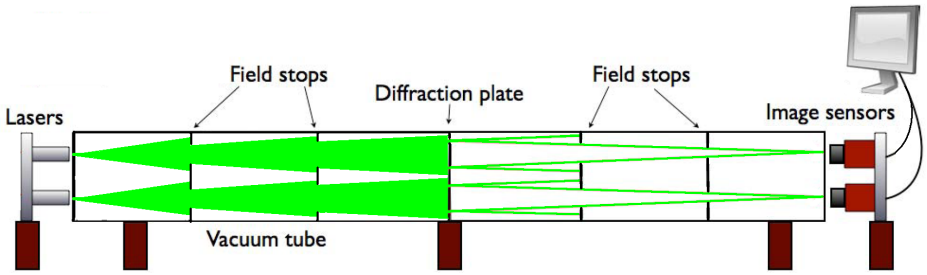

Figure 4.7: Schematic overview of the RasCLiC set-up, showing the operation of the field stops

tube, several field stops or diaphragms are installed. Figure 4.7 shows the location of these field stops of which, with variable size (larger diameter near the diffraction plate section), seven are located along the length of the vacuum tube. They have a *shark-teeth* shape to ensure that they do not have a well-defined diameter, which avoids unwanted diffraction, see Figure B.7(a). The field stops are installed to get rid of interfering reflections in the vacuum tube that would fall om the diffraction plate or the pixel image sensor. Attached to the vacuum tube one can find three pumping groups. These pumps are able to bring the pressure down to $1.5{\cdot}10^{-4}$ mbar in about three days.

In the middle of the set-up, a diffraction plate is placed to diffract the incoming light coming from the lasers. The plate contains two identical patterns with a similar, but up-scaled design as the Rasdifs in the 4 m set-up. Below one can see the design of one of those diffraction patterns (Figure 4.8(a)), a simulated diffraction pattern [20] (Figure 4.8(b)), a photograph of the diffraction plate holder(Figure 4.8(c)) and a photograph of the pixel image sensor image read-out on the PC (Figure 4.8(d)).

Using a pulley, a weight can be used to pull on the so called *plaque*, i.e.

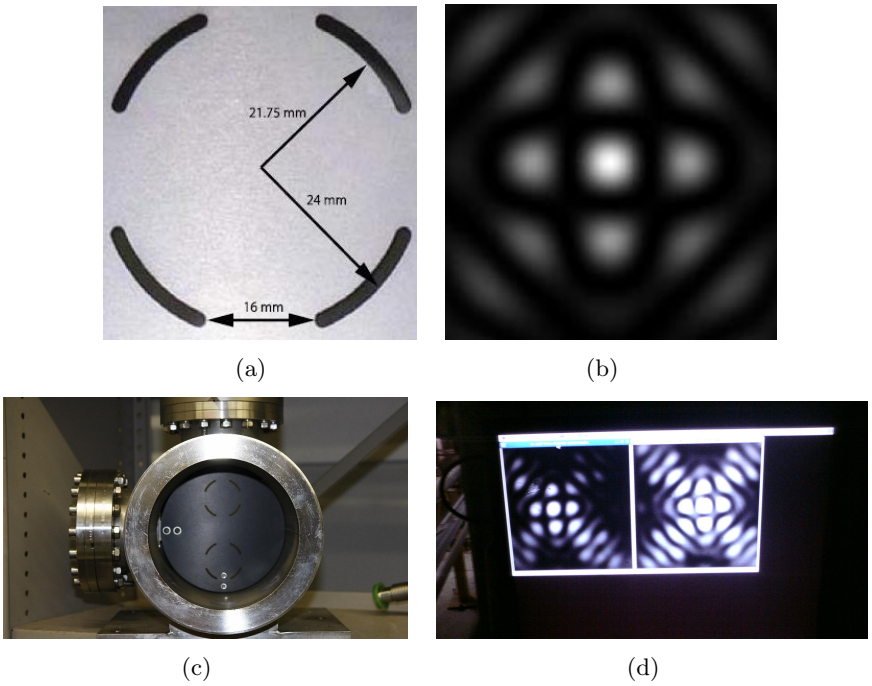

Figure 4.8: (a) Design and dimensions of the diffraction pattern, (b) simulations of the resulting diffraction pattern, (c) a photograph of the plate holder and (d) a photograph of the pixel image sensor read-out at the PC

the platform the diffraction plate holder is on. This way, translations in the horizontal direction perpendicular to the optical path can be applied. The WPS is also on the same plaque and thus initial comparison studies can be performed this way.

The side where the read-out of the system takes place is the side where two PIKE F100B Fiber from Allied Vision pixel image sensors and the PC are. Through the perspex plate sealing the vacuum, these pixel image sensors pick up the diffraction pattern. At full resolution, the pixel image sensors can operate at 100 frames per second. They can be adjusted in position in height, but are bolted to a fixed plate. This means adjustment in the horizontal dimension is not possible, but the position of the diffraction plate and the laser can be adjusted in this direction. The position of the diffraction image on the pixel image sensor is thus tunable via other ways than moving the pixel image sensors themselves.

Chapter 5

Sources of error

As can been seen in Table 3.1, there is room for error with the pre-alignment of the CLiC, albeit in the order of 1 μm. Analysis of all the different errors can provide understanding of the system and ideas for system design improvement. As is usual in statistics, errors are subdivided into two categories: systematic errors and random errors. In general, systematic errors *always* occur with the same value if the instrument is used in the same way. *Random* errors vary from observation to observation. In the case of optical alignment systems, systematic errors are generally introduced by the physics involved in light passing through several media, be it glass or air. Some components of thermally introduced errors in the light path have a random nature, but this distinction is not described. The *pure* random errors find their origin in the source of light and the device used to collect the light, i.e. the pixel image sensor. Together with the resolutions provided by the image analysis software, these errors provide an upper ceiling of the maximum resolution the optical alignment systems can achieve.

The systematic errors of both optical alignment systems are explained, followed by the random errors. Because an improvement to several systematic error is to shield the optical path with an isolated duct a shielding study by R. Rosing (Nikhef) of this solution is presented. The knowledge of the errors, assisted by an image analysis routine, is used to calculate the *Cramér-Rao Lower Bound* (CRLB), providing an indication of the performance of the shift estimation software and the amount of systematic error. The combined random errors are already dealt with in the CRLB.

5.1 Systematic errors

Light doesn't travel along a straight line through a medium across which a thermal gradient is present, which results in a density gradient. This is known as the refractive bending of light and imposes a offset to the location of an image. The density gradient results in a gradient in the

refractive index of the medium. Varying thermal conditions in the light path can shift the position of the image. Another phenomenon resulting in a variation of the position of the image is thermally induced jitter is discussed. Systematic errors specific to the different alignment systems are explained at the end of the section: chromatic aberration (Rasnik) and the virtual point of departure (Rasdif).

5.1.1 Refractive bending of light

In a thermal gradient spanned medium light travels along a region where the refractive index changes continuously in the direction perpendicular to the ray's path. This gives for the gradient shown in Figure 5.1 an offset in the opposite direction of the gradient. Derivation and quantification of this effect is given below [10].

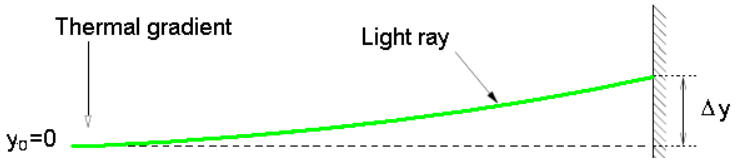

Figure 5.1: Refractive bending of light ray subject to a thermal gradient

If only deviations in the vertical (y) direction are considered, the index of refraction can be written as a function of y:

$$n(y) = n_0(1 - \epsilon y) \tag{5.1}$$

In equation 5.1, $n_0\epsilon$ is the gradient in the refractive index. This gradient finds its origin in thermal gradients and, to less extent, pressure gradients. The differential equation of a light ray is $d/ds(n\ d\vec{r}/ds) = \nabla n$ in vector form, where s is the path's length and $\vec{r}$ the amount of bending. In the case where only deviations in the y-direction are considered, $s = z$ to good approximation and $|\vec{r}| = y$, so the differential equation is $d/dz(n\ dy/dz) = -n_0\epsilon$. For a paraxial ray starting on the axis $y = y_0$, where $n = n_0$, the solution to this differential equation is:

$$y = y_0 - \epsilon\frac{z^2}{2} \tag{5.2}$$

The ϵ is found using $A = (RT/p)(n^2 - 1)/3$, the Lorenz-Lorentz formula, which reads upon rearrangement:

$$n - 1 = \frac{3Ap}{RT(n+1)} = \frac{3A}{2R}\frac{p(y)}{T(y)} \tag{5.3}$$

The last step in equation 5.3 is made by noting that $n + 1 \approx 2$. The pressure and temperature, both dependent on the vertical coordinate, can be expressed to first order as $p(y) = p_0 + p'y$ and $T(y) = T_0 + T'y$, where

p_0 and T_0 are the conditions at the axis $y = y_0$ and p' and T' are the gradients in the vertical direction. The ratio $p(y)/T(y)$ can be Taylor expanded to:

$$\begin{aligned}\frac{p(y)}{T(y)} &= \frac{p_0}{T_0} + y\left[\frac{(T_0 + T'y)p' - (p_0 + p'y)T'}{(T_0 + T'y)^2}\right]_{y=y_0=0} \\ &= \frac{p_0}{T_0} + \frac{p'y}{T_0} - \frac{p_0 T'y}{T_0^2}\end{aligned} \tag{5.4}$$

Substituting equation 5.1 and equation 5.4 into equation 5.3 and noting that $n_0 - 1 = (3A/2R)(p_0/T_0)$:

$$\begin{aligned}n_0 \epsilon y &= \frac{3A}{2R}\left(\frac{p_0 T'y}{T_0^2} - \frac{p'y}{T_0}\right) \\ \epsilon &= \frac{1}{n_0}\frac{3A}{2R}\left(\frac{p_0 T'}{T_0^2} - \frac{p'}{T_0}\right)\end{aligned} \tag{5.5}$$

With the values of n_0,p_0 and T_0 we can determine $3A/2R$. The values of refractive index for air n_0 is dependent on the colour (λ) of the light used, as seen in equation 5.6 [25] and is shown in Figure 5.2

$$\begin{aligned}n_0 - 1 = 8.3425 \times 10^{-5} &+ 2.4061 \times 10^{-2}\left(130 - \frac{1}{\lambda^2}\right)^{-1} \\ &+ 1.5998 \times 10^{-4}\left(39 - \frac{1}{\lambda^2}\right)^{-1}\end{aligned} \tag{5.6}$$

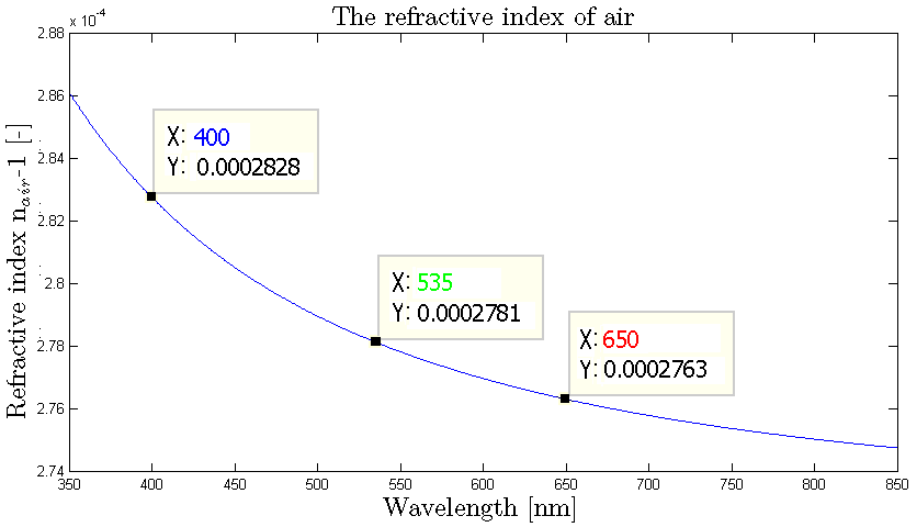

Figure 5.2: Refractive index of air versus wavelength of light at standard pressure and temperature

For example, for green ($\lambda = 535$ nm) light $n_0 - 1 = 2.781 \times 10^{-4}$, so at $p_0 = 1.0132$ bar and $T_0 = 293$ K the factor $3A/2R$ is equal to

$8.042b \times 10^{-7}$[K/Pa]. The pressure gradient for air is typically $-1.15 \times 10^{-4} p_0$/m and its pre-factor in equation 5.5 is typically smaller than the thermal gradient's pre-factor ($1/T_0 < p_0/T_0^2$), so it is generally a small contributor to refractive bending. Using equation 5.2, looking only at the influence of the thermal gradient, a 1 K/m gradient would bend a beam 7.59 μm over a 4 m path in atmospheric pressure. With $y \propto \epsilon \propto T'$, sub-micron bending of light over 4 m would require a gradient below the value of 0.132 K/m.

The refractive bending of light brings uncertainties for optical alignment systems. Changes in the local conditions can alter the position of the image, while the elements that are aligned by the system are not moving. That is why the refractive bending of the light of a system should be kept at a minimum, or at least in the range of the alignment criteria. The pre-factor of the thermal gradient in equation 5.5 shows that also the pressure can be lowered or the temperature can be raised for the air around the entire optical alignment system to decrease the refractive bending. This would mean the system would need to be in a separate volume in order to establish the wanted conditions and this would bring mechanical and financial consequences for the implementation of such a system. Lowering the thermal gradient at the optical path is feasible as the optical path can be isolated and is the discussed in §5.3.

5.1.2 Thermally induced jitter

The volume of air through which the ray of light traverses is proposed to be infinitesimally layered in the vertical direction in slabs with decreasing refractive index in the direction of the thermal gradient in §5.1.1. This is a static simplification of the dynamical process of infinitesimal air volumes, which all have small differences in temperature thus in refractive index. Small air flows, whether or not caused by local convection, give rise to a constantly varying medium through which a ray of light must pass in order to get from light source to pixel image sensor. The traversing of all these small volumes with different refractive index, which all move in the dynamical medium, means the endpoint of a ray of light, coming from a fixed point on the source, varies on the same time scale as the air flows. All the different rays of light coming from the light source, intended to produce a fixed image, thus produce a wobbling image. Because of convection and the constant flow of heat between adjacent infinitesimal volumes of air, there is the correlation between the location of the infinitesimal volumes and the refractive index. This and the fact that the images sent are large enough compared to the amplitude of the wobble of every different ray of light results in the the image not being distorted much but shifted constantly, i.e. wobble, instead. It does, however, decrease the sharpness of an image, which can be seen as small scale distortion. The wobbling of the images is known as thermally induced jitter, and, together with the

software analysis' resolution, is the main reason of jitter in the read-out of the different shifts and rotations of both Rasnik and Rasdif.

The temperature measurement of the entire volume in which the alignment system is an impossible task and thus modelling of the temperature and air flow in this volume is in order. The above description of the underlying fluid mechanics poses a problem in terms of the ability to model the phenomenon of this thermally induced jitter. Knowing the magnitude and location of every infinitesimal (convective) air flow seems of the room where the alignment system is located and what effect this all has on the envelope of the alignment system itself seems impossible, but measures can be taken to reduce the sources of convective air currents or the ability of air to flow through the envelope. A source of a convective air current can be a temperature difference between regions below and above the path of traversing light, i.e. thermal gradients in directions perpendicular to this light path. Isolating the light path of an alignment system by e.g. a isolating duct not only reduces these perpendicular thermal gradients, but also restrains air flows present to traverse the envelope of the light path.

Possible *rules of thumb* regarding this issue are found in astrophysics, because observational astrophysics has to deal with comparable problems. Earth's atmosphere is notorious for producing wobbling *images*, such as twinkling stars. A large difference between this problem and the problem discussed here is the pressure difference in the light path which is present when looking at the sky. This is the dominant contributor to the twinkling of the stars in a sense that the varying conditions and pressure induced air flows in the atmosphere result in varying refractive indexes along the entire path of light over time [26]. This difference makes the *rules of thumb* inapplicable to the *constant* pressure in the alignment systems considered in this thesis.

5.1.3 Chromatic Aberration

The refractive index of a gas or a material is dependent on the colour or wavelength of the light traversing trough, as is seen in Figure 5.2 for air. This phenomenon is called dispersion and the wavelength (λ) dependence of the refractive index of a gas or material is usually given by relations as equation 5.6. For most gasses or materials, this knowledge is accounted for by such empirically found dispersion relations. Schott BK7, a type of glass used for lenses also has such a dispersion relation with several (empirically found) constants given in equation 5.7 [27] and Table 5.1 respectively. This type of dispersion relation is called a Sellmeier series equation.

$$n_{BK7} = 1 + \frac{B_1\lambda^2}{\lambda^2 - C_1} + \frac{B_2\lambda^2}{\lambda^2 - C_2} + \frac{B_3\lambda^2}{\lambda^2 - C_3},\ \lambda \text{ in } \mu\text{m} \qquad (5.7)$$

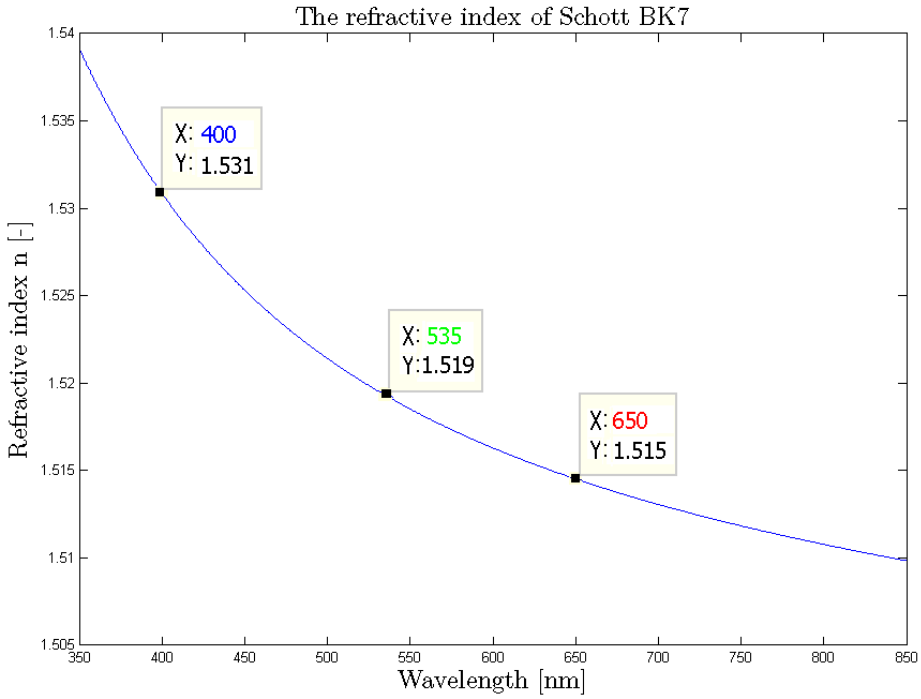

Figure 5.3: Refractive index of Schott BK7 versus wavelength of light at standard pressure and temperature

Constant	Value	Constant	Value
B_1	1.03961212	C_1	$6.00069867 \times 10^{-3}$
B_2	$2.31792344 \times 10^{-1}$	C_2	$2.00179144 \times 10^{-2}$
B_3	1.01046945	C_3	1.03560653×10^{2}

Table 5.1: Dispersion constants for the Sellmeier series equation [27]

The wavelength dependence of the Schott BK7 glass' refractive index is similar than that of air, as can been seen comparing Figure 5.2 and Figure 5.3. As both the refractive index of air and Schott BK7 are wavelength dependent, the angle of refraction of a ray of light incident at the interface of air (n_{air}) and Schott BK7 (n_{BK7}) is different for blue than for red light. Refraction of light is described by equation 5.8, which is called Snell's law. As the ratio $n_{air}(\lambda)/n_{BK7}(\lambda)$ is smaller for blue light (0.653) than for red light (0.660) when passing through an air-BK7 interface, blue light is refracted more (θ_2 is the angle with the normal) than red light. The fact that refraction is wavelength dependent is the physics behind the spitting of the colours when impeding *white* light on a prism and is called chromatic aberration or lateral colour.

$$
\begin{aligned}
sin\theta_2 &= \frac{n_1}{n_2} sin\theta_1 \\
sin\theta_{_{BK7}} &= \frac{n_{air}(\lambda)}{n_{_{BK7}}(\lambda)} sin\theta_{air}
\end{aligned}
\tag{5.8}
$$

A simple (planar-convex) lens has two interfaces, namely an air to glass interface and a glass to air interface. As precise ray tracing simulations, schematically depicted in Figure 5.4, show, the chromatic aberration phenomenon results in different focal points. In fact, the focal point of all simple (one material, simple geometry) lenses is given in a catalogue is for one wavelength only, a wavelength in the *green region*. These focal points are not precise in a sense that the three rays do not meet exactly at one point as this is only the case for the design wavelength. This is called spherical aberration this phenomenon is encountered for such simple lenses. A way of minimising the chromatic aberration is the use of composite lenses, made from two different materials each with opposite dispersion relations, i.e. inverse refractive index dependence relations with respect to wavelengths.

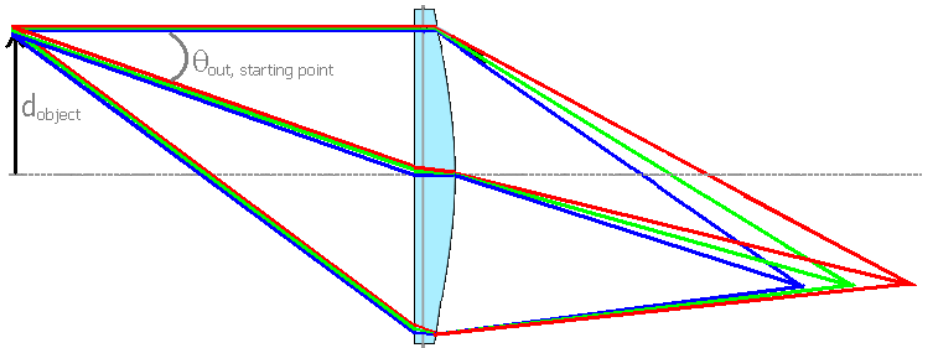

Figure 5.4: Ray tracing of light rays with different wavelengths through a planar-convex lens, chromatic aberration phenomenon exaggerated

With the Matlab routines included in Appendix A.1, one can calculate the intersection of the ray, started at top of the object with given angle with the optical axis ($\theta_{out,startingpoint}$), with a line perpendicular to the optical axis, i.e. the location of the image of the starting point. Two routines are included for reasons of cross reference checks, one with the planar surface and the other with the convex surface at the object side. These routines can be used to identify the *ideal* focal distance and object distance for a Rasnik. When the distance of the total system is known, the ideal position of the lens can be determined.

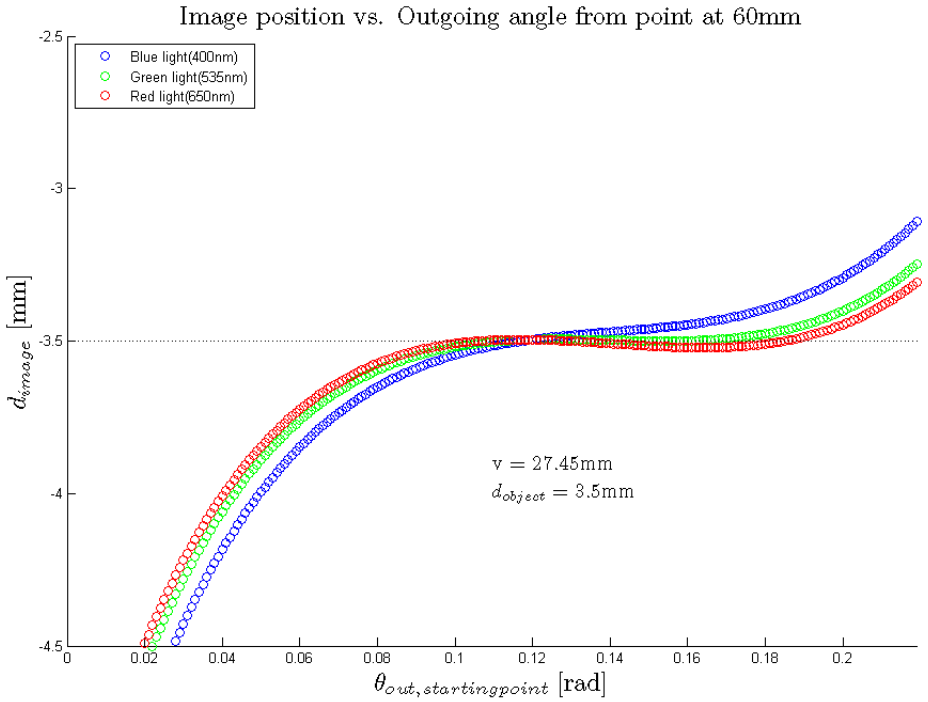

(a)

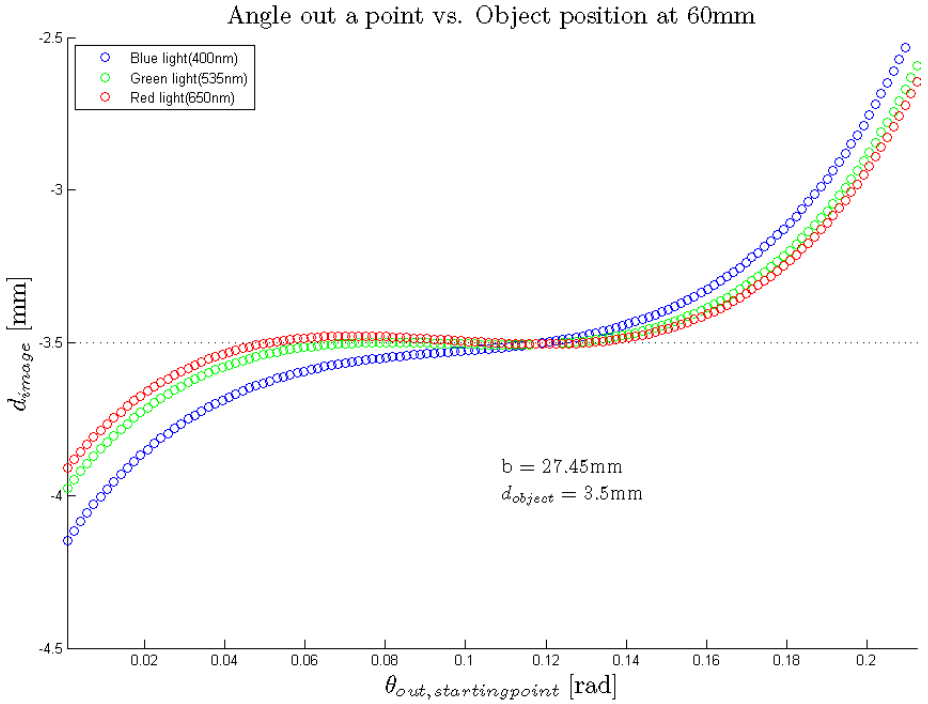

(b)

Figure 5.5: Ray tracing simulation for a 60 mm Rasnik with (a) the planar surface and (b) the convex surface on the light source side

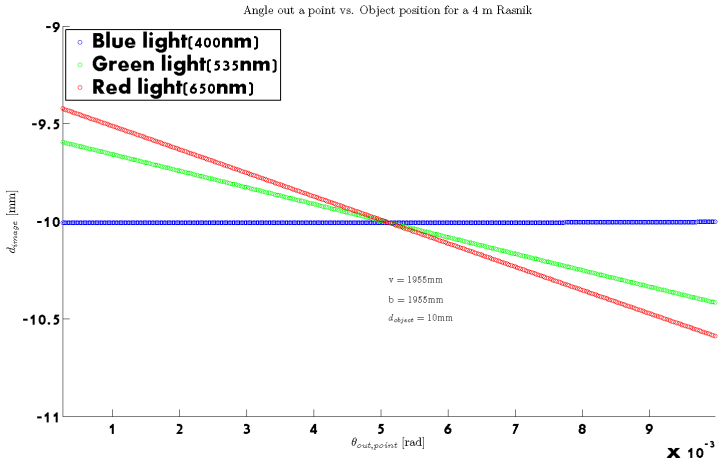

(a)

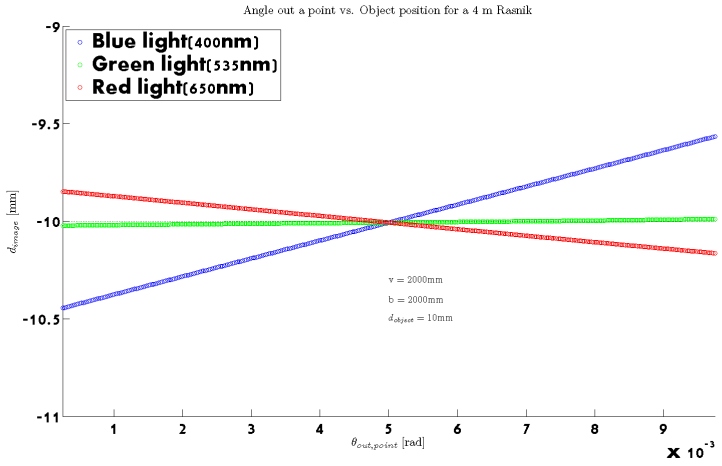

(b)

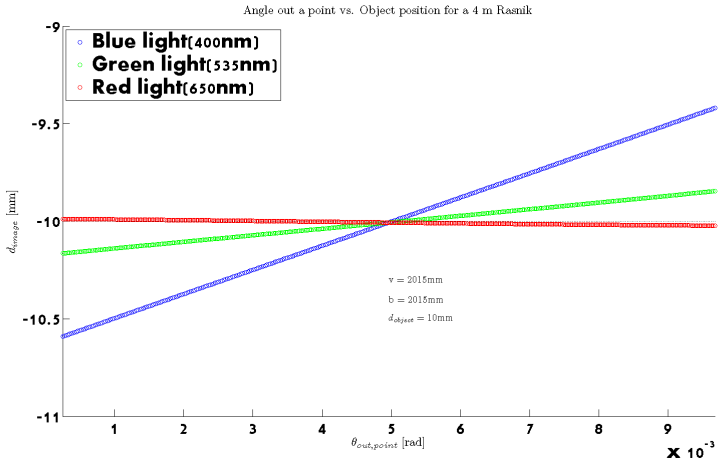

(c)

Figure 5.6: Ray tracing simulation for a 4000 mm Rasnik with the *ideal lens position* for (a) blue light, (b) green light and (c) red light

The relative depth in field of a Rasnik is constant when downscaling the system, so at some point it will be necessary to determine the *ideal lens position* more precisely. For a 60 mm Rasnik (a typical proximity system, as will be shown in §7.1.2) this is shown in Figure 5.5. Naively one would place the lens in the middle of a Rasnik as is usual when depth in field is ample to cope with this small systematic error, but the smaller Rasniks lack this needed depth in field. This is why more precise placing of the lens is needed and this *ideal lens position* can be provided by simulations like the ones in Appendix A.1. The graphs shown in Figure 5.5 both show that end points aren't falling on the desired value (-3.5mm in this case) and that blue light is refracted more in a sense that rays not going through the middle of the lens deviate more from the desired value than red rays.

For 4 m Rasniks similar simulations are possible and subsequent results are shown in Figure 5.6. The deviations from the desired value (-10mm in this case) are relatively smaller than in Figure 5.5, because the incident angles and thus the amount of refraction involved are orders of magnitude smaller than for the 60mm Rasnik. In other words, the usual spherical aberration consequences are less for large Rasniks than for smaller Rasniks. Again, whilst using the same lens, blue light is refracted more and this is visible in the smaller size of the whole system.

5.1.4 Virtual point of departure

The image Rasdif uses for shift estimation is an image that is produced by diffraction. The amount of movement (in X and Y) of the image is proportional to the transverse movement of the light source, just as this is the case for Rasnik. For Rasnik it is the movement of the mask which is measured, so the location of the LED and diffusor is unimportant as long as *enough* homogeneous light shines through the mask. Rasdif has a similar peculiarity as it will turn out that is not the movement of the physical location of the laser, but the so called *virtual point of departure* (VPoD) of the laser light, that is measured.

In Figure 5.7 an explanation and several consequences and solutions of the VPoD *problem* are shown. The finite size of the crystal of the diode laser creates a diverging beam emitting light which appears to be coming from a point source *behind* the laser, shown in Figure 5.7(a). The location of this virtual point source is the VPoD and, because it does not coincide with the physical location of the laser, the ratio of the distance between diffraction plate and image sensor and the distance between the laser and the diffraction plate is no longer 1. This ratio must be 1 for the shift of the Rasdif image to be the same as the shift of the light source, just as two persons who move the same distance (one up and the other down) on a see-saw must be at equal distance from the rotation point (the diffraction plate in this analogy).

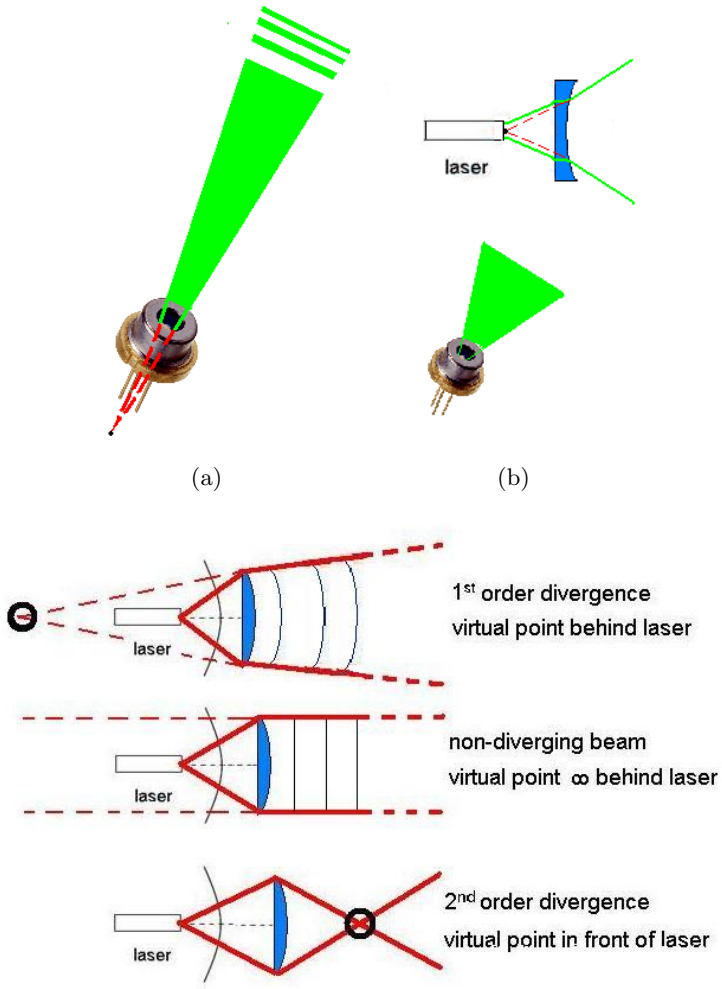

Figure 5.7: (a) The virtual point of departure for a typical diode laser, (b) possible solutions to make the virtual point coincide as close as possible with the physical location of the laser and (c) different divergences for a diode laser with optics

Possible solutions are shown in Figure 5.7(b): putting a negative lens in front of the diode laser making the beam more divergent and choosing a small laser diode with a small crystal but more diverging beam. The negative lens suffers from the same spherical aberrations for simple lenses as described in §5.1.3 making the VPoD a *virtual line of departure*, where the rays of light in the middle of the diverging beam have a VPoD which is more *behind or in* the laser than rays of light on the edges of the diverging beam. This effect is not expected to be very large, but the uncertainties involved with the catalogue divergences of laser diodes would mean introducing even more uncertainties when using optics.

The VPoD issue is discovered on the first configuration of the 4 m Rasnik/ Rasdif set-up at Nikhef, where other laser diodes than the current DPSS green lasers were installed in a prior stage of Rasdif development. These red diode lasers (type:HERO-PLP6501AR) have adjustable focus by means of a positive lens in front of the diode laser. Adjustment of this focus is found to have an effect on the slope of shift measurements, where the slope is defined as the actual read-out divided by the applied translation. In Figure 5.7(c) the effect of the adjustment of the position of the small positive lens with respect to the laser, i.e. the focus, is shown. The VPoD can be behind the laser, but also in front of the laser by so called second order divergence. If the VPoD is behind the laser, one can expect a smaller slope. Again using the see-saw analogy, if person (VPoD) is further away than the other (image on the pixel image sensor) from the rotation point and moves down, the other person on the see-saw moves up but with a smaller magnitude. This smaller magnitude of movement of the image results in a slope smaller than 1. On the other hand, if the VPoD is in front of the laser, the person moving down is closer to the rotation point and the slope is expected to be larger than 1. The DPSS laser now in both the 4 m set-up at Nikhef and the 140m RasCLiC set-up at CERN has a preferred VPoD which gives slopes around 0.98, as is shown in §6.1.1. The VPoD being close to the physical position of the laser is because the crystal emitting the beam has small dimensions (<1mm).

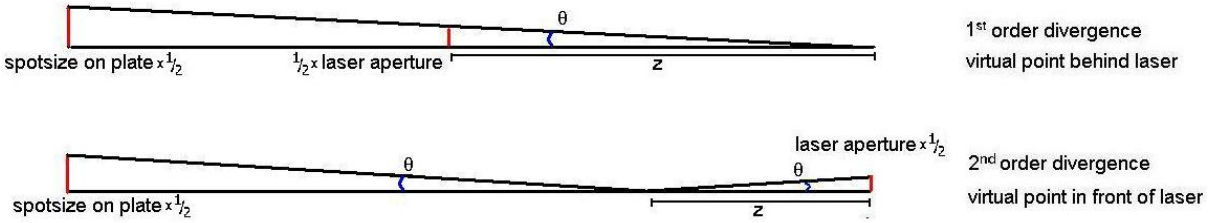

Figure 5.8: Simple geometrical model in order to calculate to first order the position of the virtual point of departure out of the known spot size

In the VPoD measurements conducted with the HERO-PLP6501AR red diode lasers the magnitude and adjustment of the divergence is done by measuring the spot size on the (region around) the diffraction plate. The effects of the VPoD being behind or in front of the laser and the magnitude of this anomaly were predicted using a simple geometrical model, which can be explained using Figure 5.8. The tangent of angle

θ is helpful here, because of the equal shaped triangles involved:

$$\begin{aligned} tan(\theta) &= \frac{\text{Laser aperture}}{z} = \frac{\text{Spotsize}}{d_{aperture-plate} + z}, 1^{st} \text{ order div.} \\ tan(\theta) &= \frac{\text{Laser aperture}}{z} = \frac{\text{Spotsize}}{d_{aperture-plate} - z}, 2^{nd} \text{ order div.} \end{aligned} \tag{5.9}$$

If the convention of a positive z for 1^{st} order divergence and a negative z for 2^{nd} order divergence is adopted, the slope can be calculated in the following way:

$$\text{slope} = \frac{d_{aperture-plate}}{d_{aperture-plate} + z} \tag{5.10}$$

Equation 5.10 shows the same behaviour as in the see-saw analogy. In case of a VPoD behind the laser the expected movement of the image is smaller than the translation applied to the laser itself, which is the slope, is smaller than 1. For VPoDs in front of the laser the slope is larger than 1.

Figure 5.8 also shows that if the spot size is small, the VPoD and the slope is further away from respectively the laser and 1. This implies asymptotic behaviour around the infinity of the VPoD being infinitely behind the laser for a non-diverging beam. This can been seen as a beam of plane waves incident on the diffraction plate and in that case translation of the light source doesn't have *any effect* on the waves as *seen* at the location of the diffraction plate. Measurements with both 1^{st} and 2^{nd} order diverging beams were done on the 4 m set-up at Nikhef to confirm this asymptotic behaviour and the results are shown in Figure 5.9.

As the applied translation is 1mm, the slope of the measurement is the value at the top of each pyramid in mm. These values can be plotted together with the model and this is shown in Figure 5.10. This graph is made using the Matlab code found in Appendix A.2.

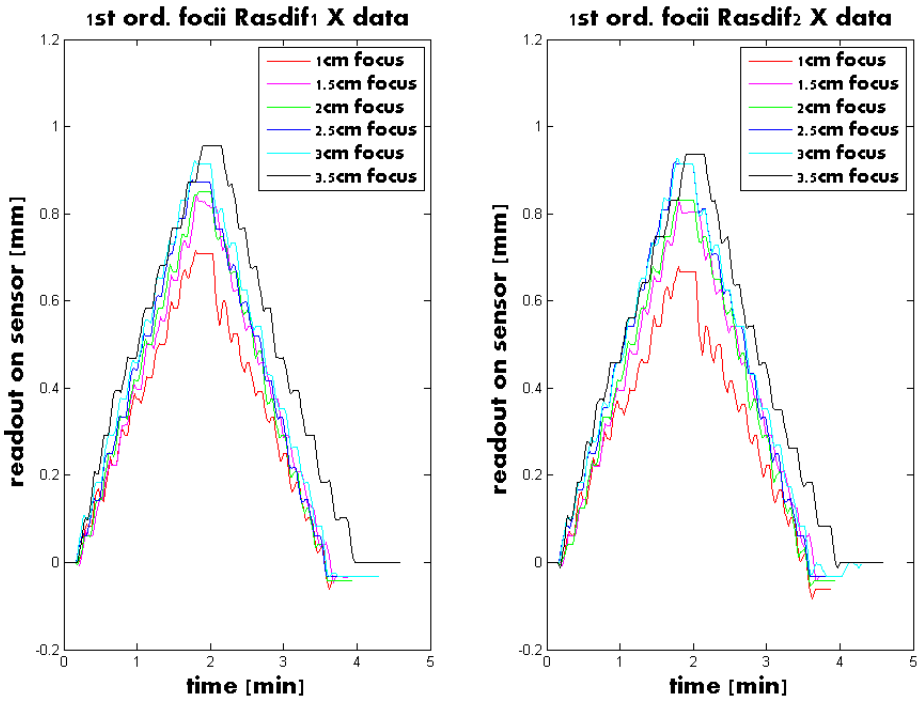

(a)

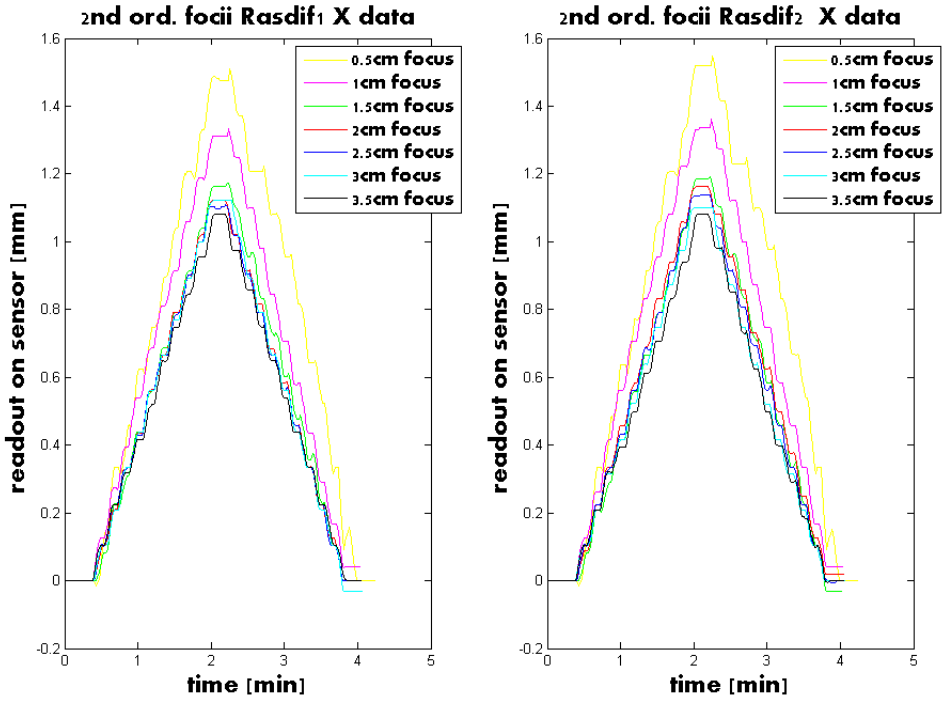

(b)

Figure 5.9: X read-out of 2 Rasdifs upon 1mm x translation back and forth in steps of 100μm of (a) first order divergent and (b) second order divergent beams

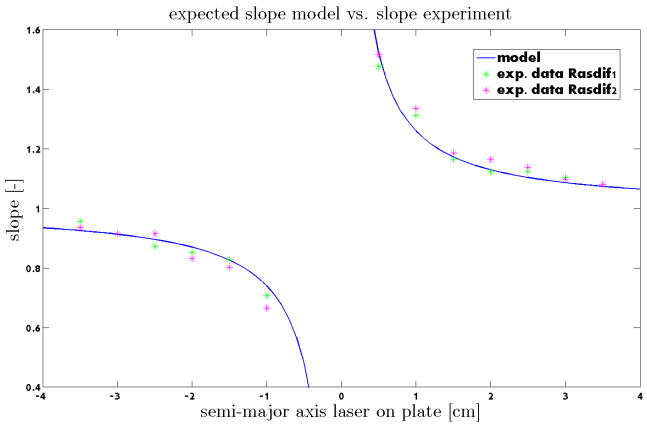

Figure 5.10: Slope measurements and virtual point model versus the laser spot size on the diffraction plate. To clearly show the asymptotic behaviour, the spot sizes for 1^{st} order divergence are given a negative value

The VPoD not coinciding with the location of the laser means that a rotation around the y axis of the laser will give a translation of approximately $z_{laser-VPoD} \times sin(\phi)$ of the VPoD. This is a first order approximation and only for small ϕ. Rotational measurements and comparison with an adapted version of the same model can be done and is shown in Figure 5.11, also produced by the Matlab code found in Appendix A.2. The smaller amount of data points is due to the small spot sizes being in de vicinity of the diffraction plate sizes, which resulted in the spot *falling of* the diffraction plate when rotation is applied.

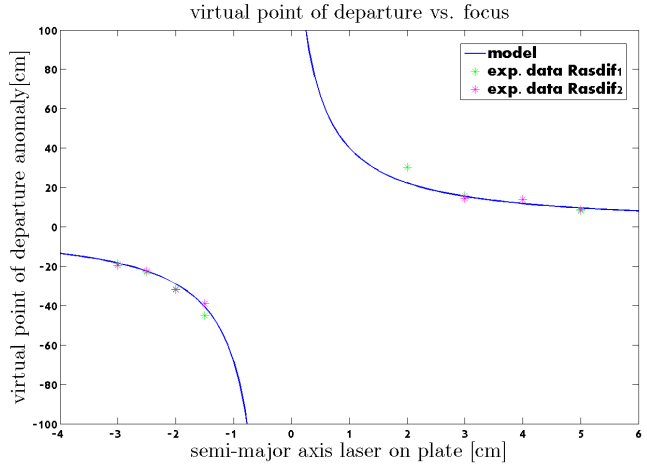

Figure 5.11: Rotational measurements and virtual point model versus the laser spot size on the diffraction plate

5.2 Random errors

The random errors in the optical alignment systems have their origin at the source or at the end point. Random errors are defined as errors that, based on the average of N samples, decrease by a factor $\sqrt{N}$. A brief explanation of the noise in the light source and the pixel image sensors is given below.

5.2.1 Noise in the light source

Rasnik uses a LED as light source in combination with a diffusor to provide a homogeneous beam of light to the mask. The (light emitting) diode is well understood in solid state physics and a common description of diode noises is divided in three types on contributions to the total noise [28]:

- Generation and recombination noise (G-R noise) associated with electron-hole generation and recombination in the junction
- Johnson or thermal noise associated with the capacitor like nature of the junction. The randomly fluctuating potential energy on it and variations in the thermal energy of the charge carriers (Brownian motion) result in a corresponding random kinetic energy component, which is the Johnson noise current I_J
- 1/f noise associated with the irreducible limit of the performance of the electric circuit. Because a true understanding of the physics behind it isn't made yet, it is just named *1-over-f noise*

The G-R noise is dependent of the current (I_{LED}) going through the LED over a time interval, the current being the source of the outgoing light, the charge of the charge carrier(q) and the efficiency with which is current is converted to light, the photoconductive gain (G):

$$\langle I_{G-R}^2 \rangle = \left(\frac{2q}{\Delta t} \right) \langle I_{LED} \rangle G \tag{5.11}$$

The Johnson or thermal noise over a time interval is, from thermodynamic considerations, proportional to $k_B T$, and inversely proportional to the resistance (R):

$$\langle I_J^2 \rangle = \frac{2k_B T}{R \Delta t} \tag{5.12}$$

The 1/f noise is ill understood, but many different phenomena appear to have nearly identical low-frequency noise behaviour:

$$\langle I_{1/f}^2 \rangle = \frac{K I^a}{f^b \Delta t} \tag{5.13}$$

In equation 5.13, K is a normalization constant, $a \approx 2$ and $b \approx 1$. Known contributions to the 1/f noise of are int. al. the fluctuation of the internal series resistance and a fluctuation of light caused, most probably, by a concentration fluctuation in the light-emitting region [29]. These three noise categories add quadratically, so the total noise is given by:

$$\langle I_{tot}^2 \rangle = \langle I_{G-R}^2 \rangle + \langle I_J^2 \rangle + \langle I_{1/f}^2 \rangle \tag{5.14}$$

The laser in Rasdif is also contains a (pumping) diode, so all of the above applies to the noise in that light source as well. The crystal in the DPSS laser used for the frequency modulation of the light introduces noises associated with atomic transitions of exited states is the crystal (the process that produces the modulated green light). The process of frequency modulation is not without losses and the heat produced here heats up the laser casing. The heating up of this casing, it not being (infinitely) symmetric, results in a translation of the diode and the crystal. This translation results in a subsequent translation of the *whole* laser beam and subsequently the image. The systematic error introduced here evolves exponentially to a stable state where the heat produced is equal to the heat emission to the structure around the laser and air around it.

5.2.2 Pixel noise

The pixel image sensor used in the 4 m set-up is the C300 Logitech webcam and uses CMOS technology. This technology uses complementary metal-oxide-semiconductor (CMOS) facilities where (silicon) photodiodes and their read-out circuitry produced on a single wafer. The PIKE F100B pixel image sensors used in the 140m RasCLiC set-up use CCD technology, which has most of its circuitry multiplexed not in the wafer itself, but on the sides or behind the semiconductor material. While there are intrinsic differences in the resistance of the pixels (CMOS pixels having a larger resistance, reducing Johnson noise), random noises that apply for both int. al. the dark current and variations of the photo response differing from pixel to pixel [28]. The dark current is mostly a result of thermally excited charge carriers, when no light is falling on the pixels of the pixel image sensor. Variations in the photo response of different pixels find their origin in the non-uniformity of the pixels, which seems impossible to solve. To make every pixel completely identical to adjacent pixels all over the surface of the pixel image sensor is beyond the technology used today to produce pixel image sensors.

5.3 Thermal effect of the conditions in the light path's medium

In order to decrease the thermally induced systematic errors described in §5.1.1 and §5.1.2 thermal insulation of the optical path is applied. An

extensive finite element study was performed by R. Rosing (Nikhef) in Abacus investigating the needed geometry and material of the thermal isolation. The goal of the isolation is to decrease the thermal gradient below the needed maximum gradient for sub-micron bending over 4 m of 0.132 K/m. The theoretical quantification of the thermally induced jitter is unknown, so a thermal insulation is applied to the 4 m set-up at Nikhef. The results of this empirical quantification are the subject of §6.2.1.

In R. Rosing's report [30], 4 different geometries of shielding are analysed using a thermal finite element analysis. The analysis is two dimensional, so it is assuming an infinitely long shielding. The 4 geometries analysed are:

- Circular cross section, outer radius 11cm, with 2mm aluminium rings and 22mm polyurethane *core* in between
- Square cross section, outer sides 22cm, with 2mm aluminium outer and inner structure and 22mm polyurethane *core* in between
- Rectangle cross section made to fit in the CLiC mock-up at CERN, , with 2mm aluminium outer and inner structure and 22mm polyurethane *core* in between
- Rectangle cross section modelled of the insulation that is applied on the 4 m set-up at Nikhef, 4.5 mm inner structure with a 5cm DIY store (Praxis) rockwool around it

The first two analyses were done in order to compare circular and square geometries with the same dimensions. The third analysis is done to quantify the design made for the RasChain set-up, described in §7.1.2, setting a maximum to the outer temperature difference that would still result in the 0.132K/m gradient at the optical path. The fourth analysis is done to get a feeling for the gradients present in the Nikhef 4 m set-up. This allowed for a *quantified* reference in terms of the gradient to the results obtained in this set-up.

The analyses of the circular and square cross sections proved that a circular cross section resulted in a slightly smaller thermal gradient over the inner volume. This difference in resulting gradient is of such small magnitude that for practical reasons, the design of the RasChain insulation has been given a rectangular shape. A result of the finite element analysis of the RasChain design is shown in Figure 5.12. This design, however, would fit in the volume envelope available for RasChain in the CLiC alignment mock-up, described in §7.1, but could not be installed due to it not being able to *slide in* the mock-up. Altering the 3 corners to be like the left upper *corner*, ending up with a hexagonal structure, solves this problem. This alteration is not believed to have large effects on the inner gradient, so the analysis is not redone. The conclusion of the analysis is that a maximum temperature difference of 0.74 K over the

outer surface is allowed to end up with the required 0.13 K/m thermal gradient in the inner envelope.

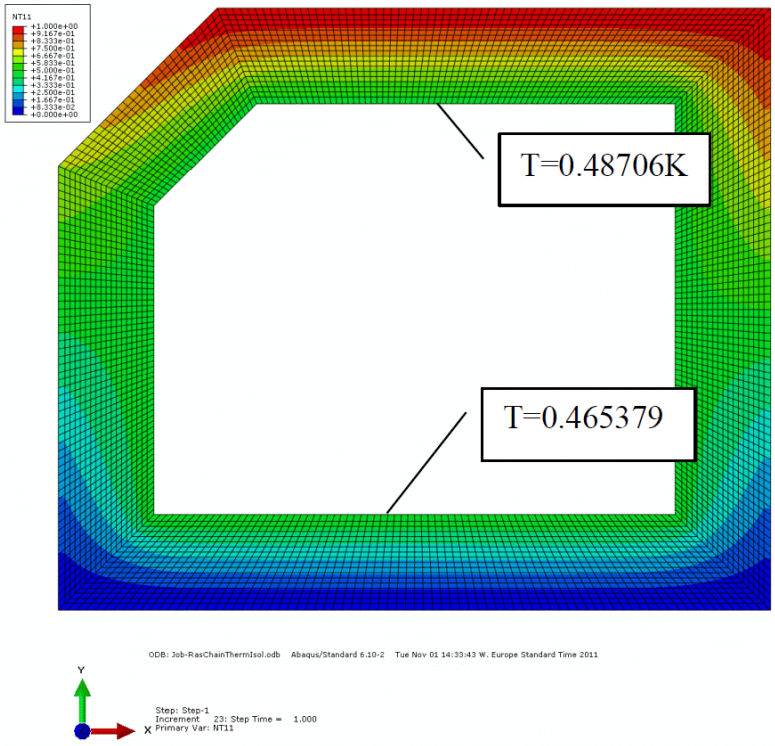

Figure 5.12: Thermal finite element analysis of the RasChain isolation design. The applied temperature difference is 1K from top to bottom

5.4 Cramér-Rao analysis

The mean squared error of any estimate of a deterministic parameter has a lower bound known as the Cramér-Rao Lower Bound (CRLB) [31]. The observations of random variable $\mathbf{y}$ have a probability density function $f_y(y,\theta)$, where θ is the unknown parameter. Then for *any* unbiased estimator $\hat{\theta}$ of the parameter , its covariance matrix satisfies the inequality [32]:

$$cov(\hat{\theta}) \geq F^{-1}$$
$$F = \mathbb{E}\left[-\frac{\delta^2}{\delta\theta^2} log\ f_y(y,\theta)_{\theta=\theta_0}\right] \tag{5.15}$$

The matrix F is called the Fisher information matrix (FIM). For two dimensional shift estimation the CRLB is a bit different [33]. The unknown parameter is now the shift vector $(v_x, v_y)^T$ (of the shifts $x' = x - v_x$

and $y' = y - v_y$) and the FIM is dependent on the image gradients. The image gradients are defined as $I_x = dI/dx$ and $I_y = dI/dy$:

$$
\begin{aligned}
cov(\hat{v}) \geq \quad & F^{-1} \\
F(v) = \quad & \frac{1}{\sigma^2} \begin{bmatrix} \sum_S I_x^2 & \sum_S I_x I_y \\ \sum_S I_x I_y & \sum_S I_y^2 \end{bmatrix} \\
F^{-1}(v) = \quad & \frac{1}{\sigma^2 \det(F)} \begin{bmatrix} \sum_S I_y^2 & -\sum_S I_x I_y \\ -\sum_S I_y I_x & \sum_S I_x^2 \end{bmatrix} \\
\text{, with} \quad \det(F) = \quad & \frac{1}{\sigma^4} \left[\sum_S I_x^2 \sum_S I_y^2 - \left(\sum_S I_x I_y \right)^2 \right]
\end{aligned}
\tag{5.16}
$$

The variances of v_x and v_y are on the *11* and *22* position of the covariance matrix respectively, given by the inverse of the FIM. The FIM and its inverse are both shown in equation 5.16. To see the dependence of the variance on the gradient more clearly, the second term of the determinant is sometimes neglected [34], as shown in equation 5.17. The code that calculates the gradients I_x and I_y and subsequent calculation to obtain the CRLB is found in Appendix A.4. Typical gradient squared images I_x^2 and I_y^2 that result from (a part of) this code are shown in Figure 5.13. As can be seen from both these images, the assumption that the second term in the determinant can be neglected is fair. Regions, where I_x has a high value, have a low value for I_y and vice versa, so their multiplication gives a far lower value than I_x^2 or I_y^2. Obtaining the noise σ of the system is described in the next section.

$$
\begin{aligned}
var(v_x) \geq F_{11}^{-1} \qquad & var(v_y) \geq F_{22}^{-1} \\
\geq \frac{\sum_S I_y^2}{\sigma^2 \det(F)} \qquad & \geq \frac{\sum_S I_x^2}{\sigma^2 \det(F)} \\
var(v_x) \geq \frac{\sigma^2}{\sum_S I_x^2} \qquad & var(v_y) \geq \frac{\sigma^2}{\sum_S I_y^2}
\end{aligned}
\tag{5.17}
$$

Considering equation 5.17, the CRLB provides two ways by which the Rasdif performance can be improved. Firstly, a full use of the range of

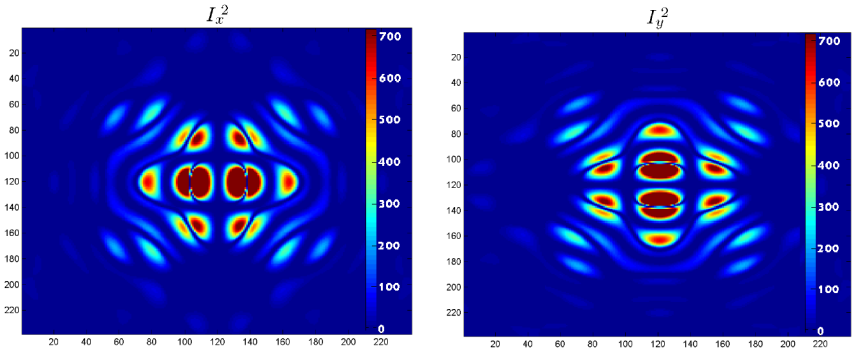

(a) (b)

Figure 5.13: (a) Gradient squared in the x direction and (b) gradient squared in the y direction of a typical Rasdif image

the intensity increases the signal-to-noise ratio in the image. An 8-bit image, for example, should have value *0* at the *black areas* and value *255* at the white blobs. This can, to some extent, be achieved by attuning the light source and the lighting settings of the image sensor. Secondly, the design and size of the diffraction plate can increase the amount of gradient energy in the diffraction pattern. The number of fringes present in the image and the contrast between these fringes can be altered by changing this design or the size.

5.4.1 Random noise determination

Random noise determination of the used light source—pixel image sensor combination is necessary for determining the CRLB of the system, as shown in equation 5.17. The set-up for determining this noise is best described as the Rasnik light source without the mask incident on the pixel image sensor. The light source is only centimetres apart from the pixel image sensor to eliminate the contributions by systematic errors as much as possible. As the PIKE F100Bs of the 140m set-up were not available at Nikhef when these measurements were done, only the pixel image sensor of the 4 m set-up, the Logitech C300, was investigated. To compare the results obtained with these measurements, the Videology 24B1.3XUSB-C (a high quality pixel image sensor also used in the 4 m set-up) and the Logitech C5000 Pro (a pixel image sensor used in prior Rasniks) were also investigated using the method described below. A single measurement with the DPSS laser beam incident on the C300 pixel image sensor is done for comparison of the noise levels when using a Rasdif light source.

A number of pictures (N>1000) are shot in PNG format and the value of 8 positions (i.e. pixels) of all these pictures are put in 8 different vectors. This operation is done by the Matlab code, which is found in

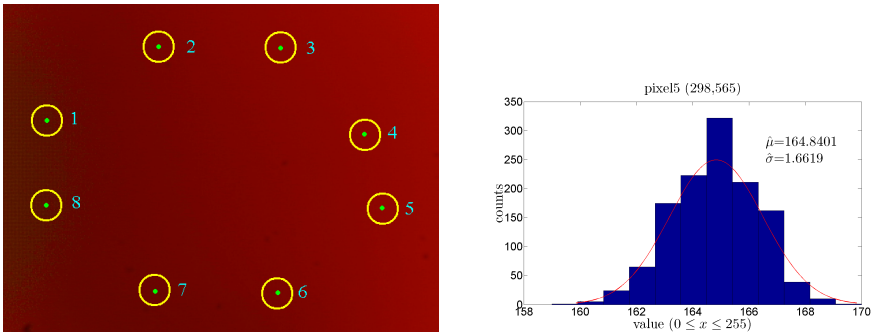

(a) (b)

Figure 5.14: (a) Location of the pixels used for random noise determination and (b) a typical Gaussian fit over a pixel vector

Appendix A.3, and these vectors are plotted and a Gaussian fit would give the σ. The location of the pixels and a typical Gaussian fit over a *pixel vector* are both shown in Figure 5.14. Both noises, the pixel noise and the noise in the light source, and thus their sum as well, are assumed to be Gaussian here. The pixel correlation between all pixels and a value versus time plot of a pixel can be examined to determine if light source intensity variations or other artefacts were in the data. If this is the case, the measurement is discarded. The σ obtained after analysis of the pixel values is a measure for both the pixel noise as the noise of the light source as there is no way to keep these apart in a read-out of an image sensor.

For both red and green light the pixel image sensor Logitech C300, which is to be used in future Rasnik implementations at the CLiC mock-ups, is investigated. Both colours are investigated because of the Bayer pattern on pixel image sensors. This pattern, used in almost all colour pixel image sensors, intrinsically uses more surface of the pixel to detect green light than it uses to detect red light. This could have an effect on the noise, as an *integral* over a bigger surface should result in less noise. Measurements like these are done to characterise the pixel image sensor. As the C300 pixel image sensors are obtained by opening a homonymous commercial USB webcam, so no complete characterisation of the specifications are supplied. The voltage supplied to the light source is varied to obtain different light intensities per measurement. The results of both sets of measurements are shown in Figure 5.15. No clear difference between the noise response of the C300 when using different colours is detectable.

The results of measurements done on the C5000 and the Videology pixel image sensors are shown in Figure 5.16. Comparing Figure 5.16(a) and Figure 5.16(b) a clear difference between the CMOS pixel image sensor out of a webcam (C5000) and an industrial CMOS pixel image sensor (Videology) is visible. The total random noise levels of the Videology are lower than those of the C5000 over the entire intensity (μ) range.

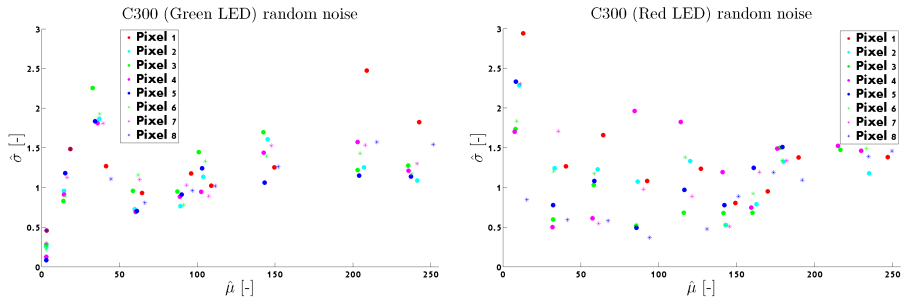

(a) (b)

Figure 5.15: μ versus σ plots of the Logitech C300 for (a) green light and (b) red light

The total random noise going down a considerable margin when using a pixel image sensor of better quality might be an indication that the total random noise is dominated by the pixel noise. In other words, the noise contribution in the light source is smaller than the contribution of the pixel noise. To a small extent, larger random noise levels are visible at low intensity for the C5000. This is not investigated more as the C5000 results were for comparison only and the C300 would be the used pixel image sensor in the 4 m set-up and CLiC mock-up.

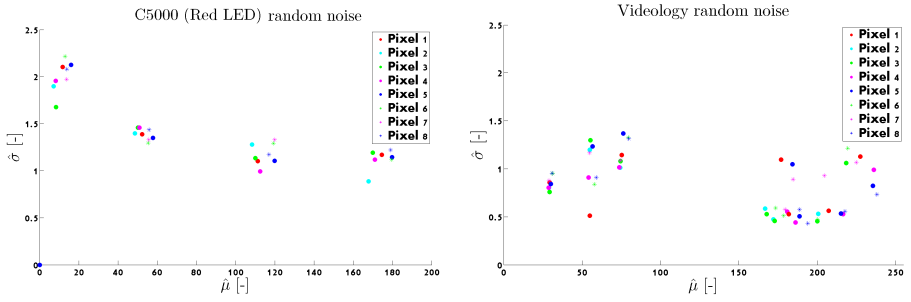

(a) (b)

Figure 5.16: μ versus σ plots of (a) the Logitech C5000 pro and (b) the Videology 24B1.3XUSB-C

The measurements of Figure 5.15 and Figure 5.16 are taken at zero gain and maximum shutter time. These are the settings generally known for introducing the least noise. Gain is electronic enhancement of the output values of the pixels, which introduces (more) electronic noise. A longer shutter time results in a longer integration time to establish an output and this levels out noises that have a time over which they vary smaller than the shutter time. To explore the noise dependence on the gain setting, random noise measurements with varying gain—fixed maximum shutter time are done. The results are shown for red and green light in Figure 5.17. Figure 5.17(a) and Figure 5.17(b) show similar behaviour

when changing the gain setting. It matches the expected behaviour as more applied gain increases the noise level. In both sets of measurements the second gain setting (25 percent gain) results in the lowest noise. As the levels of $\overline{\hat{\mu}}$ are almost the same, something else than electric amplification of the signal is occurring. As discussed above, the C300 pixel image sensor specifications are unknown and this ill understood *black box behaviour* is to be taken into account.

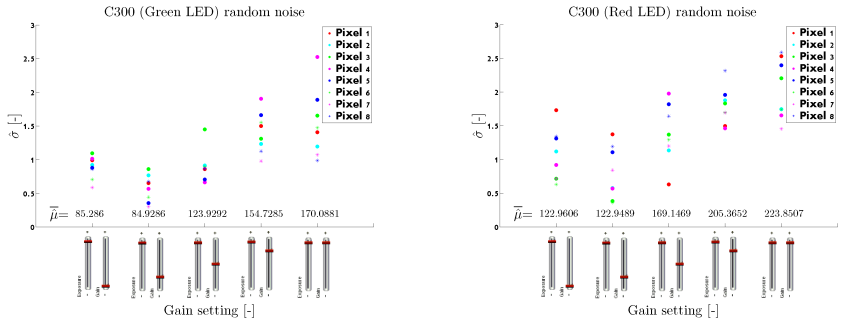

(a) (b)

Figure 5.17: Gain versus σ plots of the Logitech C300 for (a) green light and (b) red light

The fact that longer shutter times should result in less noise is also shown in equations 5.11, 5.12 and 5.13, where an increase in Δt decreases the noise. Sets of measurements where the shutter time is varied show no clear noise dependence on shutter time, as is shown in Figure 5.18(a). This may be an indication that the time scales of the random noises are larger than the shutter time window over which the C300 can variate. One pixel read-out of single measurement using a DPSS laser in stead of the Rasnik light source is shown in Figure 5.18(b). A comparison of this result to the results of the Rasnik light source results, shows the noise levels are comparable.

5.4.2 Analysis results

Now that the random noise is *known*, the obtained value for σ can be plugged in equation 5.17. Considering the results shown in the previous section, a value of $\sigma = 2$ (with respect to 8-bit read-out of the image sensors) is adopted for the calculation of the CRLB. As the variance in the shift estimation must be dependent on the size of the pixels that are used to register the image, the pixel size must somehow appear in equation 5.17. This equation is used in the Matlab script that calculates the CRLB, which is found in Appendix A.4. In this code, the dx and dy used to calculated the gradients I_x and I_y are, in fact, equal to the pixel size. The C300 pixel image sensor has square pixels with dimension 11.2 μm and thus the pixels have the same dimension (d_{pix}) in x and y. They

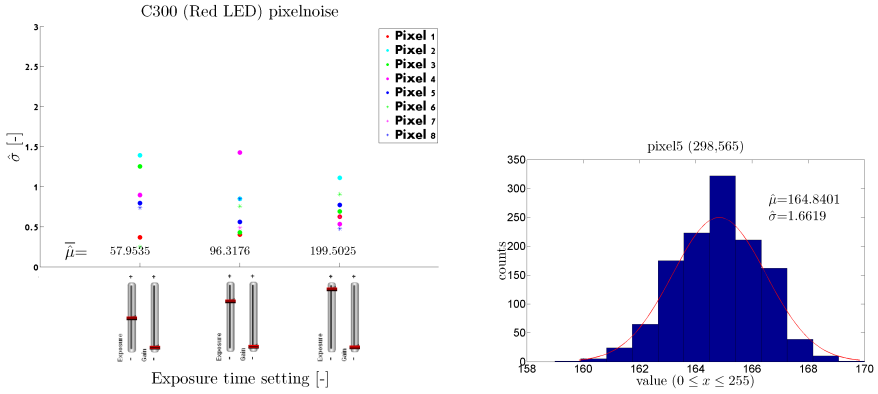

(a) (b)

Figure 5.18: (a) Example of an exposure time versus σ measurement of the Logitech C300 and (b) a single pixel read-out of single measurement using a DPSS laser

can be taken outside the sum in the denominator of equation 5.17:

$$var(v_x) \geq \frac{\sigma^2}{\frac{1}{d_{pix}^2}\sum_S I_x^2} \qquad var(v_y) \geq \frac{\sigma^2}{\frac{1}{d_{pix}^2}\sum_S I_y^2}$$

$$var(v_x) \geq \frac{d_{pix}^2\sigma^2}{\sum_S I_x^2} \qquad var(v_y) \geq \frac{d_{pix}^2\sigma^2}{\sum_S I_y^2} \tag{5.18}$$

The variance is the standard deviation (σ) squared so the standard deviations are equal to $\sigma_{CRLB,x} = \sqrt{var(v_x)}$ and $\sigma_{CRLB,y} = \sqrt{var(v_y)}$. The values for σ_{CRLB} give the CRLB using simulated, noiseless images and taking into account the random noise. It is the resolution that *can* be obtained by a lossless image analysis algorithm without any of the systematic errors described in §5.1.

Simulated Rasdif images are made using software made by B. Bouwens. The simulation is done for a 4 m Rasdif system with a point source laser emitting spherical waves of light at 532 nm. The size of the diffraction plate, with the design as shown in Figure 3.5(c), is scaled to vary its dimensions. The scale is varied from 0.5 to 5 in steps of 0.02, with 5 as the upper limit because at that point the outer radius of the diffraction plate is 7.2 mm. This is nearing the lens size needed for a 4 m Rasnik and having a diffraction plate with smaller dimensions than the lens was the initial drive for Rasdif.

Figure 5.19 shows the results for Fresnel diffraction of several scaled diffraction plate designs. The diffraction patterns become smaller and more fringes appear with larger diffraction plate design, as predicted by

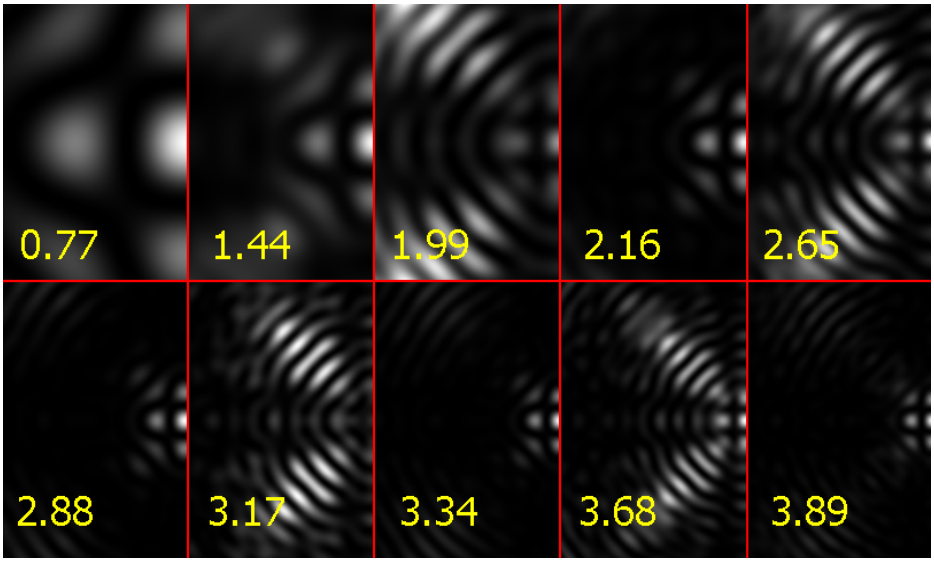

Figure 5.19: Simulated Rasdif images varying for a 4m system, varying the scale of the diffraction plate design. As the images are symmetric, only half of each image is shown. The values in each image indicate the outer radius of the design in mm

diffraction theory. A resonating behaviour in the intensity of the fringes of the *legs* can also be distinguished from the 1.99 mm diffraction pattern onwards. Considering these images, the amount of gradient energy in the diffraction pattern does not seem to vary linearly with the diffraction plate design dimensions. The gradients in the image are needed for the CRLB calculation performed by the Matlab routine of Appendix A.4

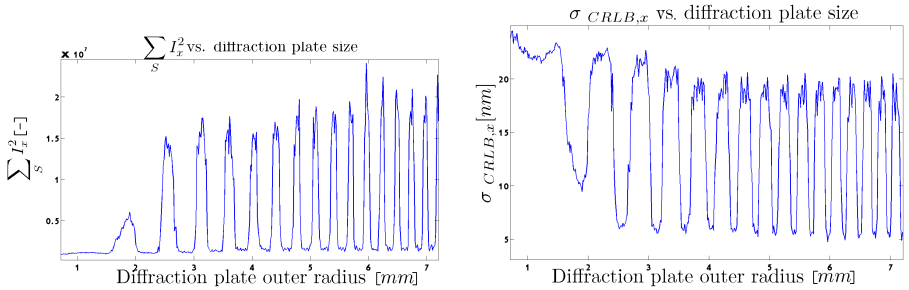

(a) (b)

Figure 5.20: (a) X gradient squared summed over the entire image and (b) the CRLB in the x-direction calculated for the simulated Rasdif images

The resonating behaviour, be it with a superimposed fluctuation, is clearly visible in Figure 5.20(a). This fluctuation is due to the fact that with finer and finer diffraction pattern more and more fringes *enter* the image. The amount of gradient energy of the present diffraction plate

in the 4 m Rasdif (outer radius of 1.44 mm) is more than an order of magnitude smaller than, for example, the gradient energy in a diffraction pattern by a diffraction plate with an outer radius of 2.6 mm or 3.1 mm. Considering equation 5.18, the higher gradient results in a lower CRLB, as is shown in Figure 5.20(b). The gradient and the CRLB in the y-direction are the same as in the x-direction, because the images are symmetric.

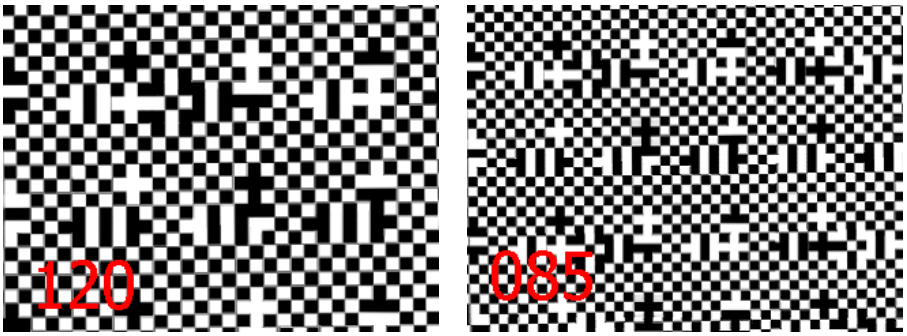

(a) (b)

Figure 5.21: Noiseless Rasnik images (a) with a chess field size of 120 μm and (b) with a chess field size of 85 μm

The projected Rasnik images intrinsically hold more gradient energy than Rasdif images. In Rasnik images, shown in Figure 5.21, the full area of the image sensor is filled with black-to-white transitions, i.e. gradients. Rasdif images have *dark areas* and the *best* images typically have an order of magnitude less gradient energy than a Rasnik image. This results in a Rasnik image with chess field size of 120 μm, shown in Figure 5.21(a), having a σ_{CRLB} of 0.96 nm. A Rasnik image with chess field size of 85 μm, shown in Figure 5.21(b), has a σ_{CRLB} of 0.75 nm.

Chapter 6

Operational tests and precision improvement

Particular (thermal) conditions are key for obtaining a more correct response (§5.1.1) and better resolution (§5.1.2) of optical alignment systems. Under varying thermal conditions the subsequent varying refractive bending might shift the image and thermally induced jitter decreases the resolution. In §5.3 a summary of an extensive finite element analysis performed by R. Rosing (Nikhef) is presented. Theoretical predictions on int. al. the refractive bending of light are implemented in the analysis to design thermal shielding in such a way that the alignment systems meet the CLiC requirements. Application of the results of the analysis to the thermal shielding of the 4 m set-up is described and discussed in this chapter. If the optical path is in perfect vacuum, *all* thermal gradients and thermally induced jitter vanish of course. Evacuating the optical path of the 140 m set-up to a certain pressure will reduce the effect of the thermal gradient (see equation 5.5). In fact, at some pressure the mean free path becomes equal to the vacuum tube diameter and no thermal gradient can exist at all. The thermal induced jitter also reduces as there are simply less air molecules in the optical path to refract on. A resolution comparison to the WPS at a pressure of 1.5×10^{-4} mbar is presented in this chapter.

Applying known translations to different set-ups can show if the system gives the expected output. If this is not the case, the element of the system that causes these deviations needs to be altered or replaced. The *virtual point of departure* issue, regarding the laser of a Rasdif system, encountered in §5.1.4 is an example of this procedure. This virtual point is not at all specified when one orders a laser, so different lasers were tried and the same tests were performed. After sufficient testing, the green DPSS laser came out as best. Present response to both the 4 m set-up, where translations were applied at the light sources, as well as the 140 m set-up, where the diffraction plate (holder) was subject to the applied translations, are described below.

N. B. TT1 laser breakdown in vacuum operation

After installing the DPSS lasers at the TT1 set-up at November 28, 2011, the vacuum tube was evacuated to a pressure of 1.5×10^{-4} mbar. This meant air cooling of the laser was reduced greatly and *all* the heat transfer had to be done via the structure around the laser. The design of the laser mount is shown in Figure 6.1. The heat from the laser could only transfer outside the vacuum via the circular plate and the three threads. These three threads run down to the part of the mount that is in contact with large plates of the steal and the *outside world*. The stainless steal structure around the laser is thought to have insufficient heat transfer capacities to remove the part of the 1 W of electrical energy that is not converted into light.This has proven to be an inadequate way of getting rid of the dissipative heat generated by the lasers.

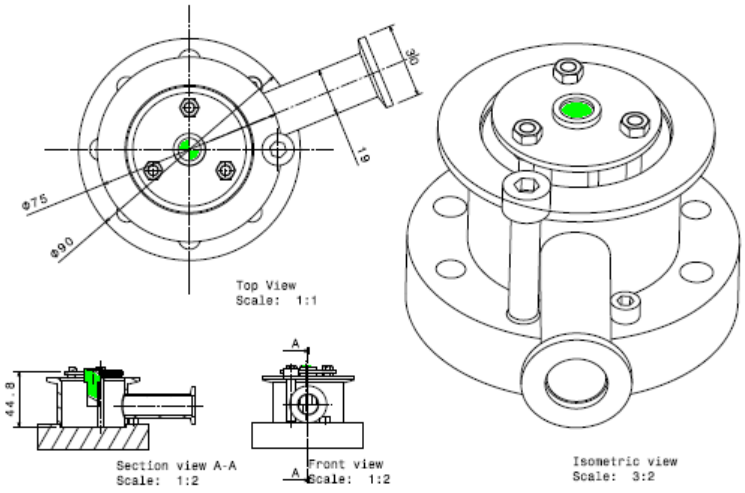

Figure 6.1: Technical drawing of the laser-mount (courtesy of R. Rosing)

When opening the vacuum at February 8, 2012, the bottom laser only seemed to emit red light, which meant that the pumping and frequency doubling mechanism did not work any more. This is believed to have been caused by overheating of the laser, which altered it's monochromatic emission characteristics. The diode's light not being fully monochromatic any more, diminished the DPSS operation and thus the operation of the bottom Rasdif. On February 8, 2012, both lasers were removed from the 140 m set-up and returned to Nikhef. New design studies on the laser mount have to be done in order to solve this problem. On February 7 and 8, 2012, measurements with the upper Rasdif were performed, comparing it to the WPS. The results of this measurement, with only one of the two Rasdifs working, are presented below.

6.1 Mechanical behaviour

To test the response of both set-ups to applied transitions, one of the element(holder)s of both the 4 m and the 140 m set-up are translated in a direction perpendicular to the optical path. For the 4 m set-up, the translation is applied at the light sources to the (horizontal) x direction by means of the linear actuator, shown in Figure 4.1(b). The way the 140 m set-up is tested is more crude and is shown in Figure 6.2. Both the diffraction plate holder of the RasCLiC and the two WPS systems are placed on a so called *plaque*. A weight, which is simply a tank filled with water, pulls on the plaque via a pulley.

Figure 6.2: Translation applied to the plaque the diffraction plate is on by means of a pulley and a weight (tank filled with water). Two WPS systems (W2D-7D7-006 and W2D-7D7-007) are positioned on the same plaque

6.1.1 4 m set-up response to applied translations

The applied translations to the light sources are done by the electrical linear actuator: The Newport Newstep. First calibrating the Rasdif images to be the centre of the image sensor, the linear actuator applies a translation in steps of 214.3 μm (one seventh of 1.5 mm) to the lights sources' mount. Four translational steps are applied to one side in the x direction, seven to the opposite side and three in the initial direction to return to the x position where the measurement started. The results are shown in Figure 6.3(a). As the mount's translations in the x direction are *never* precisely aligned with the x direction defined by the Rasnik mask or Rasdif image sensor, a small translation readout in the y direction is

visible.

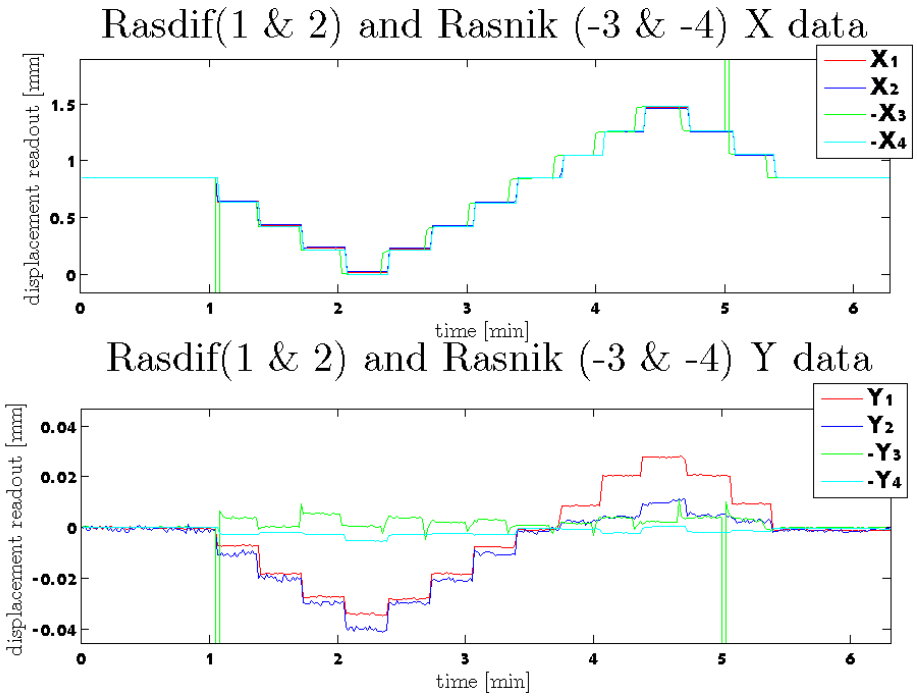

(a)

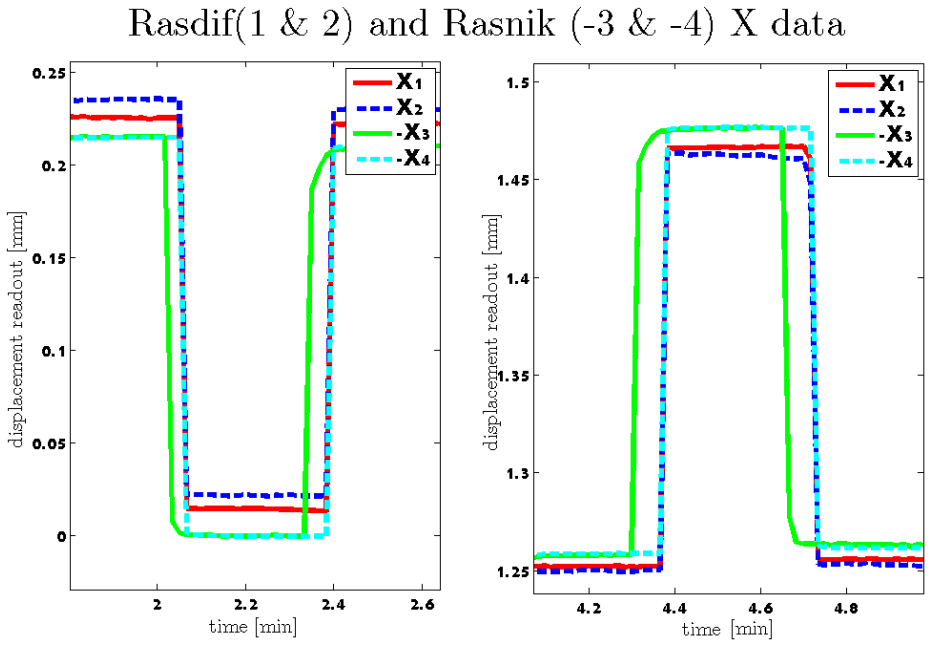

(b)

Figure 6.3: (a) 4 m set-up response to applied translations over a range of 1.5 mm with steps of 214.3 μm and (b) a zoom-in at the extreme values for slope determination

There are large peaks in the Rasnik 3 readout (at 1 and 5 minutes) because the image, which is taken for position determination there, was precisely taken during the translation. A smeared out image was taken by the image sensor and the position estimation software failed to reconstruct the position. Visible in Figure 6.3(b), the Rasnik and Rasdif readouts do not match exactly. The Rasdif slope is smaller than the Rasnik position estimation in both extremes. As described in §5.1.4, this is because of the VPoD of the Rasdif lying behind the laser, giving these Rasdifs a smaller slope than the Rasniks. The Rasdif slope with respect to the Rasnik readout is about 0.98.

6.1.2 Diffraction plate translation in the 140 m set-up

Two different translational measurements have been done at the 140 m set-up: one on February 7, 2012, at around 18 h and one on February 8, 2012, around 9 h. The weight is manually hanged on and off the plaque via the pulley. The results of both tests are shown in Figure 6.4, with the WPS data plotted as well for comparison. As discussed in §3.2.1, the expected readout of RasCLiC is twice that of the WPS. The difference between the two measurements is that the first one is started with the weight on and the second on started with the weight off. This is visible in the different apparent directions of the translations. The 0.5 Hz wobble in the RasCLiC readout is because the tank of water was not hanging perfectly still and is thus only visible in both measurements during a period where the weight is on. As is the case for the 4 m translational measurements, a readout in the y direction is visible. The same reason as explained above applies, but also the crude way of applying the translations bends the structure supporting the plaque not only in the x direction, but also in the y direction.

In both measurements, the WPSs give a x direction readout of about 70 μm to the translation as a result from applying the weight. For the February 7 measurement, the RasCLiC gives a readout of 125 μm, whereas a 60 μm readout is apparent in the February 8 measurement. Images written during the measurement also showed this different shift in images at a *weight on* and *weight off* instant, excluding a software readout error. The physical reason for this anomaly is ill understood. A possible explanation of this large error is the presence of bubbles of air in the vacuum tube that work as a lens. These bubbles might swerve through the vacuum tube explaining the different lensing from day to day.

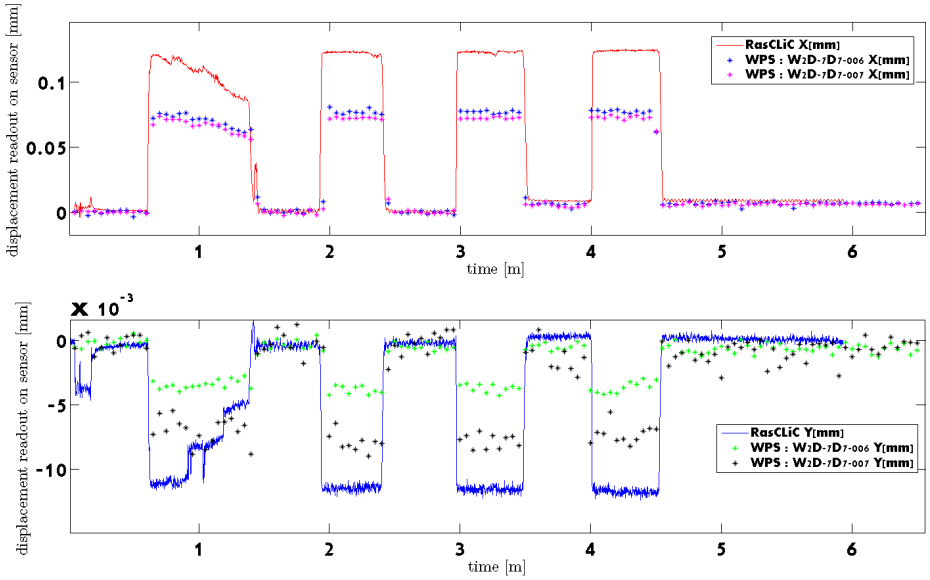

(a)

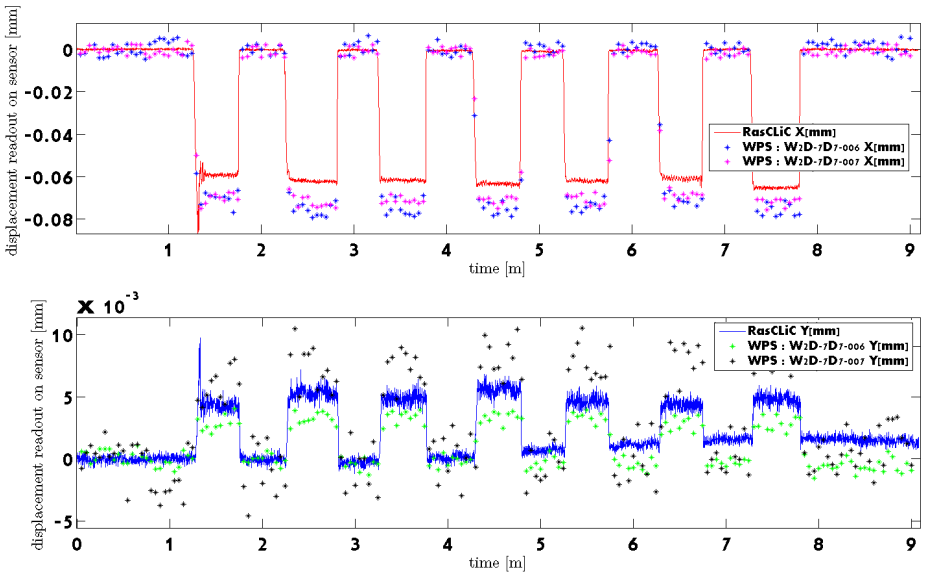

(b)

Figure 6.4: 140 m set-up response to applied translations by pulling the *plaque* at (a) February 7, 2012, around 18 h and (b) February 8, 2012, around 9 h

6.2 Thermal behaviour

The resolution of both set-ups are measured by running the software read-out in a static operation. No translations are applied and all matters that could effect the thermal conditions, e.g. cooling devices or lab lightings,

are switched off.

6.2.1 4 m thermal operation in open air

As discussed in §5.1.2, the flows of air result in a wobbling of the image that is presented to the image sensor. Without any thermal shielding, the resolution measurements of the parallel Rasdifs and Rasniks are shown in Figure 6.5. The thermally induced jitter, together with the random noises, result in an rms resolution of 5-10 μm for all four alignment systems.

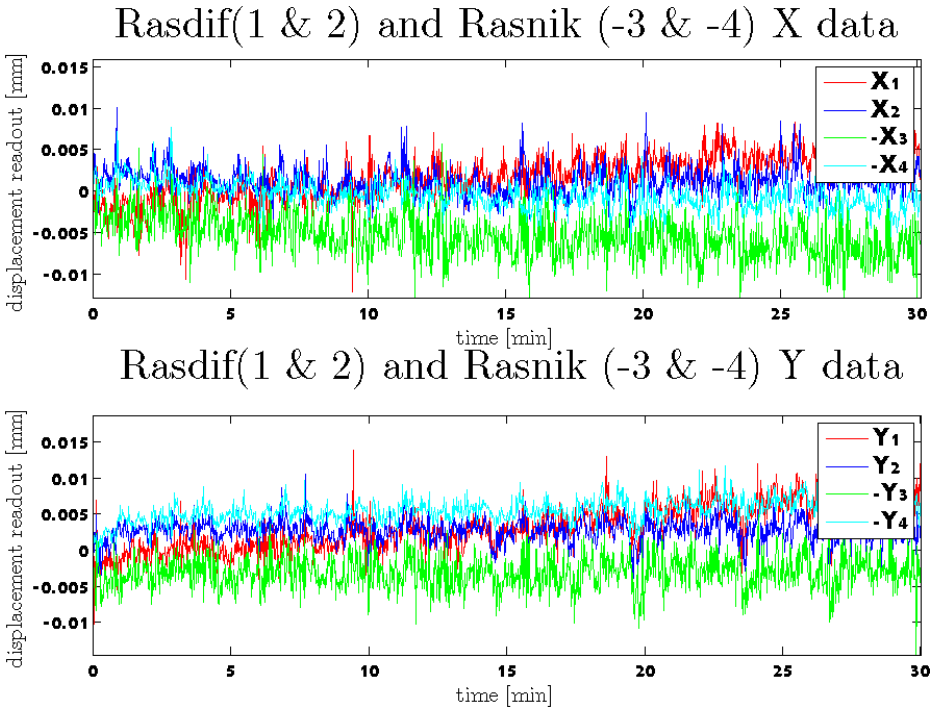

Figure 6.5: 30 min. resolution measurement at the 4 m parallel Rasdif/ Rasnik set-up. No thermal shielding is applied here

The thermally induced jitter is not easily modelled. The systematic bending of light is calculated for gradients that will exist in an infinitely long thermally shielded duct in §5.1.1 and §5.3. The ducts that are used in the 4 m set-up and that are to be used in the CLiC alignment mock-up are not infinitely long and open on both sides. Longitudinal flows of air can still pass through these ducts and the precise thermal gradient present, for example, in the lab at Nikhef is unknown.

Applying all of the above in a single model is a cumbersome job — if not impossible — and an empirical approach is adopted to determine if the thermal shielding solution is ample for reducing the jitter to sub-micron levels. Simulating the ducts to be used in the CLiC mock-up, shown in Figure 5.12, in the 4 m set-up was done by folding rockwool from a DIY

store (Praxis) around aluminium ducts and placing these ducts in the 2 m voids between the three Rasdif/ Rasnik element holders.

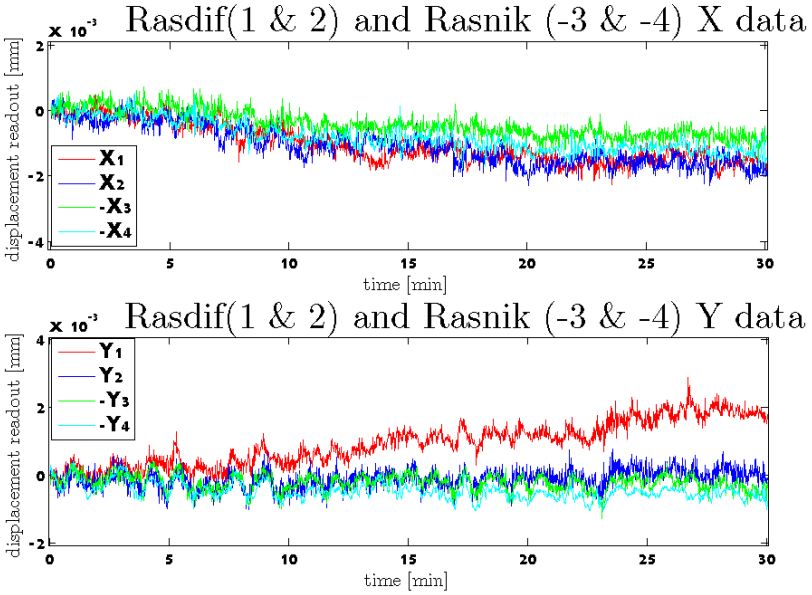

Figure 6.6: 30 min. resolution measurement at the 4 m parallel Rasdif/ Rasnik set-up. A thermal shielding of aluminium and rockwool is applied here

Applying this thermal shielding to the 4 m set-up gives better resolution for Rasdif and Rasnik. The Rasdif and Rasnik rms resolution is reduced by a factor 10 to 0.5-1 μm, as is shown in Figure 6.6. The drift in the x direction of about 1-1.5 μm is picked up by all four systems. This can be a contraction or expansion of the supporting structure of one of the element holders. Rasdif 1 shows a drift in by y direction of about 2 μm. This is believed to be attributed to the thermal expansion of the laser structure itself. The heat, due to dissipation of electrical energy, heats up the material around the laser and this expands in a non-symmetric way.

6.2.2 140 m thermal operation in a vacuum

The results of an overnight measurement of the RasCLiC set-up in a 1.5 $\times 10^{-4}$ mbar vacuum is shown in Figure 6.7. For comparison, the readout of the two WPS sensors, which are on the same location as the diffraction plate, are also plotted. The rms resolution of the RasCLiC is about 1.5-2 μm in the x and y direction. Two WPSs show different performance in the x and y direction and compared to each other. The W2D-7D7-007 has a 6 μm rms resolution in both directions, but the W2D-7D7-006 has a different resolution for both directions. The rms x resolution of the W2D-7D7-006 is about 12 μm, whereas the rms y resolution of this WPS

is about 3 μm.

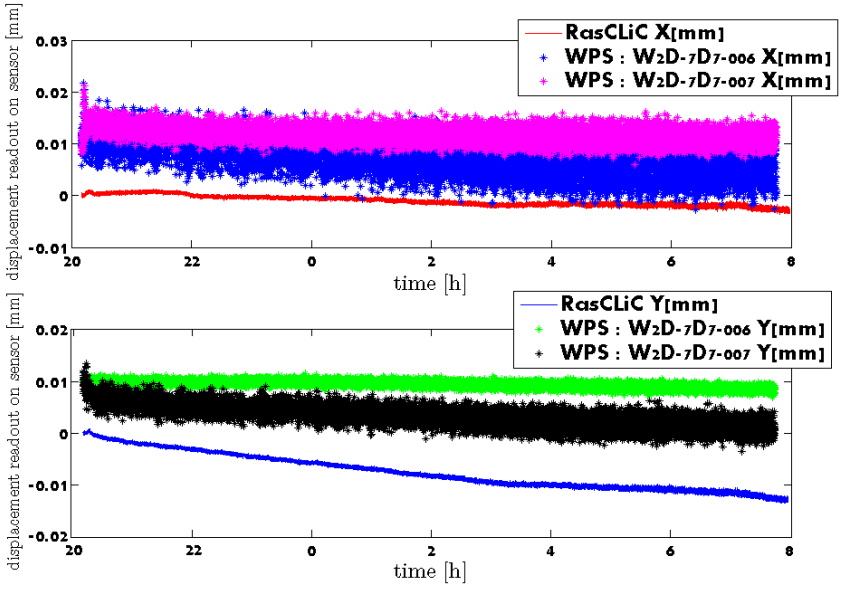

Figure 6.7: 12 hour resolution measurement of 140 m RasCLiC set-up and the WPS on the night of February 7 and 8 2012. The RasCLiC is in a vacuum of 1.5 $\times 10^{-4}$ mbar

The drift in the x and y direction, picked up by all three systems, can be due to a temperature decrease over night in the tunnel. These may contract the supporting structures of the systems. Different magnitudes of the drifts are then due to the different (materials used in) the supporting structures of the different systems.

Chapter 7

Implementations at CERN

The ultimate goal of this thesis is comparison of Nikhef's optical alignment systems to other proposed systems for the CLiC pre-alignment. Will optical alignment complement existing alignment systems or will it be unable to come close to the performance of the other likely candidates? Or will it even surpass the performance of these other candidates? These are questions that are only going to be answered if all alignment systems read out side by side on a mock-up of the CLiC design, i.e. all the main beam and drive beam components.

A design of a 2 m section of the CLiC design is shown in Figure 7.1. At the beginning and end of each of these sections, a position sensor is to be installed for the intermediate alignment. Between the main beam and the drive beam alignment will be present as well by a proximity system (60 mm Rasnik), as described in chapter 3. A mock-up of two of these 2 m sections has been built at CERN to test the performance of several alignment systems for these distances. For the 200 m pre-alignment the present *mock-up* is the TT1 set-up.

Having both the electron and the positron beam aligned individually is not enough though. The *very* high speed particles will have to collide and in Table 3.1 the alignment requirements for the final focus show to be even more strict than the 2 m requirements (linac). This is because the two beams that have to collide have an area of only 42 nm^2. The beams are focused to this small area by so called *QD0 magnets*, which are quadrupole magnets. Space at interaction point is *expensive* as it is primarily reserved for detectors. Even if *alignment* is given some space, the alignment system probably has to be small and precise, not to mention radiation hard. For these and for redundancy reasons a smart solution has been devised to get the position information of both ends of the beam radially outside of the interaction point environment. By doing so, these outward points can be aligned and this data can be translated to information about the alignment of the two QD0 magnets. This system is called the QD0 spoke system.

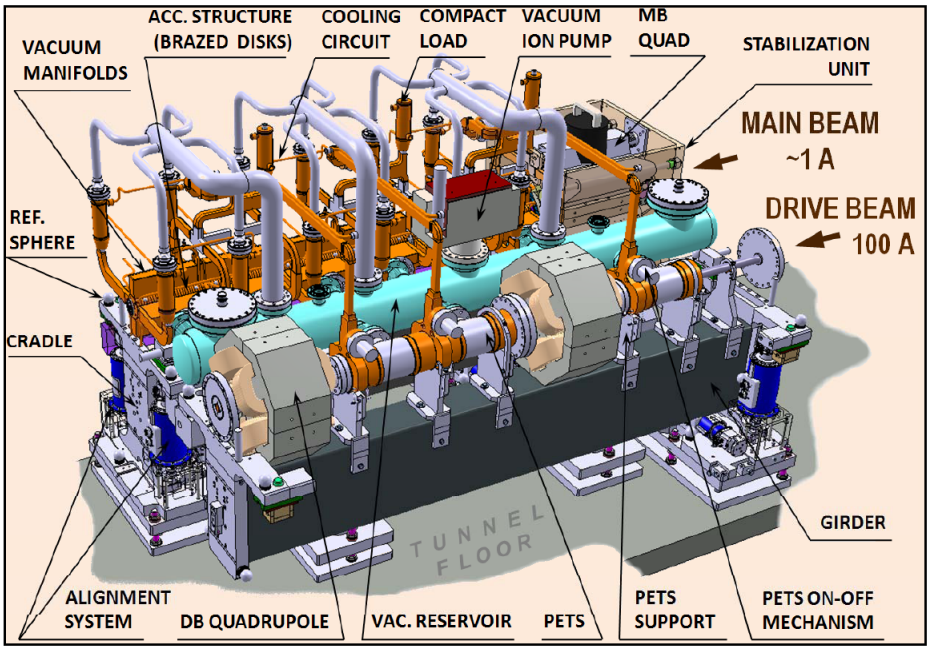

Figure 7.1: The CLiC alignment mock-up; 2 m section which is repeated along the entire CLiC design, from [35]

7.1 2 m CliC alignment mock-up

To test and compare all alignment systems that could be installed in the small and intermediate CLiC alignment distances. Alignment between the drive beam and the main beam is to be done by small alignment systems. Nikhef proposes Rasnik for this purpose as there is much experience with Rasnik in this field. The alignment of the components of the two beams is to be done by alignment systems that have a sensor at every 2 meters. This is because the 2 m section, which is shown in Figure 7.1, is repeated along the entire CLiC design. The capability to align these sections with 4 m systems is proven by the 4 m set-up at Nikhef. If an image moves on the image sensor read-out, it is not certain which of the three points of both alignment systems is moving. To determine this and to comply to the demand that a sensor should be present every 2 m, a leap-frog method is applied, as shown in Figure 7.2.

7.1.1 Mock-up description

A mock-up of a 2 units of 2 m section of the CLiC design is in Building 169 (169/S-039) at CERN, of which a photograph is shown in Figure 7.3. The main beam supports are in *red* and on the *yellow* supports drive beam components have to be installed. The apparatus packed with springs and the blue cylinder, both in *white*, are piezoelectric actuators to apply knows

Figure 7.2: Schematic overview of the leap-frog method with 3 Rasnik/ Rasdif elements at each point. Every light source—lens/ diffraction plate—image sensor trio is now (indirectly) a position sensor of that particular point

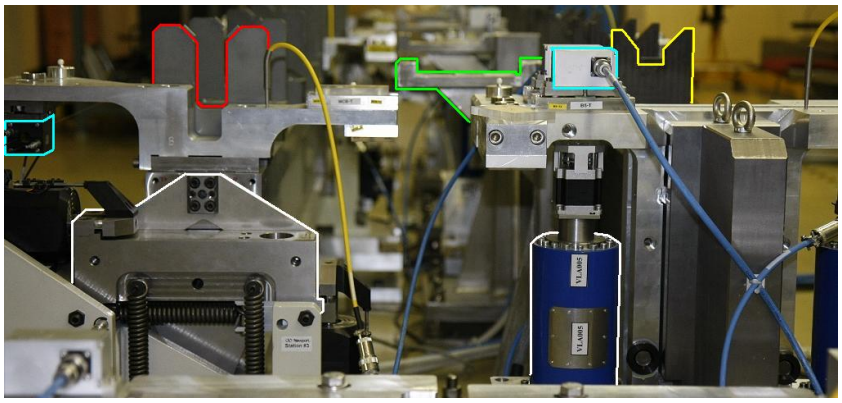

Figure 7.3: The CLiC alignment mock-up (courtesy of J. Koopstra)

translations to the mock-up and, ultimately, to realign the beams on the basis of the output of the alignment systems. The *green* supports in the middle are there for the vacuum structure. Both in turquoise, a Wire Positioning System (WPS) and a Tilt Meter System (TMS) are visible. Figure 7.3 shows the state of the mock-up in the summer of 2011. At that point many more elements needed to be installed, in particular whole beam and vacuum structure on top. The top structure of int. al. vacuum tubing, focussing magnets and PETSs is shown in Figure 7.1. Sections of 2 m are still to be installed on both sides of the present 4 m mock-up in the future.

7.1.2 RasChain

In Figure 7.2, the system to be installed in the 2 m CLiC alignment mock-up is globally explained. This solution is called RasChain for obvious reasons: a chain of Rasniks and Rasdifs is to be installed on the mock-up. Each beam will be fitted with so-called ChainPlates every 2 m, so that the leap-frog method can be applied. Both 4 m Rasnik and 4 m Rasdif will work side by side for redundancy and comparison reasons. Each ChainPlate is fitted with a DPSS laser, a Rasnik light source, a 1 m focal length lens, a diffraction plate and one image pixel sensor, as is shown in Figure 7.4.

A Rasnik and Rasdif monitoring the same 4 m of beam alignment

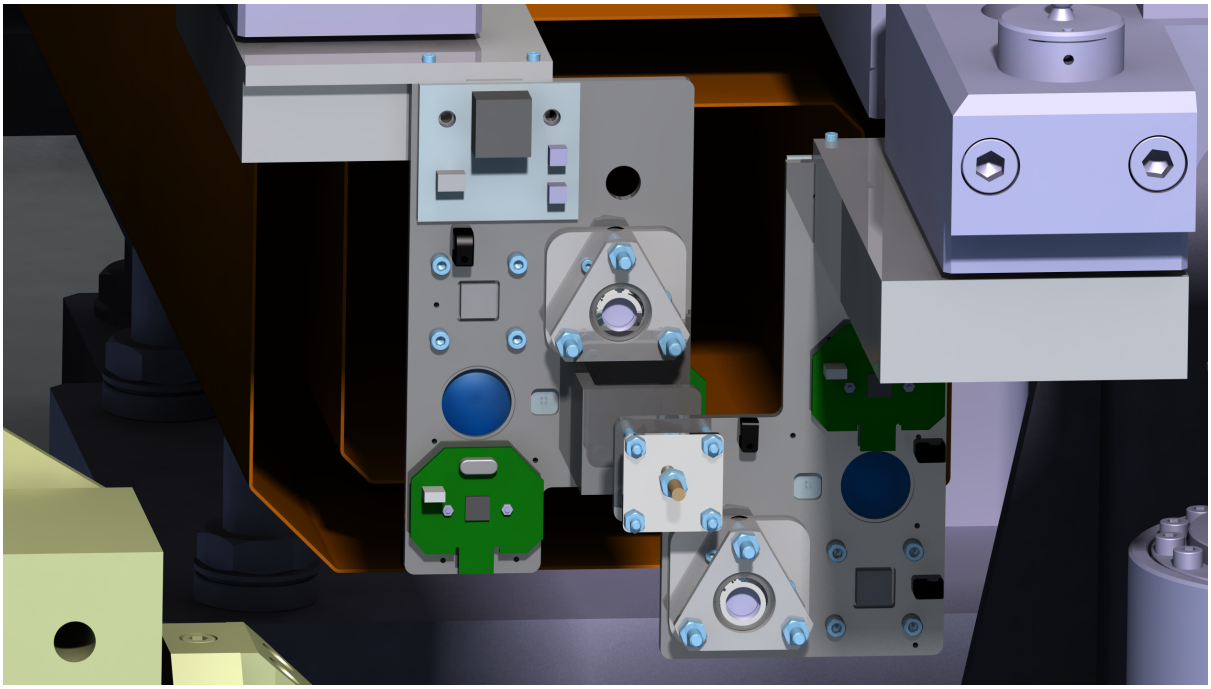

Figure 7.4: CATIA drawing of the ChainPlate designs. Both the drive beam and main beam ChainPlate and the proximity Rasnik monitoring inter-beam alignment are shown. The void between the aluminium ducts of thermal shielding, in *orange*, is to be filled with polyurethane (courtesy of A. Alaei)

will not read out simultaneously as they will share an image pixel sensor. They will be controlled by a *switchbox*, designed by H. Groenstege. A computer controlling this switchbox will apply the correct software to the images, as Rasnik and Rasdif images come and go on the image pixel sensor. A 60 mm Rasnik system, with the camera (image sensor and lens combination) attached to one plate and the light source with the mask to the other, monitors the inter-beam alignment.

Hexagonal thermal shielding ducts, little under 2 m of length shown in Figure 7.5, will be positioned between the ChainPlates, ensuring a small gradient and decreasing other thermal effects in the optical path on all the Rasnik and Rasdif light *travelling* that particular section. Around the unshielded part near the ChainPlates flexible sheets of isolation material will be folded. This is to be solved *in situ*, as the design of this is both cumbersome and superfluous.

All ChainPlates and the components that are on there are designed to be a distance of 2010 mm apart, which is a dimension of the CLiC mock-up. The points at which the Nikhef will *hang* the ChainPlates are spaced this amount. If this dimension of 2010 mm changes Rasnik and Rasdif elements will have to be altered. In Rasnik, as shown in Figure 5.6,

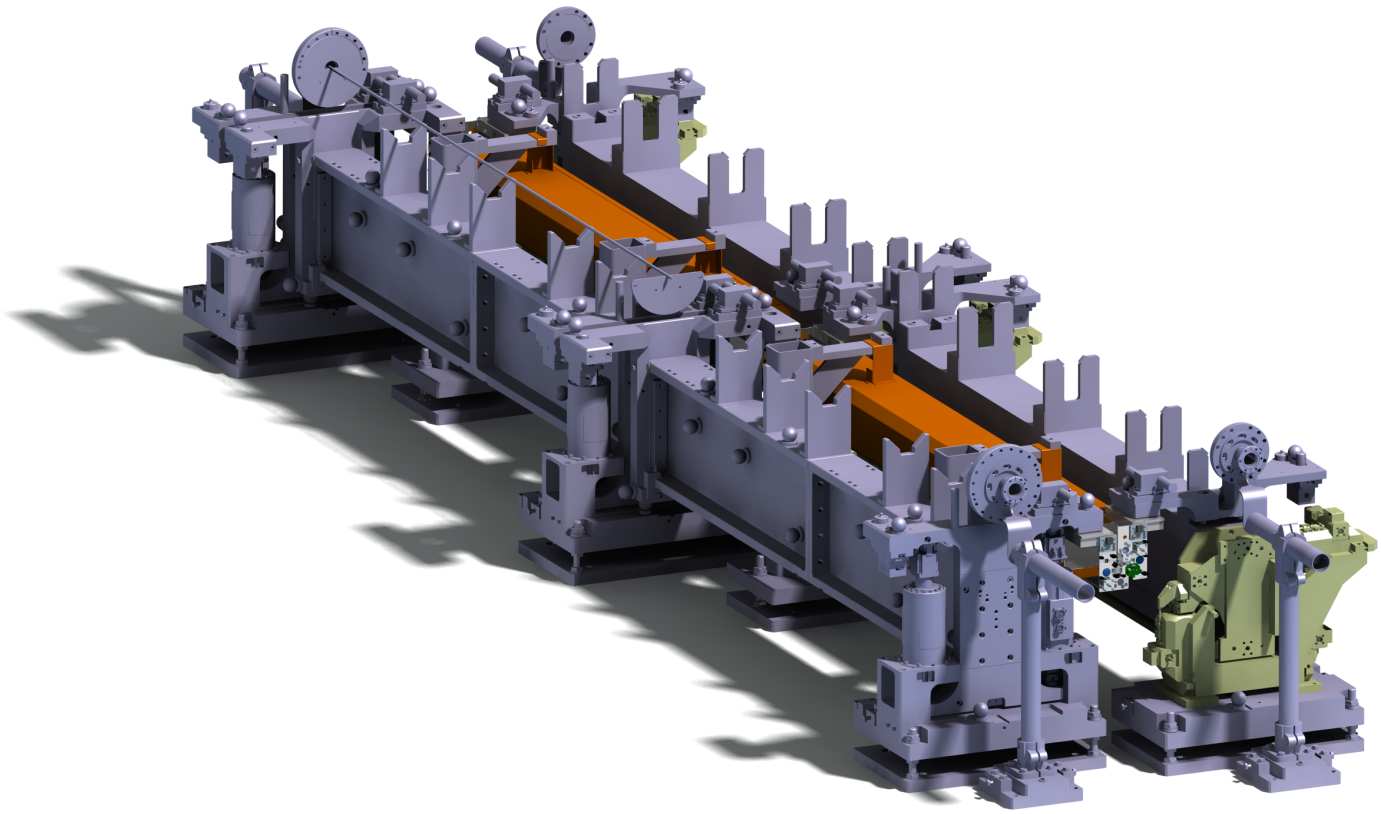

Figure 7.5: CATIA drawing of the 4 m CLiC alignment mock-up with the thermal shielding ducts, in *orange*, and two more sets of ChainPlates are *hidden* in the set-up: in the middle (lens/ diffration plate are used for 4 m alignment) and at the end (image pixel sensor is used for 4 m alignment)(courtesy of A. Alaei)

the colour of the used LEDs can be changed to alter the dimensions of the Rasnik. Depth of field can even stretch this window where changing the colour of light is the solution. Larger adjustments to the Rasnik dimension are to be solved by changing the lens. For most particular dimensions this has to be a non-standard focal length.

Rasdif can vary system length without much trouble. Adjustments to the laser lights colour, i.e. wavelength, or altering the design of the diffraction plate can both be solutions to the adjustment of the system length. For both Rasnik and Rasdif holds that, if the distances to from the lens or the diffraction plate to the image sensor and the light source are not equal, the see-saw analogy, introduced in §5.1.4, applies. For example, if these distances are not equal and the light source of a Rasnik or Rasdif is moving, the image movement is proportional to the translation of the light source multiplied by the ratio of the distance between lens/ diffraction plate and image sensor and the distance between the light

source and the lens/ diffraction plate. If the light source is closer to the middle, the image moves more than the light source, just as a person on a see-saw that is closer to the rotation point makes the other person move more than he or she does.

7.2 QD0 spoke system

When both linacs of the CLiC are delivering accelerated particles at their ends, these particle beams must be made to *end up at the same place*, i.e. made to collide. The final focussing magnets, denoted QD0, can be aligned with Rasniks and Rasdifs, just as the beam lines of the two linacs. To avoid using space that could be used for (inner tracker) detectors, a different approach than direct alignment is taken. The position information is radially transferred to the outside via wheels of spokes, having spokes of 3.5 m each, as shown in Figure 7.6. The Zerodur spokes have a standard cross section of 6 mm $\times$ 6 mm.

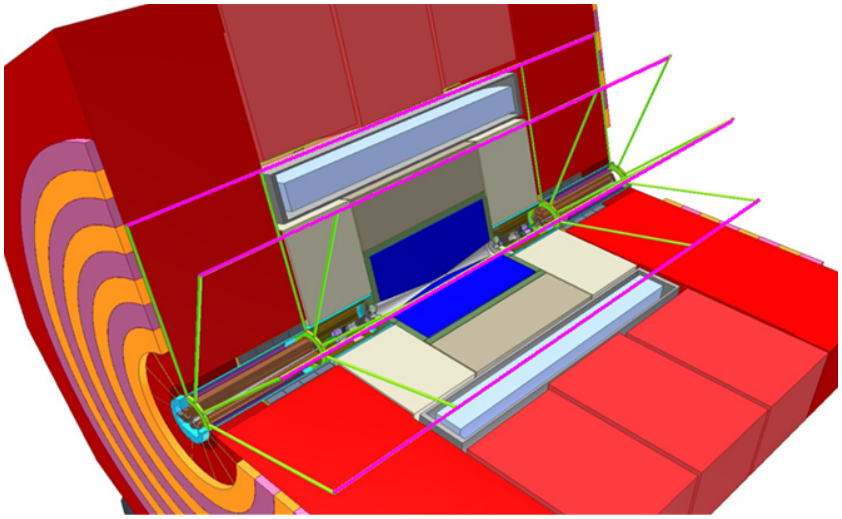

Figure 7.6: The QD0 spoke system aligning the QD0 magnets, avoiding near-vertex-point use of space. The wheels of spokes are indicated in *green* and the optical paths for Rasniks are indicated in *purple*

The spokes are made of Zerodur, a material made by Schott used intensively in (the supporting structures of) large mirrors in telescopes, including Keck I and Keck II [36]. The reason for its use there is the extremely low thermal expansion coefficient, e.g. one can produce mirrors which retain acceptable figures in extremely cold environments such as deep space [37]. In the QD0 alignment case, thermal expansions of the spokes induced by, for example, radiation incident on calorimetric detectors, can result in errors in the radial transfer of the position information. The spokes make contact to a so called reference ring, of which there are

Expansion class	Thermal expansion coefficient
2	$0 \pm 0.10 \times 10^{-6}\ K^{-1}$
1	$0 \pm 0.05 \times 10^{-6}\ K^{-1}$
0	$0 \pm 0.02 \times 10^{-6}\ K^{-1}$
Characteristic	**Value**
Density	$2.53\ gcm^{-1}$
Thermal conductivity at 20 °C	$1.46\ WK^{-1}m^{-1}$
Thermal diffusivity at 20 °C	$0.72 \times 10^{-6}\ m^2s^{-1}$
Thermal capacity	$0.8\ JK^{-1}g^{-1}$
Young's modulus at 20 °C	$90.3\ GPa$
Poisson ratio	0.243

Table 7.1: Thermal expansion coefficients for different classes and other characteristics of Zerodur [38]

two per QD0 magnet, as shown in Figure 7.7(a). A steel semi-sphere ensures a well defined point of contact, as shown in Figure 7.7(b). Producing the spokes using Zerodur, of which the specifications are shown in Table 7.1, is the proposed solution for this problem.

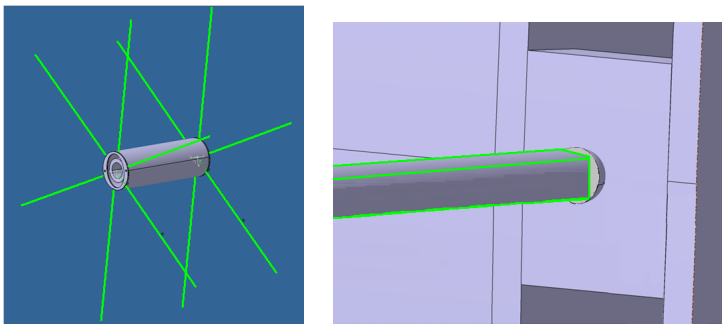

(a) (b)

Figure 7.7: (a) A model of a QD0 magnet with reference rings and Zerodur spokes and (b) a zoom-in at the contact point between a Zerodur spoke and the reference ring (Courtesy of R. Rosing)

As shown in Table 7.1, there are several classes that claim smaller and smaller uncertainties in the thermal expansion coefficient of zero. This smaller and uncertainty comes at a cost, because the ceramic Zerodur is actually a mixture of elements with counteracting thermal expansion coefficients. The quality of the mixture, in terms of homogeneousness and precise absolute amounts of *ingredients*, determines this cost, process-wise as well as financially. To explore and check all these claimed (thermal as well as structural) characteristics and test the workability of Zerodur for the specific purpose of the QD0 spoke system, a 1 m spoke set-up was

constructed at Nikhef.

7.2.1 Design of the 1 m spoke set-up at Nikhef and outlook

To explore and check all the characteristics of Zerodur, shown in Table 7.1, and test the workability of Zerodur for the specific purpose of the QD0 spoke system shown in Figure 7.6, a set-up with a 1 m Zerodur spoke was constructed at Nikhef. This 1 m spoke of Zerodur actually consists of 5 small 20 cm long spokes glued together. The Zerodur spoke is *hung* in the aluminium protection duct by means of flexible rubbers, called *flexos*. At one end of the spoke, a Rasnik mask is attached and a steel semi-sphere is attached to the other end to make contact with the so-called reference block. This reference block is a well defined (low tolerances) shape block. The thermal expansions of both the glue and the steel semi-sphere is not so small and well defined as the Zerodur spoke (sections), but the dimensions of both are so small with respect to the total distance of the spoke that their influence is expected to be small, if not unmeasurable by the *100 nm* resolution 60 mm Rasnik. Designed by H. van der Graaf, G. Brouwer and A. Alaei, the design of the set-up is shown in Figure 7.2.1.

The three main measurements done on this set-up should result in the quantification of the quality of the position transfer by the semi-sphere, the thermal expansion coefficient and the Young's modulus. The semi-sphere is pressed onto the reference block by means of springs, so that the force applied can be kept relatively constant every subsequent test contact. Heating the Zerodur shouldn't make it expand, so a readout of the thermal expansion of the table to set-up is on is expected. Applying a compressive force to the spoke should compress the spoke according to (a form of) Hooke's law:

$$E \equiv \frac{\text{stress}}{\text{strain}} = \frac{F/A_0}{\Delta L/L} = \frac{FL}{A_0 \Delta L} \tag{7.1}$$

In equation 7.1, E is Young's modulus, A_0 is the area where the force is applied (6 mm $\times$ 6 mm in this case) and L is the length of the spoke.

Expanding the set-up to three spokes is the next step, for which there are already two more holes in the steel structure around the reference block. The two extra spokes are then fitted with the lens and the pixel image sensor. The next step is constructing 3.5 m spokes and testing their performance under different angle with respect to the direction of gravity, as is the case in the wheel. The final set-up is a complete mock-up of a wheel, where the performance of the complete QD0 spoke system can be validated.

7.2.2 Preliminary results of the 1 m spoke set-up

The contact made by the steel semi-sphere with the reference block ideally gives the same Rasnik x readout every time the contact is made. Springs

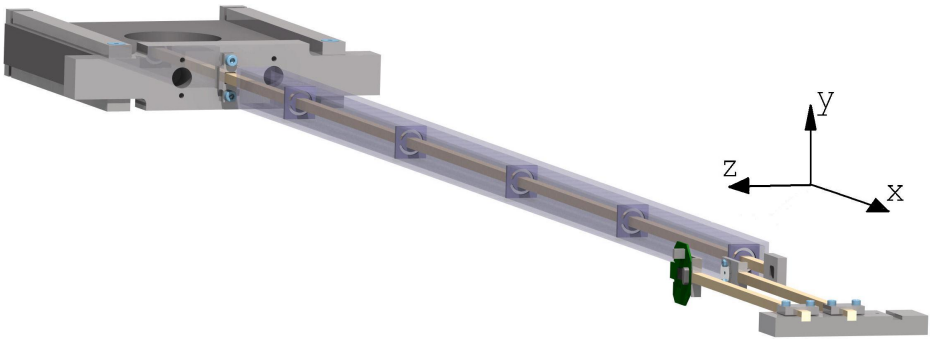

(a)

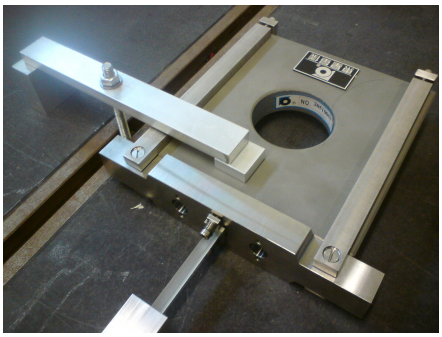

(b)

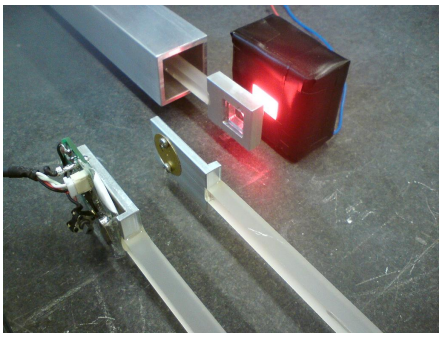

(c)

Figure 7.8: (a) CATIA drawing of the 1 m Zerodur spoke set-up (Courtesy of A. Alaei), (b) a photograph of one end the Zerodur spoke making contact with the reference block and (c) a photograph of the other end of the Zerodur spoke with a Rasnik (mask) attached to it

pushing the Zerodur rod against the reference block apply the *same* force to ensure this *constant* contact position in the x direction. The results of a measurement where the rod is pulled away by hand from the reference block and released again to be pressed to the reference ring by the springs is shown in Figure 7.9.

The pulling away of the spoke, thus moving the Rasnik mask, is visible in the readout as the peaks downward in Figure 7.9(a). The movement of y during the pulling of the Zerodur rod in the x direction is attributed to the flexos. The flexos bend a bit during the movement of the rod and thus the entire rod moves a bit downwards. When the rod is pressed back into contact position, the y coordinate does not return to its initial value. This is attributed to a *stick and shift* behaviour of the flexos. Before the start of measurement, (one of) the flexos could have been bended. When the first rod movement is made, the bending is increased so that at some point the outer edges of the flexos loose grip and move along with the rod. Other stick and shift scenarios can be thought of as well and all can explain a *permanent* movement in the y direction of the Rasnik mask.

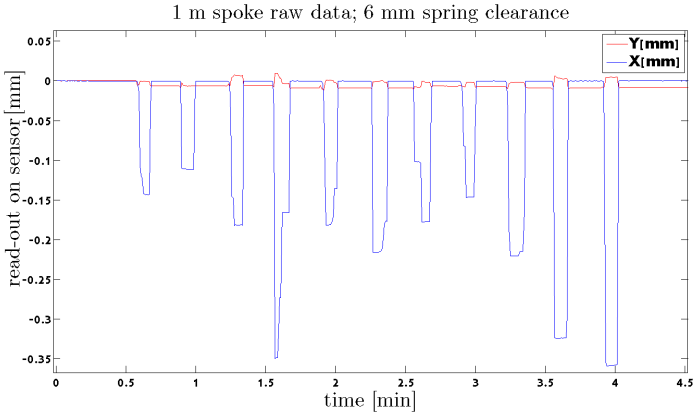

(a)

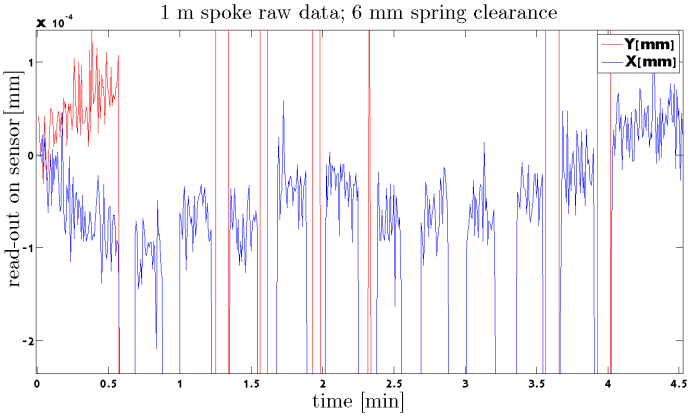

(b)

Figure 7.9: (a) Semi-sphere to reference block contact repeatability measurements. The end of the spoke is pulled off contact by hand and pushed back by the springs and (b) a zoom-in at the contact x coordinate

The contact repeatability in the x direction is shown in Figure 7.9(b). For 12 *different contacts* the x position are in a 150-200 nm *window*.

The 1 m spoke set-up is placed on a granite table as is visible in the photographs of Figure 7.2.1. During a decrease in temperature, the granite contracts and the mask is pushed away from the reference block side by the *non-expanding* Zerodur. The camera (lens and image sensor) are pulled to the opposite side by the contracting granite. Thus a readout of the expansion of the granite over 1 m should be visible. This contracting over 1 m is determined by the coefficient of thermal expansion (CTE) of granite and the change in temperature. The CTE for granite is 6.3 $\times$ 10^{-6} K^{-1} [38], so this predicts a 6 μm contracting of 1 m of granite for every degree of change in temperature. The results of a measurement over 4 nights is shown in Figure 7.10

The temperature is measured by a Lascar EL-USB-1 Temperature

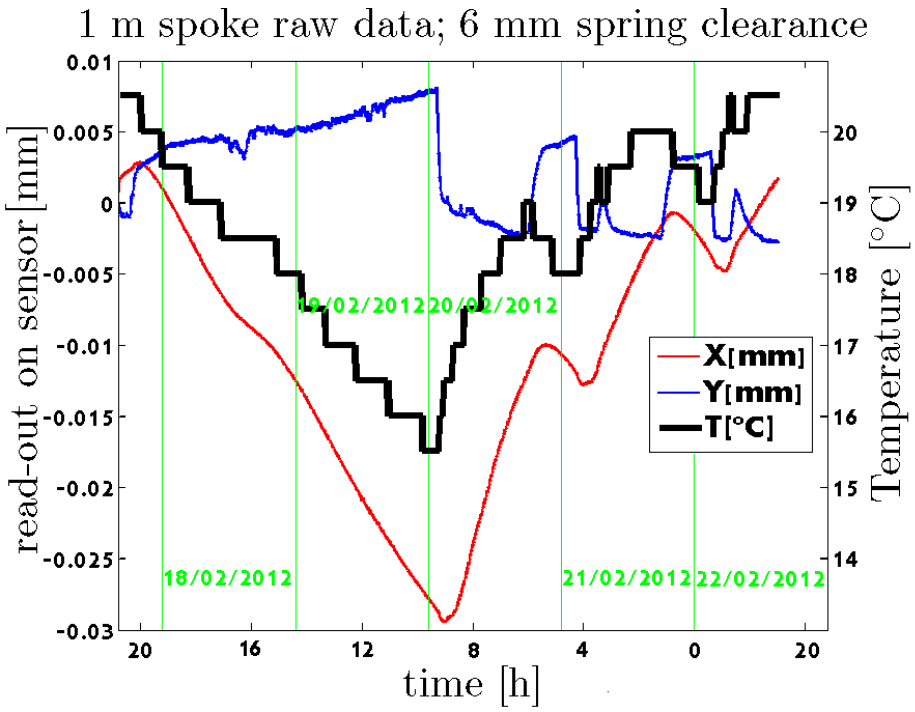

Figure 7.10: 4 day Rasnik measurement of the expansion of granite table and temperature. The x coordinate is in the length direction of the 1 m Zerodur spoke

Data Logger, which has a resolution of 0.5 °C, as is visible in the steps of the temperature measurement in Figure 7.10. The measurement started on a Friday, so the first decrease of temperature is the cooling of the lab during the weekend. The contracting of the table is visible as a decrease in the x position readout of the Rasnik, which shows a delay with respect to the temperature behaviour. This is due to the slower heating and cooling of granite than air. Over the weekend the x coordinate decreases approximately 32 μm. The temperature has decreased 5 $\pm$ 0.25 °C. A granite contraction of 31.5 $\pm$ 0.16 μm is expected during this temperature evolution. Comparing this value with the measured 32 μm by the Zerodur spoke gives a 1.6 percent deviation.

Applying a compressive force to the spoke is done by pressing a small spring against the mask holder at the end of the spoke. The spring force is calibrated by pressing it on a weighing scale until it has a certain *calibration length*. The force the spring exerts on the weighing scale is simply the reading of the weighing scale times the free fall acceleration constant. The spring, which as a *rest* length of 45 mm, is then pressed against the mask until it has the same length as the calibration lengths. The on screen Rasnik readout is then noted down and the results are shown in Table 7.2.

Spring length [mm]	Spring force weight [kg]	Rasnik μm x readout
45	0	830 μm
40	1.3	827 μm
35	2.7	825 μm
30	4.0	817 μm

Table 7.2: Measurement for Young's modulus determination of the 1 m Zerodur spoke

The force corresponding to the weight measurement of the spring (1.3 kg, 2.7 kg and 4.0 kg) is 12.8 N, 26.5 N and 39.2 N respectively. In Figure 7.11 a plot of measured contractions and the expected contraction is shown. The order of magnitude of the Young's modulus is confirmed, as is the goal of such a coarse measurement. The material not buckling under its own weight is an important attribute for its proposed use in the QD0 spoke system.

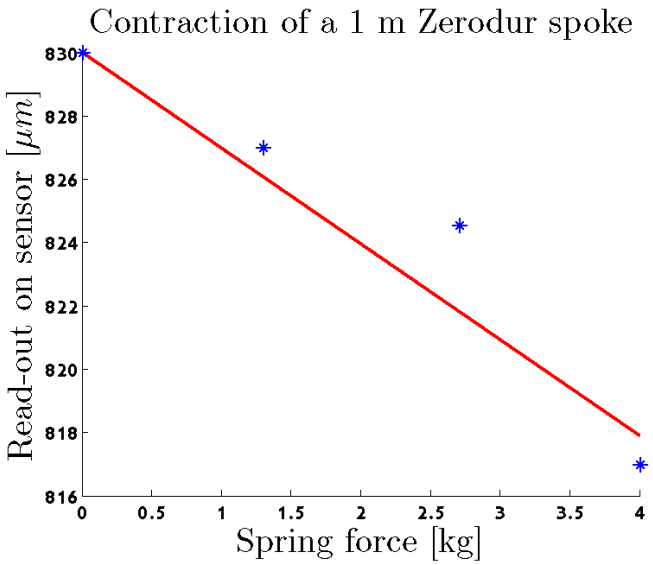

Figure 7.11: Contraction measurement of a 1 m Zerodur spoke. The expected contraction, governed by the Young's modulus, is plotted in *red*

Chapter 8

Conclusions and Recommendations

8.1 Conclusions

After several years of 91 m and 140 m Rasdif development in the TT1 set-up at CERN, research of this alignment system is also conducted for smaller sized Rasdifs. The characteristics of an intermediate sized 4 m Rasdif, operated parallel with 4 m Rasniks, have been investigated at Nikhef. Further development on the light source of the 140 m double Rasdif (RasCLiC) towards larger number implementation has been done in collaboration with the Accelerator & Beam Physics Survey and Alignment group at CERN. Moreover, the first step towards a solution for the alignment of the final focusing magnets of the CLiC (QD0) has been made by building a 1 m Zerodur spoke set-up at Nikhef.

The fact that the Rasdif does not align on the physical location of the laser, but on the virtual point of departure (VPoD) of the spherical waves the laser emits, was discovered and investigated. Two independent methods of measurement can quantify the VPoD location and its effect of the slope, defined as the ratio of the read out versus the applied translation. The asymptotic VPoD characteristic of a simple focusable diode laser were investigated and confirmed by a simple geometrical model.

Confirmation by this model meant the VPoD issue was understood and a search for a small laser, implementable in intermediate sized alignment, could commence. A DPSS laser, stripped out of an ordinary laser pointer, has proved to have a VPoD close to the physical location of the laser. The measured slope of about 0.98 translates to a VPoD about 4 cm behind the laser medium. The downside to this type of laser is the relatively large dissipation. This heats up the laser and the structure around it, potentially compromising the precision. The temperature rise of the structure around the laser may result in translation of the laser medium whilst there is no translation of the point to be aligned.

The diffraction plate in the present 4 m set-up has a outer radius of

1.44 mm, a scaled version of the diffraction plates of the 140 m RasCLIC in the TT1 set-up. Two dimensional shift estimation Cramér-Rao Lower Bound (CRLB) analysis of simulated Rasdif images show that diffraction plates scaled to larger dimensions can result in more gradient energy in the Rasdif images. The first two peaks in a gradient energy versus outer radius plot are found at an outer radius of approximately 1.90 mm and 2.55 mm. This increased gradient energy theoretically lead to smaller CRLBs by a factor 2.5 or 3.75 respectively.

Response to applied transitions of the 4 m Rasniks and Rasdif match closely, a part from the somewhat smaller slope of the Rasdif, which again is about 0.98 for both Rasdifs. When applying a weight to the diffraction plate of the 140 m RasCLiC in and evening and morning measurement in the TT1 set-up, both WPSs give a translation readout of about 70 μm. The RasCLiC readout is different for both measurements and reads 125 μm and 60 μm respectively.

The rms resolutions of the 4 m Rasniks and Rasdifs is similar in both x and y directions. Without any thermal shielding, the rms resolution for both systems is about 5-10 μm. Thermal shielding of the optical path by means of aluminium ducts with DIY store rockwool folded around it is applied. This enhances the rms resolution of both systems by about a factor of 10 to 0.5-1 μm. The rms resolution of the 140 m RasCLiC in a vacuum of 1.5 $\times 10^{-4}$ mbar is 1.5-2 μm.

Preliminary results show a 1 m spoke of Zerodur, to be used in the alignment of the QD0 magnets of the CLiC, has the expected behaviour. The contact repeatability of the end of the spoke, with a steel semi-sphere glued on, with a reference block is within 150-200 nm. The set-up, being placed on a granite table, is able to reconstruct the coefficient of linear thermal expansion (CTE) of granite with great precision, which strengthens the Zerodur claim that its CTE is 0. The order of magnitude of the Zerodur material is confirmed so that Zerodur seems the material that should be used for the QD0 spoke system.

8.2 Recommendations

With the introduction of the DPSS laser in the 4 m set-up as well as the 140 m set-up, a small high intensity laser with the desired VPoD characteristics is found. The high intensity comes with a price as the dissipation of electrical energy heats up the laser and the (laser) structures around it. In vacuum operation at the TT1 set-up, the cooling of the laser via its mount has proven to be inadequate resulting in a break down of the laser. Solutions for sufficient heat transfer away from the laser or even cooling solutions should be looked into.

New diffraction plates for the 4 m set-up and RasChain solution as well as for the 140 m RasCLiC should be ordered. CRLB analysis of simulated 4 m Rasdif images show a resonant behaviour in the gradient energy for

images resulting from scaled versions of the used diffraction plates. The recommended outer radius of the diffraction plate to be ordered is 2.55 mm. Larger radii diffraction plates will not result in substantial decrease in the CRLV and will result in finer and finer diffraction patterns. These fine diffraction patterns will be blurred by thermally induced jitter and more gradient energy will be lost to this than for less fine diffraction patterns. The same resonant behaviour is expected for 140 m Rasdif image simulation when scaling the current RasCLiC diffraction plate.

Thermal shielding by ducts in the 4 m set-up and the RasChain design decrease the thermal gradients across the optical path, but currents of air can still flow freely in the longitudinal direction of the duct. These flows of air may induce the same effects as the thermally induced jitter. Sealing of the ducts by means of optical windows is a way to counter these flows of air.

Rasdif software development is still ongoing. Present software analysis uses the first image of a measurement as the reference image. This image carries the noise introduced by the system and using a simulated image a reference image does not contain this noise. Image quality enhancement before using the images for the shift estimation by *super-resolution techniques* should also not go unexplored.

The measured RasCLiC 1.5-2 μm resolution is still far away from the obtained 20 nm resolution in 2008 [19]. This resolution was obtained with the fibre coupled HeNe laser, which possibly resulted in a more stable beam of light than the DPSS lasers out of a laser pointer. After solving the cooling issues with this laser, a vacuum stability measurement of the new mount is recommended.

As the RasCLiC system shows different readout from measurement to measurement for the same applied translations in a direction perpendicular to the optical path, a translational linearity measurement in a non-vacuum (standard atmospheric pressure) is recommended. The deviations in the measurements of February 7 and 8 differ by a factor of 2 and this is ill understood.

Bibliography

[1] Dylla, HF 2006 *The Development of UHV and XHV for Physics Research*, viewed 30 November 2011, <cas.web.cern.ch/cas/Spain-2006/PDFs/Dylla-3.pdf>

[2] Baker, M 2007 *Medical Linear Accelerator Celebrates 50 years of treating cancer*, viewed 30 November 2011, <news.stanford.edu/news/2007/april18/med-accelerator-041807.html>

[3] Suhag, MV et. al. 2010 *Radiotherapy : Basic Concepts and Recent Advances* <http://medind.nic.in/maa/t10/i2/maat10i2p158.pdf>

[4] Herrmannsfeldt, WB 1968 'Precision Alignment Using a System of Large Rectangular Fresnel Lenses', *Applied Optics*, vol. 7, issue 6, pp. 995-1005

[5] Varian, RH, Varian ,SF 'A High Frequency Oscillator and Amplifier', *J. Appl. Phys.* 10, 321 (1939); doi:10.1063/1.1707311

[6] Pagani, C 2003 *Overview of Linear Collider Status and Perspectives* <http://www.desy.de/f/seminar/Pagani.pdf>

[7] Scrivens, R 2008 *Cern Hadron Linacs*, viewed 12 December 2011, <http://linac2.home.cern.ch/linac2/default.htm>

[8] Fermilab National Accelerator Laboratory 2011, *The Fermilab accelerator complex after the Tevatron shutdown* , viewed 12 December 2011 <http://www.fnal.gov/faw/future/accelerators.shtml>

[9] SLAC National Accelerator Laboratory 2011, *Scientific Achievements and Contributions*, viewed 12 December 2011 <http://home.slac.stanford.edu/achievements/>

[10] Griffith, LV 1989 *The Poisson Line as a Straight Line Reference*, Livermore, CA, Lawrence Livermore National Laboratory

[11] Quesnel, JP, Mainaud Durand, H, Touzé,T 2008 *Streched Wire Offset Measurements: 40 Years of Practice of this Technique at CERN*, Geneva, CERN

[12] Bestmann, P et. al. 2010 *Validation of an optical WPS system*, poster, 11th International Workshop on Accelerator Alignment (Desy, Hamburg, Germany), Geneva, CERN

[13] Seryi, A et.al. 2001 'Hydrostatic Level System for Slow Ground Motion Studies at Fermilab and SLAC', *Proceedings of the 2001 Particle Accelerator Conference*, Chicago, IL, pp. 1479-1481

[14] Clements, E 2005 *The Compact Linear Collider*, viewed 21 December 2011, <http://www.symmetrymagazine.org /cms/?pid=1000156>

[15] Assmann, AW et.al 2000 *A 3 TeV e^+e^- Linear Collider based on CLiC Technology*, CERN report (number:CERN-2000-008), CERN, Geneva

[16] Delahaye, JP 2008 *Reminder of CLIC Objectives and Scheme CLIC Feasibility Issues RDprogram, Status and Plans*, viewed 1 December 2011, <clic-study.web.cern.ch/clic-study/Presentations/FRXCMH01_TALK.pdf>

[17] Duinker, P et al. 1988 *Some methods and tools for Testing and optimizing Proportional Wire Chambers*, Nikhef, Amsterdam

[18] Kea, M 2007 'FOAM: An Image Analysis Routine for the ATLAS Barrel Muon Spectrometer Alignment System', Amsterdam, NIKHEF

[19] Beker, M 2008 'RasClic: A Long Base, Low Frequency,High Precision Seismograph', MSc thesis, Nikhef, Amsterdam

[20] van der Geer, R 2008 'A Diffraction Simulation for RasClic', MSc thesis, Nikhef, Amsterdam

[21] Elmore, WC, Heald, MA 1985 *Physics of Waves*, Courier Dover Publications, Mineola, NY

[22] Rodriguez, C 2007 *Understanding FFT- based algorithm to calculate image displacements with IDL programming language*, University of Texas, San Antonio, <http://www.utsa.edu/lrsg/Teaching/EES5053-06/project/ Cynthia.pdf>

[23] Mainaud Durand, H et.al. 2010 'CLiC Active Pre-alignment System: Proposal for CDR and program from TDR', *Proceedings of the 11th International Workshop on Accelerator Alignment*, DESY, Hamburg

[24] Mainaud Durand, H, Touzé 2006 *The CLiC active prealignment studies*, viewed 7 December 2011, <www.opensourceinstruments.com/WPS/CLIC/CLIC.pdf>

[25] Birch, KP, Downs, MJ 1994 'An Updated Edlén Equation for the Refractive Index of Air', *Metrologia*, 1994, 31, pp. 155-162

[26] Léna, P et. al. 1986 *Observational Astrophysics*, 2^{nd} edition (1996), Springer-Verlag, Berlin

[27] Dispersion Relations 2010, viewed 9 January 2012, <http://www.cvimellesgriot.com/products/Documents/Catalog/Dispersion_Equations.pdf>

[28] Rieke, G 1994 *Detection of light—From the Ultraviolet to the Submillimeter*, 2^{nd} edition (2003), Cambridge University Press, New York, NY

[29] Rumyantsev, SL et.al. 2005 'Low-frequency noise of GaN-based ultraviolet light-emitting diodes', *Journal of Applied Physics*, vol. 97, no. 123107, pp. 1-5

[30] Rosing, R 2011, *RasClic—Shielding optical path*, Nikhef, Amsterdam

[31] Kay, SM 1993 *Fundamentals of Statistical Signal Processing: Estimation Theory*, Prentice Hall, Upper Saddle River, NJ

[32] Van der Hof, P, den Dekker, A 2010 *Signal Analysis and Estimation*, lecture notes, Delft University of Technology, Delft

[33] Pham, TQ et.al 2006 *Performance of Optimal Registration Estimators*, Delft, Delft University of Technology

[34] Robinson, MD, Milanfar, P 2004 'Fundamental Performance Limits in Image Registration', *IEEE Transactions on Image Processing*, Vol. 13, no.9, pp.1185-1199

[35] Samoshkin, A et. al. 2011 *CLiC Two Beam Module for the CLiC Conceptual Design and Related Experimental Program*, poster, International Particle Accelerators Conference (4-9 September, San Sebastian, Spain), Geneva, CERN

[36] Döhring, T Properties of Zerodur Mirror Blanks for Extremely Large Telescopes, *Proceedings of SPIE*, Vol. 6148, 61480G-8, viewed January 30, <http://www.optics.arizona.edu/optomech/Fall10/grad%20student%20reports/Properties%20of%20Zerodur%20Mirrors%20for%20Large%20Telescopes.pdf>

[37] Baer, JW, Lotz, WP 1998 *Figure testing of 300 mm Zerodur mirrors at cryogenic temperatures*, Ball Aerospace & Technologies, Boulder, CO, viewed January 30, <http://www.4dtechnology.com/reflib/Figure%20testing%20of%20300%20mm%20Zerodur%20mirrors%20at%20cryogenic%20temper.pdf>

[38] ZERODUR® Zero Expansion Glass Ceramic, viewed January 30, <http://www.schott.com/advanced_optics/english/our_ products/zerodur/zerodur.html?so= benelux& lang=english& PHPSESSID=9u64v2fmura3c99nftntjg2525>

[38] Doiron, T 2004, *CTE for Some Common Materials*, viewed February 21, <http://emtoolbox.nist.gov/Temperature/Slide14.asp>

Appendix A

Used Matlab code

In this appendix several Matlab m-files, i.e. scripts, are displayed. The text colours are taken from Matlab standard colour scheme. Most plotting code and all pre-allocation of used *cells* and *vectors* are not displayed here.

A.1 Ray tracing light with different wavelengths

In order to investigate the chromatic aberration effect, the code following in the subsections below is used. In order to understand the code, the denominations of different distances, heights and angles has been schematically drawn in Figure A.1.

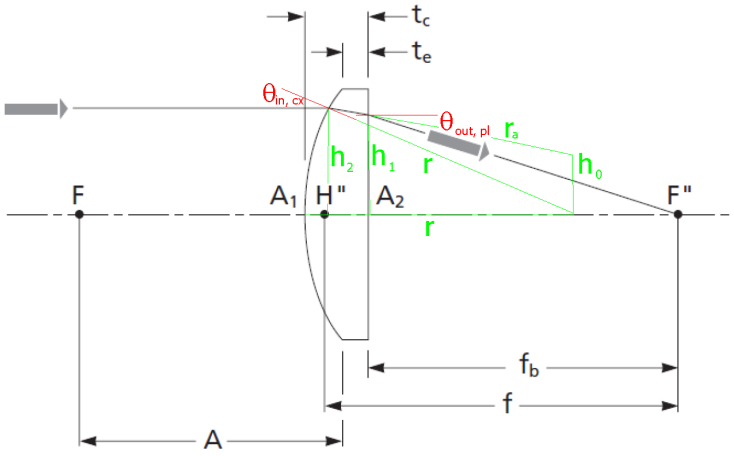

Figure A.1: Denomination explanation of the different distances, heights and angles in the two ray tracing models

For redundancy and cross-check reasons, two ray tracing configurations were made: a model where the planar surface of the planar-convex lens faced the object and another model where it is the convex surface

faced the object.

A.1.1 Planar surface of the lens towards the object

The code for ray tracing from a point a distance height away from the optical axis, rays emitted with different angles with respect to the optical axis. The planar-convex lens is positioned as such that the planar surface is towards the object (starting point of the rays of light). Different wavelengths— red (650 nm), green (535 nm) and blue(400 nm) —are investigated to quantify the chromatic aberration effect described in §5.1.3.

```
%Schott BK7 constants of the dispersion formula
B1=1.03961212;
B2=2.31792344*10^-1;
B3=1.01046945;
C1=6.00069867*10^-3;
C2=2.00179144*10^-2;
C3=1.03560653*10^2;

%Dispersion formula for BK7 and air
wvlngth=0.35:0.0005:0.85;
nBK7=zeros(length(wvlngth),1);
nair=zeros(length(wvlngth),1);

for i=1:length(wvlngth)
nBK7(i)=sqrt(1+(B1*wvlngth(i)^2)/(wvlngth(i)^2-C1)+(B2*...
    wvlngth(i)^2)/(wvlngth(i)^2-C2)+(B3*wvlngth(i)^2)/...
(wvlngth(i)^2-C3));
nair(i)=(10^-8)*(8342.54+2406147*((130-(1/wvlngth(i))...
    ^2)^-1)+15998*((38.9-(1/wvlngth(i))^2)^-1));
end
%incoming light with variable ang for 10 to 80 degrees
height=input('At what height is the starting point
of all rays? [mm] ');
v=input('What is the distance between mask and planar
lens surface? [mm] ');
%dimage-lens (A2-H"=-2.0)
anginplrad=0:0.001:(atan(1.75*height/v));
r=7.781;
tc=3.1;
h1=height-tan(anginpl)*v;

%Ray trace through the lens
for j=1:length(h1)
```

```
angoutplbl(j)=asin(((nair(101)+1)/nBK7(101))*sin(anginpl(j)));
angoutplgr(j)=asin(((nair(371)+1)/nBK7(371))*sin(anginpl(j)));
angoutplrd(j)=asin(((nair(601)+1)/nBK7(601))*sin(anginpl(j)));
h0bl(j)=h1(j)+tan(angoutplbl(j))*(r-tc);
h0gr(j)=h1(j)+tan(angoutplgr(j))*(r-tc);
h0rd(j)=h1(j)+tan(angoutplrd(j))*(r-tc);
if h1(j)-tan(angoutplbl(j))*tc > 0
 rabl(j)=h0bl(j)*cos(pi/2-angoutplbl(j))*(1+0.5*sqrt(4-...
 4*(h0bl(j)^2-r^2)/(h0bl(j)^2*cos(pi/2-angoutplbl(j))^2)));
elseif h1(j)-tan(angoutplbl(j))*tc < 0  & &  h0bl(j) > 0
 rabl(j)=h0bl(j)*cos(pi/2-angoutplbl(j))*(1+0.5*sqrt(4-...
 4*(h0bl(j)^2-r^2)/(h0bl(j)^2*cos(pi/2-angoutplbl(j))^2)));
else
 rabl(j)=abs(h0bl(j))*cos(pi/2+angoutplbl(j))*(1-0.5*sqrt(4-...
 4*(h0bl(j)^2-r^2)/(h0bl(j)^2*cos(pi/2+angoutplbl(j))^2)));
end
if h1(j)-tan(angoutplgr(j))*tc > 0
 ragr(j)=h0gr(j)*cos(pi/2-angoutplgr(j))*(1+0.5*sqrt(4-...
 4*(h0gr(j)^2-r^2)/(h0gr(j)^2*cos(pi/2-angoutplgr(j))^2)));
elseif h1(j)-tan(angoutplgr(j))*tc < 0  & &  h0gr(j) > 0
 ragr(j)=h0gr(j)*cos(pi/2-angoutplgr(j))*(1+0.5*sqrt(4-...
 4*(h0gr(j)^2-r^2)/(h0gr(j)^2*cos(pi/2-angoutplgr(j))^2)));
else
 ragr(j)=abs(h0gr(j))*cos(pi/2+angoutplgr(j))*(1-0.5*sqrt(4-...
 4*(h0gr(j)^2-r^2)/(h0gr(j)^2*cos(pi/2+angoutplgr(j))^2)));
end
if h1(j)-tan(angoutplrd(j))*tc > 0
 rard(j)=h0rd(j)*cos(pi/2-angoutplrd(j))*(1+0.5*sqrt(4-...
 4*(h0rd(j)^2-r^2)/(h0rd(j)^2*cos(pi/2-angoutplrd(j))^2)));
elseif h1(j)-tan(angoutplrd(j))*tc < 0  & &  h0rd(j) > 0
 rard(j)=h0rd(j)*cos(pi/2-angoutplrd(j))*(1+0.5*sqrt(4-...
 4*(h0rd(j)^2-r^2)/(h0rd(j)^2*cos(pi/2-angoutplrd(j))^2)));
else
 rard(j)=abs(h0rd(j))*cos(pi/2+angoutplrd(j))*(1-0.5*sqrt(4-...
 4*(h0rd(j)^2-r^2)/(h0rd(j)^2*cos(pi/2+angoutplrd(j))^2)));
end
angincxbl(j)=acos((-h0bl(j)^2+r^2+rabl(j)^2)/(2*r*rabl(j)));
angincxgr(j)=acos((-h0gr(j)^2+r^2+ragr(j)^2)/(2*r*ragr(j)));
angincxrd(j)=acos((-h0rd(j)^2+r^2+rard(j)^2)/(2*r*rard(j)));
angoutcxbl(j)=asin(nBK7(101)/(nair(101)+1)*sin(angincxbl(j)));
angoutcxgr(j)=asin(nBK7(371)/(nair(371)+1)*sin(angincxgr(j)));
angoutcxrd(j)=asin(nBK7(601)/(nair(601)+1)*sin(angincxrd(j)));
if h1(j)-tan(angoutplbl(j))*tc > 0
 angr2bl(j)=(-angoutplbl(j)+angincxbl(j));
 angoutcxparallelbl(j)=angoutcxbl(j)-angr2bl(j);
```

```
 tcxbl(j)=cos(angr2bl(j))*r-r+tc;
 h2bl(j)=sqrt(r^2-(r-tc+tcxbl(j))^2);
 bbl(j)=60-(v+tcxbl(j));
 Isbl(j)=h2bl(j)-bbl(j)*tan(angoutcxparallelbl(j));
elseif h1(j)-tan(angoutplbl(j))*tc < 0  & &  h0bl(j) > 0
 angr2bl(j)=(angoutplbl(j)-angincxbl(j));
 angoutcxparallelbl(j)=angoutcxbl(j)+angr2bl(j);
 tcxbl(j)=cos(angr2bl(j))*r-r+tc;
 h2bl(j)=-sqrt(r^2-(r-tc+tcxbl(j))^2);
 bbl(j)=60-(v+tcxbl(j));
 Isbl(j)=h2bl(j)-bbl(j)*tan(angoutcxparallelbl(j));
else
 angr2bl(j)=(angoutplbl(j)+angincxbl(j));
 angoutcxparallelbl(j)=abs(angoutcxbl(j)-angr2bl(j));
 tcxbl(j)=cos(angr2bl(j))*r-r+tc;
 h2bl(j)=-sqrt(r^2-(r-tc+tcxbl(j))^2);
 bbl(j)=60-(v+tcxbl(j));
 Isbl(j)=h2bl(j)-bbl(j)*tan(angoutcxparallelbl(j));
end
if h1(j)-tan(angoutplgr(j))*tc > 0
 angr2gr(j)=(-angoutplgr(j)+angincxgr(j));
 angoutcxparallelgr(j)=angoutcxgr(j)-angr2gr(j);
 tcxgr(j)=cos(angr2gr(j))*r-r+tc;
 h2gr(j)=sqrt(r^2-(r-tc+tcxgr(j))^2);
 bgr(j)=60-(v+tcxgr(j));
 Isgr(j)=h2gr(j)-bgr(j)*tan(angoutcxparallelgr(j));
elseif h1(j)-tan(angoutplgr(j))*tc < 0  & &  h0gr(j) > 0
 angr2gr(j)=(angoutplgr(j)-angincxgr(j));
 angoutcxparallelgr(j)=angoutcxgr(j)+angr2gr(j);
 tcxgr(j)=cos(angr2gr(j))*r-r+tc;
 h2gr(j)=-sqrt(r^2-(r-tc+tcxgr(j))^2);
 bgr(j)=60-(v+tcxgr(j));
 Isgr(j)=h2gr(j)-bgr(j)*tan(angoutcxparallelgr(j));
else
 angr2gr(j)=(angoutplgr(j)+angincxgr(j));
 angoutcxparallelgr(j)=abs(angoutcxgr(j)-angr2gr(j));
 tcxgr(j)=cos(angr2gr(j))*r-r+tc;
 h2gr(j)=-sqrt(r^2-(r-tc+tcxgr(j))^2);
 bgr(j)=60-(v+tcxgr(j));
 Isgr(j)=h2gr(j)-bgr(j)*tan(angoutcxparallelgr(j));
end
if h1(j)-tan(angoutplrd(j))*tc > 0
 angr2rd(j)=(-angoutplrd(j)+angincxrd(j));
 angoutcxparallelrd(j)=angoutcxrd(j)-angr2rd(j);
 tcxrd(j)=cos(angr2rd(j))*r-r+tc;
```

```
 h2rd(j)=sqrt(r^2-(r-tc+tcxrd(j))^2);
 brd(j)=60-(v+tcxrd(j));
 Isrd(j)=h2rd(j)-brd(j)*tan(angoutcxparallelrd(j));
elseif h1(j)-tan(angoutplrd(j))*tc < 0  & &  h0rd(j) > 0
 angr2rd(j)=(angoutplrd(j)-angincxrd(j));
 angoutcxparallelrd(j)=angoutcxrd(j)+angr2rd(j);
 tcxrd(j)=cos(angr2rd(j))*r-r+tc;
 h2rd(j)=-sqrt(r^2-(r-tc+tcxrd(j))^2);
 brd(j)=60-(v+tcxrd(j));
 Isrd(j)=h2rd(j)-brd(j)*tan(angoutcxparallelrd(j));
else
 angr2rd(j)=(angoutplrd(j)+angincxrd(j));
 angoutcxparallelrd(j)=abs(angoutcxrd(j)-angr2rd(j));
 tcxrd(j)=cos(angr2rd(j))*r-r+tc;
 h2rd(j)=-sqrt(r^2-(r-tc+tcxrd(j))^2);
 brd(j)=60-(v+tcxrd(j));
 Isrd(j)=h2rd(j)-brd(j)*tan(angoutcxparallelrd(j));
end
end
```

A.1.2 Convex surface of the lens towards the object

The code for ray tracing from a point a distance height away from the optical axis, rays emitted with different angles with respect to the optical axis. The planar-convex lens is positioned as such that the convex surface is towards the object (starting point of the rays of light). Different wavelengths— red (650 nm), green (535 nm) and blue(400 nm) —are investigated to quantify the chromatic aberration effect described in §5.1.3.

```
%incoming light with variable ang for 10 to 80 degrees
height=input('At what height is the starting point
of all rays? [mm] ');
b=input('What is the distance between planar lens
surface and pixel image sensor? [mm] ');
tc=3.1;
v=60-b-tc;
r=7.781;
y=-0.85*height:0.05:height;
x=sqrt(r^2-y.^2);
angoutpoint=atan((height-y)./(v+(r-x)));
%Ray trace through the lens
for  i=1:length(angoutpoint)
if  angoutpoint(i) < atan(y(i)/x(i)) & & y(i) > 0;
 angincx(i)=pi/2-(angoutpoint(i)+atan(x(i)/y(i)));
```

```
 angoutcxblue(i)=asin(((nair(101)+1)...
 /nBK7(101))*sin(angincx(i)));
 angoutcxgreen(i)=asin(((nair(371)+1)...
 /nBK7(371))*sin(angincx(i)));
 angoutcxred(i)=asin(((nair(601)+1)...
 /nBK7(601))*sin(angincx(i)));
 angoutcxparblue(i)=atan(y(i)/x(i))-angoutcxblue(i);
 angoutcxpargreen(i)=atan(y(i)/x(i))-angoutcxgreen(i);
 angoutcxparred(i)=atan(y(i)/x(i))-angoutcxred(i);
elseif  angoutpoint(i) > atan(y(i)/x(i)) & & y(i) > 0;
 angincx(i)=angoutpoint(i)-atan(y(i)/x(i));
 angoutcxblue(i)=asin(((nair(101)+1)...
 /nBK7(101))*sin(angincx(i)));
 angoutcxgreen(i)=asin(((nair(371)+1)...
 /nBK7(371))*sin(angincx(i)));
 angoutcxred(i)=asin(((nair(601)+1)...
 /nBK7(601))*sin(angincx(i)));
 angoutcxparblue(i)=atan(y(i)/x(i))+angoutcxblue(i);
 angoutcxpargreen(i)=atan(y(i)/x(i))+angoutcxgreen(i);
 angoutcxparred(i)=atan(y(i)/x(i))+angoutcxred(i);
elseif  y(i) <= 0
 angincx(i)=angoutpoint(i)+atan(abs(y(i))/x(i));
 angoutcxblue(i)=asin(((nair(101)+1)...
 /nBK7(101))*sin(angincx(i)));
 angoutcxgreen(i)=asin(((nair(371)+1)...
 /nBK7(371))*sin(angincx(i)));
 angoutcxred(i)=asin(((nair(601)+1)...
 /nBK7(601))*sin(angincx(i)));
 angoutcxparblue(i)=-atan(abs(y(i))/x(i))+angoutcxblue(i);
 angoutcxpargreen(i)=-atan(abs(y(i))/x(i))+angoutcxgreen(i);
 angoutcxparred(i)=-atan(abs(y(i))/x(i))+angoutcxred(i);
end
yplanarblue(i)=y(i)-tan(angoutcxparblue(i))*(tc-r+x(i));
yplanargreen(i)=y(i)-tan(angoutcxpargreen(i))*(tc-r+x(i));
yplanarred(i)=y(i)-tan(angoutcxparred(i))*(tc-r+x(i));
angoutplblue(i)=asin((nBK7(101)/(nair(101)+1))...
 *sin(angoutcxparblue(i)));
angoutplgreen(i)=asin((nBK7(371)/(nair(371)+1))...
 *sin(angoutcxpargreen(i)));
angoutplred(i)=asin((nBK7(601)/(nair(601)+1))...
 *sin(angoutcxparred(i)));
Isblue(i)=yplanarblue(i)-tan(angoutplblue(i))*b;
Isgreen(i)=yplanarred(i)-tan(angoutplgreen(i))*b;
Isred(i)=yplanarred(i)-tan(angoutplred(i))*b;
end
```

A.2 Virtual point model and comparison with the measurements

The virtual point of departure (VPoD) and the effect of it not coinciding with the physical location of the diode laser, emitting a spherical wave diverging beam, is described in §5.1.4. Both methods of investigation, i.e. translation and rotation, and the comparison with the model, explained using equations 5.9 and 5.10 and Figure 5.8, are investigated using this script. The code that plots a model and inserts the experimentally found data point is shown below.

```
v=194;% distance laser-plate in cm
r=0.13; % radius laser aperture in cm
focus=-2:0.05:3; % radius laser on plate in cm
% location of virtual point calculation
for i=1:length(focus)
if focus(i)<=-0.1
 virt_dep_pt(i)=(r*v)/(r+focus(i));% 1st order divergence
elseif  focus(i)>=0.05
 virt_dep_pt(i)=(r*v)/(r+focus(i)); %2nd order divergence
else
 virt_dep_pt(i)=NaN;
end
end
% Expected slope calculation
for  i=1:length(focus)
 slope(i)=200/200-virt_dep_pt(i));
end
% Experimental data (20/04/2011, 27/04/2011, 28/04/2011)
focusexp=[-1.75 -1.5 -1.25 -1 -0.75 -0.5 0.25 0.5...
 0.75 1 1.25 1.5 1.75];
slopeexprd1=[0.9568 0.9152 0.8736 0.8516 0.8286 0.7072...
1.477 1.312 1.165 1.123 1.123 1.104 1.082];
slopeexprd2=[0.9361 0.9152 0.9152 0.832 0.8031 0.6656...
1.518 1.336 1.187 1.165 1.138 1.099 1.082];
figure
plot(2.*focus,slope,'b')
hold on
plot(2.*focusexp,slopeexprd1, '*g')
plot(2.*focusexp,slopeexprd2, '*m')
hold off
axis([-4 4 0.4 1.6])
legend('model','exp.  data Rasdif1','exp.  data Rasdif1')
xlabel('semi-major axis laser on plate [cm]',...
   'interpreter','latex','fontsize',30)
```

```
ylabel('slope [-]','interpreter','latex','fontsize',30)
title('Expected slope model vs.  slope experiment',...
   'interpreter','latex','fontsize',30)
% Experimental data (07/06/2011, 08/06/2011, 14/06/2011)
% Rotations are done in steps of 0.0045 rad
vpfocusexp=[-3 -2.5 -2 -1.5 2 3 4 5];
vrtptexprd1=[-0.8403 -1.0302 -1.4179 -2.0290 1.3605 0.7147...
   0.6307 0.3670]./(asin(0.0045)*10);
vrtptexprd2=[-0.8780 -1.0118 -1.4356 -1.7605 NaN 0.6549...
    0.6319 0.3935]./(asin(0.0045)*10);
figure
plot(2.*focus,virt_dep_pt)
hold on
plot(vpfocusexp,vrtpexprd1, '*g')
plot(vpfocusexp,vrtpexprd2, '*m')
hold off
   axis([-4 6 -100 100])
legend('model','exp.  data Rasdif1','exp.  data Rasdif1')
xlabel('semi-major axis laser on plate [cm]',...
   'interpreter','latex','fontsize',30)
ylabel('virtual point of departure anomaly [cm]',...
   'interpreter','latex','fontsize',30)
title('Expected VPoD model vs.  VPoD experiment',...
   'interpreter','latex','fontsize',30)par
```

A.3 Random noise determination

The random noise described in §5.2 is determined for int. al. the C300 pixel image sensor. The obtained σ can be used in the determination of the CRLB, as described in §5.4. The method used to obtain this σ is found in code below and an explanation is described in §5.4.1.

```
files = dir('*.png');
numfiles = numel(files);
for i=1:numfiles
 images{k} = imread(files(k).name);
% Getting certain pixel values (eight coordinates) of all images
% Here, the 3rd coordinate is the rgb, so it depends on which
colour of light one is using
 eval(['pixel1(k)= images{' num2str(k) '}(170,65,2);'])
 eval(['pixel2(k)= images{' num2str(k) '}(62,228,2);'])
 eval(['pixel3(k)= images{' num2str(k) '}(64,407,2);'])
 eval(['pixel4(k)= images{' num2str(k) '}(190,530,2);'])
 eval(['pixel5(k)= images{' num2str(k) '}(298,565,2);'])
 eval(['pixel6(k)= images{' num2str(k) '}(422,403,2);'])
```

```
 eval(['pixel7(k)= images{' num2str(k) '}(420,223,2);'])
 eval(['pixel8(k)= images{' num2str(k) '}(294,63,2);'])
end
% Plotting histograms for all pixels
a=figure;
histfit(pixel1,1+(max(pixel1)-min(pixel1)))
[muhat1,sigmahat1]=normfit(pixel1);
xlabel(''value (0 \leq x \leq 255)',...
   'interpreter','latex','fontsize',30)
ylabel('counts',...
   'interpreter','latex','fontsize',30)
title('pixel1 (170,65)',...
   'interpreter','latex','fontsize',30)
muhatstr1=['\hat{\mu}=' num2str(muhat1) ];
sigmahatstr1=['\hat{\sigma}=' num2str(sigmahat1)];
hatstr1=muhatstr1;sigmahatstr1;
% Getting mu and sigma values at the same place in the graph
text(muhat1+(max(pixel1)-min(pixel1))/4, max(hist(pixel1,1+...
 (max(pixel1)-min(pixel1))))-max(hist(pixel1,1+(max(pixel1))-...
 min(pixel1))/6), hatstr1, 'interpreter','latex', 'fontsize',30)
saveas(a,'pixel1.fig' )
```

This histogram plotting code is repeated 7 times to plot all the pixel histograms.

```
%saving pixeldata and mu and sigma's
save('muandsigma.mat','muhat1', 'sigmahat1', 'muhat2','sigmahat2'...
   ,'muhat3', 'sigmahat3','muhat4','sigmahat4', 'muhat5' ...
   ,'sigmahat5','muhat6','sigmahat6','muhat7','sigmahat7'...
   ,'muhat8','sigmahat8')
save('pixeldata.mat','pixel1','pixel2','pixel3','pixel4' ...
   ,'pixel5','pixel6','pixel7','pixel8')
% Choice of seeing pixel correlation and the time evolution of
a pixel
% Checking pixel correlation
userentry1 = input('Would you like to see the correlation between
pixels?  (y=1/n=0) ');
if userentry1 == 1
 check=1;
 for i=1:8
  for j=1:8
   if i <= j
    check=check+i;
   else
    figure
```

```
    eval(['scatter(pixel' num2str(i) ',pixel' num2str(j) ')']);
    title('Pixel correlation between 2 pixels','fontsize',18)
    xlabel('Pixel values','fontsize',18)
    ylabel('Pixel values','fontsize',18)
    axisequal
   end
  end
 end
 elseif  userentry1 == 0
  check=0;
end
userentry2 = input('Of which pixel would you like to see the value
vs.  time plot?  ');
if  userentry2 > 0
 tpix=1:1:numfiles;
 figure
 eval(['scatter(tpix,pixel' num2str(userentry2) ')'])
 title('Pixel readout of pixel user entry2','fontsize' ,18)
 xlabel('time [arb.units]','fontsize',18)
 ylabel('Pixel values [-]','fontsize',18)
```

More `userentry #` values are asked for at this point, but these are omitted in this display of code.

```
else  check2=0;
end
```

A.4 Cramér-Rao Lower Bound determination

The following code calculates the CRLB and plots the gradient and the CRLB in the x-direction for a given set of Rasdif (simulated) images. It first calculates the gradient energy of the image in both directions and constructs the FIM. It uses these to calculate the CRLB in both directions.

```
sigma=2; % used random error sigma
dpix=11.2*10^-6;
files = dir('*.png');
numfiles = numel(files);
% s, x and y vectors for conv2 function
s = [1 ; 1];
dx = [1, -1];
dy = [1;-1];
% preparing images to be square
for k=1:numfiles
 images{k} = imread(files(k).name);
```

```
 sqimages{k}= images{k}(:,41:280); % conv2 only works for square
images
 gxline{k} = conv2(double(conv2(double(sqimages{k}),double(dx),...
 'same')),double(s),'same');
 gyline{k} = conv2(double(conv2(double(sqimages{k}),double(dy),...
 'same')),double(s),'same');
% removing left over lines in the 240 × 240 image resulting in
a 238 × 238 image
 gx{k}=gxline{k}(1:238,1:238);
 gy{k}=gyline{k}(1:238,1:238);
%CALCULATING CRLB%
 sumIxsq(k)=sum(sum(gx{k}.^2));
 sumIxIy(k)=sum(sum(gx{k}.*gy{k}));
 sumIysq(k)=sum(sum(gy{k}.^2));
 F{k}=1/sigma^2*[sumIxsq(k), sumIxIy(k); sumIxIy(k), sumIysq(k)];
% calculating variances
 varx(k)=(dpix^2*sumIysq(k))/(sigma^2*det(F{k}));
 vary(k)=(dpix^2*sumIxsq(k))/(sigma^2*det(F{k}));
 sigmax(k)=sqrt(varx(k));
 sigmay(k)=sqrt(vary(k));
end
outerradmm= 1.44*0.5:1.44*0.01:1.44*5;
figure
plot(outerradmm,sumIxsq)
title('X gradient squared [-] vs.  diffraction plate size',...
   'interpreter','latex','fontsize',20)
ylabel('X gradient squared [-]','interpreter',...
   'latex','fontsize',30)
xlabel('Diffraction plate outer radius [mm]','interpreter',...
   'latex','fontsize',30)
figure
plot(outerradmm,sigmax*10^9)
title('σ CRLB,x w.r.t.  diffraction plate size',...
   'interpreter','latex','fontsize',20)
ylabel('σ CRLB,x[nm]','interpreter',...
   'latex','fontsize',30)
xlabel('Diffraction plate outer radius [mm]','interpreter',...
   'latex','fontsize',30)
```

Appendix B

Stand-alone manual for the RasCLiC set-up in TT1

The Transfer Tunnel One (TT1) at CERN, a tunnel where particle beams were transferred from the Proton Synchrotron (PS) to the Intersecting Storage Rings (ISR) until about 1984 when the ISR was decommissioned, is home to a 140 m test set-up (see Figure B.1). This set-up was con-

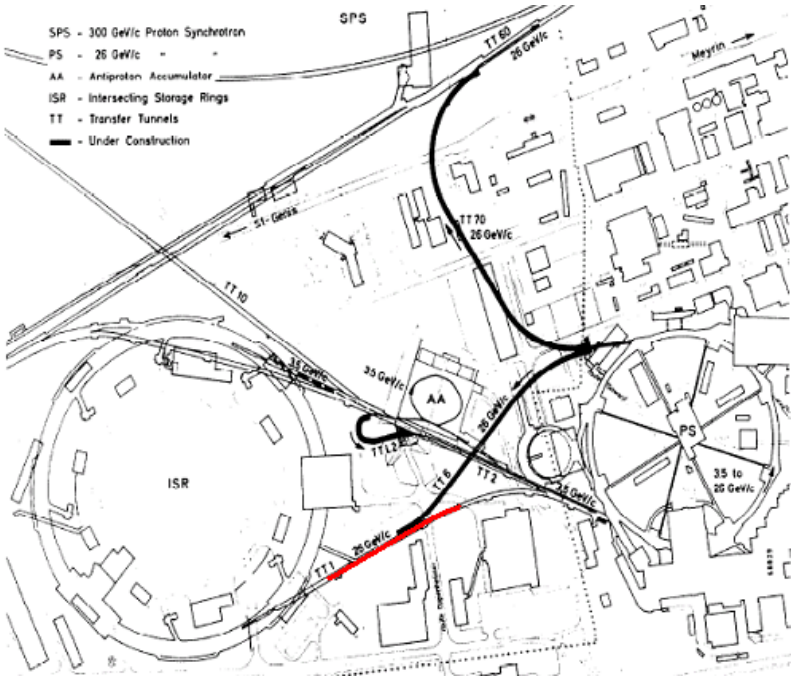

Figure B.1: The used part of TT1 (in red) relative to underground structures at CERN. At the South side of the LHC, the Super Proton Synchrotron (SPS) is just visible on this map

structed to test several alignment systems on same scale as the overlapping large distance alignment of the CLiC is designed (about 200 m). Today

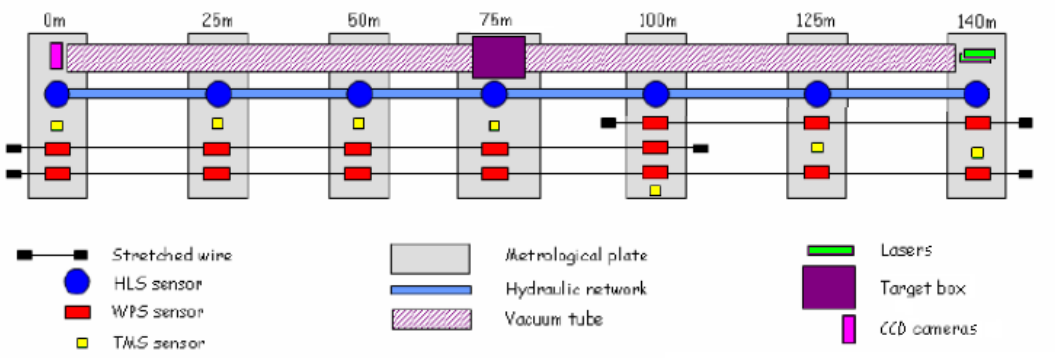

Figure B.2: Schematic lay-out of the alignment systems in the TT1 set-up

the Wire Positioning System (WPS), Hydrostatic Level System (HLS), Tilt Meter System (TMS) and the so-called RasCLiC are read out along side each other. The (double) RasCLiC is the Nikhef-built Rasdif system for CLiC to complement these systems or to be compared to them. Explanations of the alignment systems at TT1 can be found in Chapter 2 of the thesis (van Heijningen 2011) where this (stand-alone) manual is found in the appendix.

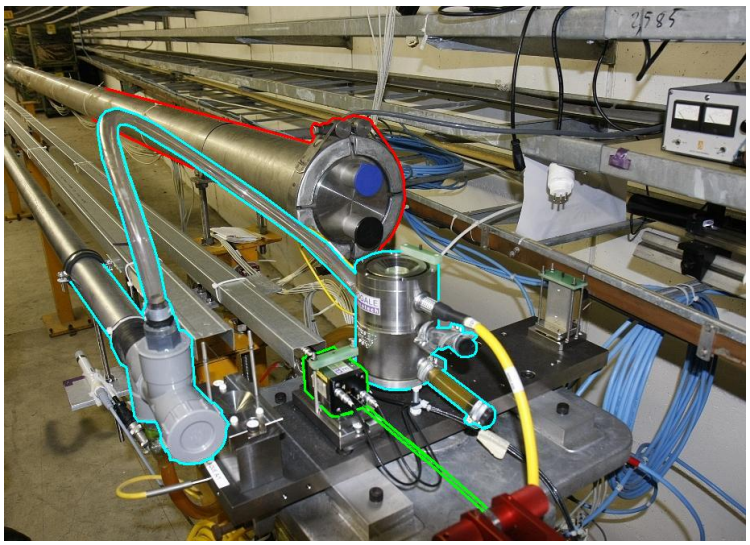

Figure B.3: Photograph of the laser side of the TT1 set-up, *old* photo. The lasers are not yet installed here and the vacuum tube is sealed of with blue caps. One can distinguish a vacuum tube (*red*), the WPS (*green*) and the HLS (*cyan*)

B.1 Laser side

The RasCLiC system is a double Rasdif over 140 m, where the lasers are at the North-East section of the tunnel at the start of the bending to the East. The two lasers were installed on 28 and 29 November 2011 and linked to the vacuum tube by means of bellows. Bellows where used to ensure independent movement of vacuum tube and the laser set-up.

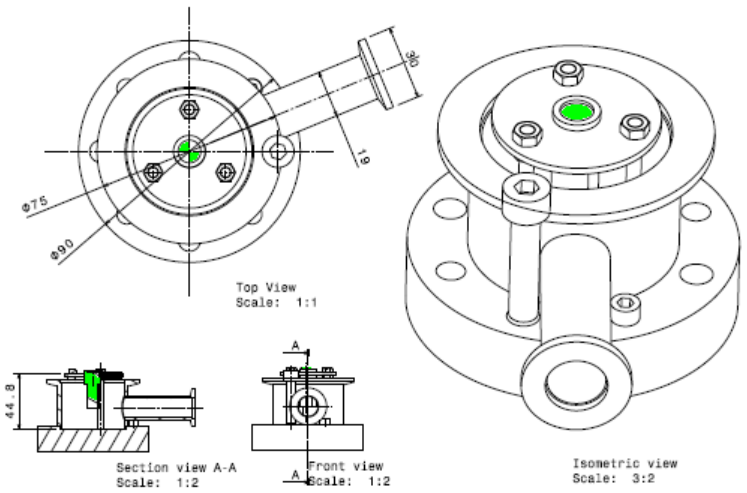

Figure B.4: Technical drawing of the laser-mount (courtesy of R. Rosing)

The design of the laser-mount was done by R. Rosing (Nikhef) and has dimensions similar to the fibre out-couplers of the red HeNe lasers (Melles Griot 05LHR925 and 25LHR925), which were used until the summer of 2011. The technical drawings of the laser-mount is shown in Figure B.4. The laser (indicated in green) is glued into a circular plate and the direction of the laser beam can be altered by six bolts, which attach the plate to the three threads. One can distinguish eight screws; the four metallic ones ensure tight fixing of the mount and with four dark ones one can alter the direction of the laser beam when its enclosed in the vacuum. In the mount, the former 4 screws have a larger hole than their thread, so that translation in the directions perpendicular to the set-up is possible.

A photograph of the laser side with only one bellow installed is shown in Figure B.5. The laser type is Diode Pumped Laser Diode (DPSS) emitting green light at 532nm and has proven to have the desired characteristics for this set-up. It has a large intensity for its size, can thus easily be made to fit in a vacuum envelope, emits coherent (enough) light up to 140 m, and the virtual point of departure of the coherent light almost coincides with the physical location of the crystal. The only drawback is that it consumes (and dissipates) a lot of power compared to its output (close to 350 mA at 3V, so approximately 1 W). When it was tested at Nikhef an increase of temperature of the messing cylinder could be

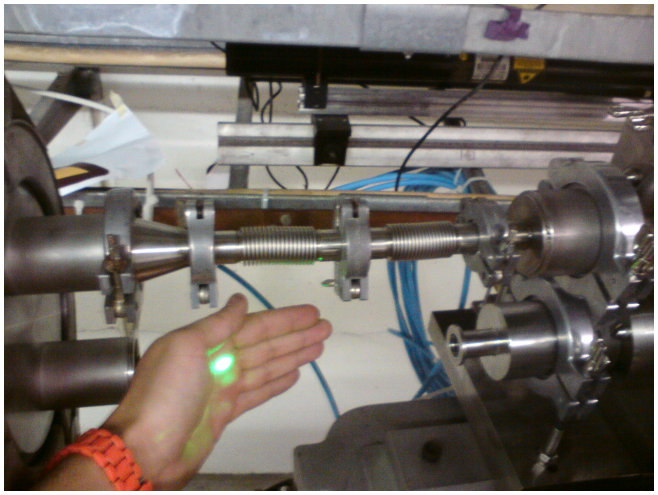

Figure B.5: The two lasers of the RasCLiC, one linked to the vacuum tube

felt, indicating the dissipation of electrical power. Both lasers have their own Delta (δ) power supply to ensure stability during operation. These δ power supplies have a maximum current output of 600 mA, so running both lasers on the same power supply would not work. When both lasers ran on just one power supply, the intensity of the lasers would variate substantially over time.

B.2 Vacuum system and diffraction plate

In Figure B.3 one see the North-East section of the vacuum tube: the laser side where the tunnel starts to bend to the East. The vacuum tube is a stainless steel tube with an inner diameter of 155 mm. It is made up of sections of some 6m and these are connected by clamps. At the laser side of the tube, two smaller tubes of about 10 cm are welded on. This makes installation of bellows to the individual lasers possible and makes it possible for the lasers to be in vacuum as well. Half-way down the tube flexible bellows are attached to ensure easy installation of the diffraction plate section. At the South-West side of the set-up (the image sensor side) the tube is sealed off with an optical window.

Inside the vacuum tube, several diaphragms are installed. Figure B.7(a) shows one of these diaphragms of which, with variable size (larger diameter near the diffraction plate section), seven are located along the length of the vacuum tube. They have a 'shark-teeth' shape to ensure that they do not have a well-defined diameter, which counteracts unwanted diffraction. The diaphragms were installed to get rid of interfering reflections in the vacuum tube that would fall om the diffraction plate or the image sensor.

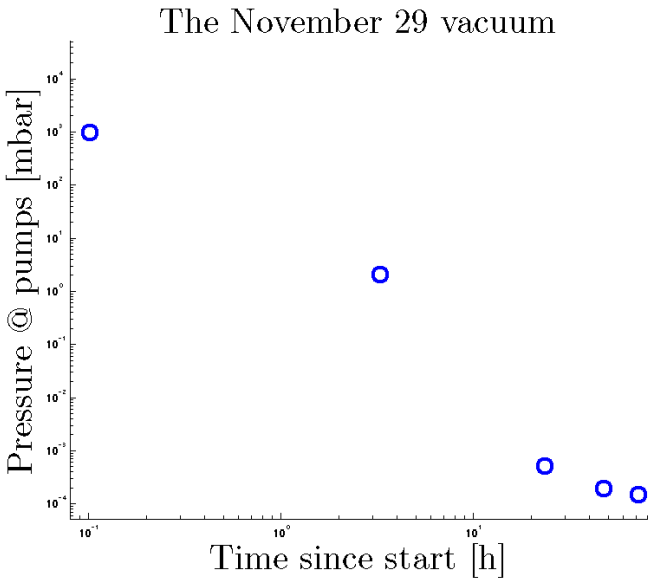

Figure B.6: Pressure readouts of the pumping stations

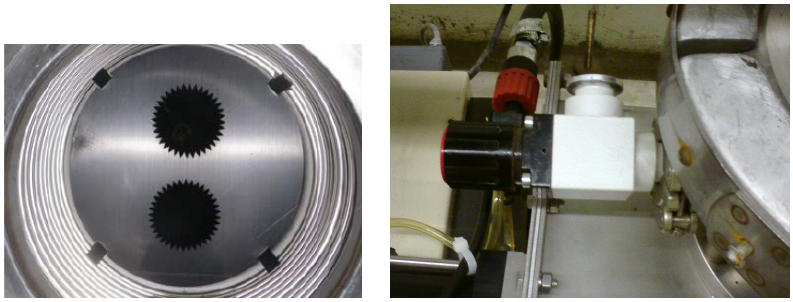

(a) (b)

Figure B.7: (a) 'Shark-teeth' diaphragms in the vacuum tube and (b) the valve one can use for releasing the vacuum

Attached to the vacuum tube one can find three pumping groups. André de Saever (CERN vacuum) closed the vacuum tube on 29 November and started the pumping procedure. This has brought the pressure down to $1.5{\cdot}10^{-4}$mbar in about three days starting from atmospheric pressure at 12:36. This is shown in Figure B.6 and Table B.1. Located on the centre pumping group is a valve to release the vacuum in a controlled way (see Figure B.7(b)).

In the middle of the set-up, a diffraction plate is placed to diffract the incoming light coming from the lasers. The plate contains two identical patterns now known to its users as *the four sausages*. Below one can see the design of one of those diffraction patterns (Figure B.8(a)), a simulated diffraction pattern[20] (Figure B.8(b)), a photograph of the diffraction plate holder(Figure B.8(c)) and a photograph of the image sensor image

Date	Time	Pressure readout [mbar])
29/11/2011	12:36	10^3
	15:45	2.05
30/11/2011	11:45	$5{\cdot}10^{-4}$
01/12/2011	10:30	$2{\cdot}10^{-4}$
02/12/2011	11:20	$1.5{\cdot}10^{-4}$

Table B.1: Pressure readouts by A. de Saever (CERN Vacuum)

readout on the PC (Figure B.8(d)). By hanging weight via a pulley on the threads where the diffraction plate holder one can translate in the horizontal direction and by turning the six bolts one can translate in the vertical direction.

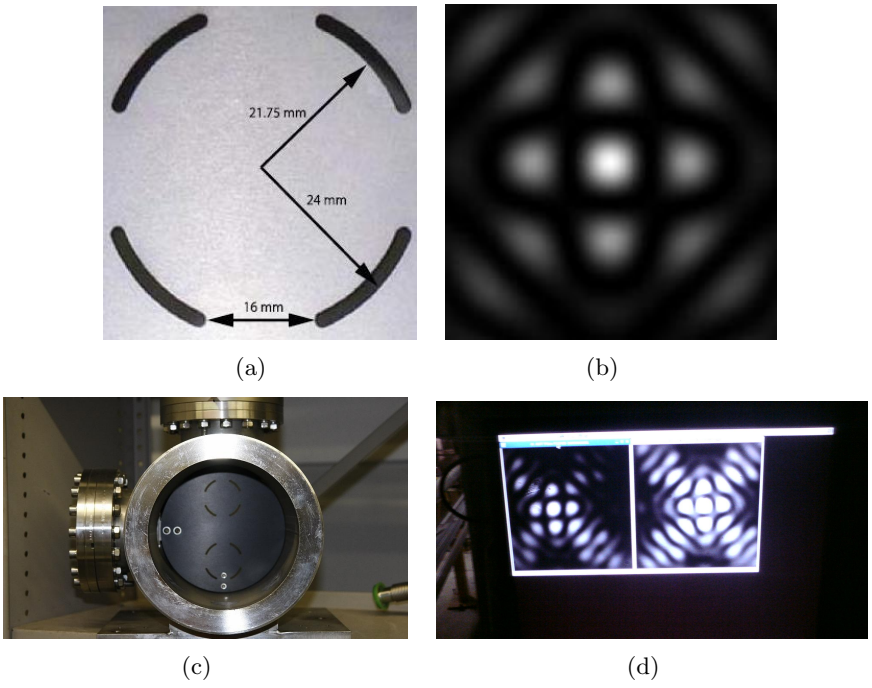

(a) (b)

(c) (d)

Figure B.8: (a) Design and dimensions of the diffraction pattern, (b) simulations of the resulting diffraction pattern, (c) a photograph of the plate holder and (d) a photograph of the image sensor readout at the PC

B.3 CCD image sensors and readout system

The side where the readout of the system takes place is the side where the image sensors and the PC are. The image sensor-type is PIKE F100B Fiber from Allied Vision and its specifications are shown in Table B.2. Two of these image sensors are used in the RasCLiC set-up.

Property or Feature	Specification
Colour/BW	BW image sensor
Effective picture elements	1004(H) x 1004(V)
Picture size	1000(H) x 1000(V), all modes
Cell/Pixel size	7.4μm x 7.4μm
Resolution depth	8, 10, 12 14 16 bit (high SNR mode)
Digital interface	IEEE 1394b (S800); IIDC V1.31
Transfer rate	100, 200, 400, 800 Mb/s
ADC	14 bit
Frame rates	Up to 48Hz (full resolution)
Gain control	Manual: 0-24 dB (steps of 0.0353 dB)
Shutter speed	35μs - 67s; Auto shutter
Dimensions	44mm x 44mm x 90mm
Operating temperature	5 °C - 55 °C
Power consumtion	5W

Table B.2: Specifications of the PIKE F100B image sensors

(a) (b)

Figure B.9: (a) Catalogue picture of a PIKE100B and (b) two PIKE F100B cams in the TT1 set-up

The two image sensors can be adjusted in height via the 8 bolts that can move vertically on the thread. The horizontal direction of the complete two image sensor structure is fixed as the plate with the threads is bolted to a metro-logical plate. If a horizontal translation is needed to have images on the image sensors, which is not possible without dismounting the image sensors from the metro-logical plate, one has to keep in mind that the horizontal location of the images can also be altered by translation of the diffraction plate holder (only half the translation needed) and translation of the lasers.

The upper image sensor can, however, be translated individually by means of tiny screws on the top and on the sides. To do this, one would first have to loosen the 4 screws holding the plate, where the upper image sensor is *hanging* in. One can see this set-up in Figure B.9(b) and a

catalogue picture of a Pike F100B is shown in Figure B.9(a). The optics of the image sensor was not of interest for this set-up and was taken off.

The PC that is connected to the image sensors reads out the image sensors. It runs on CERN Scientific Linux 5 and was installed by Juha Kemppinen on 13/10/2011. It has two user accounts (*root* and *rasclic*) and these are used for different purposes. The former is used to install new software and rights issue handling and the latter is used for running the image analysis software.

When doing image analysis, one has two options. In the directory *rasclic/jSensiflexHarry-1.6.7* one can find software that shows images the image sensor picks up (.*show*) and software that gives a coordinate read-out compared to the first image it picks up (.*RasCLICTT1*). In the 'show' software one can use several commandos: *s* for saving one image, *d* for starting Rasdif analysis and *v* for starting rapid images writing (10 Hz can be achieved).

List of Figures

List of Tables